

**Protein and dyes in confinement and
protein dynamics studied by
fluorescence techniques and NMR
spectroscopy**

Dissertation

vorgelegt von

M. Sc. Mengjun Xue

aus Mengzhou, China

Von der Fakultät II -Mathematik und Naturwissenschaften
der Technischen Universität Berlin
zur Erlangung des akademischen Grades

Doktor der Naturwissenschaften

-Dr. rer.nat.-

genehmigte Dissertation

Promotionsausschuss:

Vorsitzender: Prof. Dr. Thorsten Ressler

Berichter: Prof. Dr. Gerhard H. Findenegg, TU Berlin

Berichter: Professor Dr. Michael Gradzielski, TU Berlin

Berichter: Professor Dr. Stefan Franzen, NC State University, Raleigh

Tag der wissenschaftlichen Aussprache: 17.12.2012

Berlin 2013

D83

Acknowledgments

This Thesis was written at the Stranski Laboratory for Physical and Theoretical Chemistry at the Technical University Berlin, in the framework of the International Graduate Research Training Group 1524 " Self-Assembled Soft Matter Nano-Structures at Interfaces" as a part of the subproject B3.1 Protein assembly in surface-functionalized cylindrical nanopores.

First, I would like to thank my advisor, Prof. Gerhard H. Findenegg, for his support and the opportunity to work in his group, for many stimulating discussions, for his invaluable advice and guidance. My thanks also go to Prof. Stefan Franzen for the opportunity to work in his group at NC State University and to work on the NMR project, and for agreeing to come to Berlin for my PhD defense. Moreover my thanks also go to Prof. Hanna Gracz for the NMR measurements and her invaluable advice and guidance on NMR analysis. I would like to thank Prof. Michael Gradzielski for agreeing to be one of the members of the dissertation defense committee and allowing me to use the Leica TCS SP5 II confocal microscope to perform the fluorescence project. My thanks also go to Prof. Reza Ghiladi and Dr. Jennifer D' Antonio for the chance to prepare some DHP samples in their lab and the invaluable suggestions. My thanks also go to Prof. Dr. Thorsten Ressler for the agreeing to be the chairman in my PhD defense. I would like to thank Prof. Peter Hildebrandt for the opportunity to make some Raman experiments in his lab.

I want to express my sincere thanks to all employees of the Stranski Laboratory for always being very friendly and for giving me numerous aids. I especially would like to acknowledge Andreas Klee for fruitful discussions and advices on fluorescence technique and for the friendship. My thanks go to Dr. Dilek Akcakayiran for her fruitful helps in my research work and BET measurement of mesoporous silica. I want to thank Dr. Bhuvnesh Bharti, Vinzenz Fleischer and Sören Selve for help in the porous particle synthesis and characterization and DLS measurements of lysozyme solutions. I also would like to thank Raphael Michel for his friendly helps during my visiting in NCSU. In addition,

Yan Zeng, Hsin-yi Liu, Xiao Xie, Changzhu Wu, Zhenfang Zhang, Jianli Zhao, and all those friends in the Stranski laboratory are acknowledged for their friendship and supports. I would like to thank Shu Jiang for her help and advice on preparing the DHP A mutant (M49C). My thanks also go to Junjie Zhao for her advice on preparing of DHP A, and I also want to thank Jing Zhao for his help on the preparation and purification of DHP A.

I am grateful for Deutsche Forschungsgemeinschaft (DFG) in the frame work of IGRTG-1524 for the financial support. I would like to thank all IGRTG members, especially, I would like express my thanks to the Chairman, Prof. Martin Schoen, Managing Director, Dr. Daniela Fliegner and Administrative assistant, Petra Erdmann for their supports. I also would like to thank secretaries, Christiane, Maria, Michaela, Gabi and Rene for their helps.

I would like to express my gratitude to my parents and my young brother for being always there to support me.

Eidesstattliche Versicherung

Hiermit versichere ich, Mengjun Xue, dass die vorliegende Dissertation selbstständig und nur unter Benutzung der aufgeführten Hilfsmittel und Quellen verfasst worden ist.

Abstract

There has been ever increasing interest in ordered mesoporous materials because of their high applications potential in many fields, such as drug delivery, artificial light-harvesting and biocatalysis. MCM-41 mesoporous silica nanoparticles with pore widths in the 3 to 4 nm range hold great promise as a drug carrier vehicle because of the chemical stability, well-defined pore geometry, and tunable pore size of the particles, but the development of simple and biocompatible capping system for the pores has remained a challenge. We have found that lysozyme molecules can act as a pH-responsive nano-valve to block and unlock the pore entrances of MCM-41 nanoparticles for guest molecules. Experiments with the dye rhodamine B as a model drug indicate that pore blocking by lysozyme is due to a pH induced conformational change by which the effective size of the protein is changed in a reversible manner. This effect may form the basis of a controlled-release system without the need to functionalize the pore mouth and caps.

Mesoporous silica materials have also attracted interest as a host for nano-confined dye molecules, which undergo enhanced energy transfer and exhibit optical functionality. Measurements of the fluorescence resonance energy transfer (FRET) from fluorescein (donor) to rhodamine b (acceptor) molecules embedded in the pore space of MCM-41 silica were performed by fluorescence lifetime imaging microscopy (FLIM) and are analyzed in terms of a two- and three-exponential decay function. Results are presented for a given donor concentration and a wide range of acceptor concentrations. The mean donor-to-acceptor distance r_{DA} as calculated from the FRET efficiency is compared with the mean separation of dye molecules d as obtained from the measured uptake. It is found that r_{DA} is similar to d at high overall dye concentrations but significantly smaller than d at low concentrations. These findings are discussed in terms of the distribution of molecular distances of the guest molecules in the silica matrix. These FRET studies with dye molecules form a basis for an investigation into the mean distance between protein molecules in the pore space of ordered mesoporous silica materials.

Although current understanding of enzyme function is based mostly on static protein structures as obtained from X-ray crystallography, the dynamics of protein molecules is believed to be essential to their biological function. Dehaloperoxidase-hemoglobin (DHP A) can oxidatively dehalogenate haloaromatic compounds while maintaining its oxygen storage function. We have used hetero-nuclear NMR methods to probe the dynamics of DHP A in solution in the presence of the substrate 2, 4, 6-trichlorophenol (TCP). To facilitate the NMR measurements, DHP A was labeled with ^{15}N , and NMR relaxation parameters T_1 and T_2 and $\{^1\text{H}\}$ - ^{15}N NOE have been analyzed using reduced spectral density mapping and the Lipari-Szabo model free method. The preliminary ^{15}N spin-relaxation data reveal evidence for the presence of slow conformational exchange in DHP A in the presence of TCP. Further work is needed to corroborate these findings and their significance for the catalytic oxidization reaction.

Zusammenfassung

Mesoporöse Materialien mit geordneter Porenstruktur sind von Interesse im Hinblick auf ihr breites Anwendungspotenzial in verschiedenen Feldern, unter anderem als Träger von Wirkstoffen oder künstlichen Licht-Antennen, sowie in der Biokatalyse. MCM-41 Silica-Nanoteilchen mit definierter Porenweite im Bereich von 3 bis 4 nm weisen vielversprechende Eigenschaften als Trägerpartikel für pharmazeutische Wirkstoffe auf, doch bleibt die Entwicklung eines einfachen und bio-kompatiblen Porenverschluss-Systems eine Herausforderung. Wir haben gefunden, dass Lysozym-Moleküle als pH-responsive Nanoschalter zum Verschließen und Öffnen der Poreneingänge von MCM-41 Teilchen wirken können. Experimente mit dem Farbstoff Rhodamin B als Modell-Wirkstoff zeigen, dass die Wirkung von Lysozym als molekularer Schalter auf einer pH-induzierten Konformationsänderung beruht, durch welche die effektive Größe der Proteinmoleküle in reversibler Weise beeinflusst wird. Dieser Effekt könnte die Basis für Systeme zur kontrollierten Wirkstoff-Abgabe ohne Notwendigkeit einer chemischen Modifizierung der Porenwände oder des Porenverschlusses bilden.

Mesoporöse Silica-Materialien sind auch von Interesse als Wirtsmaterialien zum Studium photochemischer Prozesse in räumlich begrenzter Geometrie. Es wurde der Fluoreszenz-Resonanzenergietransfer (FRET) von Fluorescein (Donor) auf Rhodamin B (Akzeptor) in MCM-41 Silica mittels der Fluoreszenz-Lebenszeit-Imaging-Mikroskopie (FLIM) studiert. Messungen für eine konstante Donorkonzentration und verschiedene Akzeptor-Konzentrationen wurden mittels multi-exponentiellen Abfall-Funktionen analysiert. Aus den FRET-Daten wurde der Donor-Akzeptor Abstand r_{DA} ermittelt und mit dem aus der (Gesamt-) Farbstoff-Konzentrationen bestimmten mittleren Teilchenabstand d verglichen. Bei hohen Farbstoff-Konzentrationen ergeben sich für r_{DA} Werte ähnlich zu d , bei geringen Farbstoff-Konzentrationen dagegen deutlich kleiner als d . Hieraus lassen sich Rückschlüsse auf die Verteilung der Moleküle in der porösen Matrix ziehen. Diese Untersuchungen bilden eine Basis für weiterführende Untersuchungen zum Studium der Verteilung von Proteinmolekülen in den Poren von geordnet mesoporösen Silica-Materialien.

Obwohl das aktuelle Verständnis von Enzym-Funktion überwiegend auf der aus der Röntgen-Strukturbestimmung erhaltenen statischen Proteinstruktur basiert, wird allgemein vermutet, dass auch die Protein-Dynamik von essentieller Bedeutung für ihre biologische Funktion ist. Dehaloperoxidase-Hämoglobin (DHP A) kann halogenierte Aromaten oxidativ dehalogenieren unter Beibehaltung ihrer Sauerstoff-Speicherfunktion. In dieser Arbeit wurden heteronukleare NMR Methoden benutzt, um die Dynamik von DHP A in Lösung in Gegenwart des Substrats 2, 4, 6-trichlorophenol (TCP) zu studieren. Für die NMR Messungen wurde mit ^{15}N angereichertes DHP A hergestellt. Die NMR Relaxationsparameter T_1 und T_2 und $\{^1\text{H}\}$ - ^{15}N NOE wurden mittels reduced spectral density mapping und der Lipari-Szabo modellfreien Methode analysiert. Die in dieser Arbeit gewonnenen ^{15}N -Relaxationsdaten geben Hinweise auf langsam ablaufende Konformationsänderungen in DHP A in Gegenwart von TCP. Weitere Untersuchungen sind nötig, um diese Ergebnisse abzusichern und ihren Bezug zur katalytischen Oxidation abzuklären.

Contents

1 Introduction.....	1
2 Fundamentals.....	3
2.1 <i>Mesoporous silica-based targeted drug delivery</i>	3
2.1.1 Targeted drug delivery	3
2.1.2 Mesoporous silica.....	3
2.1.3 Mesoporous silica-based drug delivery systems.....	3
2.2 <i>Fluorescence</i>	7
2.2.1 Phenomena of fluorescence.....	7
2.2.2 The Jablonski diagram.....	8
2.2.3 Fluorescence lifetime	9
2.2.4 Time-Correlated Single Photon Counting (TCSPC)	10
2.3 <i>Fluorescence resonance energy transfer (FRET)</i>	11
2.3.1 Förster distance.....	12
2.3.2 Orientation Factor k^2	12
2.4 <i>Fluorescence lifetime imaging microscopy (FLIM)</i>	14
2.4.1 Confocal microscopy.....	14
2.4.2 Fluorescence lifetime imaging microscopy (FLIM).....	14
2.4.3 FRET-FLIM.....	15
2.5 <i>Protein dynamics</i>	16
2.6 <i>NMR relaxation analysis</i>	16
2.6.1 Chemical Shift Anisotropy (CSA)	17
2.6.2 The dipole-dipole mechanism	18
2.6.3 The role of conformational exchange	18
2.6.4 Reduced spectral density mapping.....	18
2.6.5 Lipari and Szabo model-free analysis.....	21
2.6.6 CPMG (Carr-Purcell-Meiboom-Gill) relaxation dispersion NMR experiment.....	23
2.6.7 Applications to specific proteins.....	25
3 Experimental section	29
3.1 <i>Chemicals</i>	29
3.2 <i>Preparation of MCM-41 silica particles</i>	29
3.3 <i>Loading, capping and release experiments</i>	30
3.4 <i>Characterization of silica host materials</i>	30
3.4.1 SAXS	30
3.4.2 TEM.....	31
3.4.3 Nitrogen Sorption	31
3.4.4 CLSM analysis	31
3.4.5 Fluorescence lifetime imaging	31
3.5 <i>Protein adsorption</i>	32
3.6 <i>lysozyme labeling</i>	32
3.7 <i>Expression and purification of ^{15}N labeled DHP A</i>	32

3.8 NMR spectroscopy.....	33
3.9 NMR data processing.....	34
3.10 UV-Vis enzymatic assays.....	35
4 Lysozyme as a pH-responsive valve for controlled release of guest molecules from mesoporous silica	37
4.1 Introduction.....	37
4.2 Results.....	38
4.2.1 Characterization of mesoporous silica.....	39
4.2.2 Lysozyme adsorption.....	40
4.2.3 pH-responsive pore blocking and unlocking.....	43
4.3 Discussion and conclusion.....	44
5 Energy transfer between dye molecules in MCM-41 studied by fluorescence lifetime imaging	50
5.1 Introduction.....	50
5.2 Results.....	51
5.2.1 Characterization of MCM-41.....	51
5.2.2 MCM-41 particles doped with fluorescein and rhodamine b.....	52
5.2.3 Fluorescence lifetime analysis.....	53
5.2.4 FRET efficiency.....	57
5.3 Discussion and conclusion.....	59
6 Intrinsic dynamics of DHP A underlies its enzymatic function	63
6.1 Introduction.....	63
6.2 Results and discussion.....	63
6.2.1 Binding site of DHP A for TCP.....	64
6.2.2 Backbone ¹⁵ N relaxation.....	66
6.2.3 Reduced spectral density mapping.....	69
6.2.4 Interpretation of J(ω_N) and J(0.87 ω_H) via Lipari-Szabo mapping.....	72
6.2.5 Lipari-Szabo model free analysis.....	75
6.3 Conclusions.....	77
7 Summary and outlook	80
Appendix.....	82
A1 Publications.....	82
A2 Tables of NMR data.....	83
A3.....	90

1 Introduction

Mesoporous materials have found many potential applications in many fields, such as drug delivery [1], catalysis [2], and artificial light-harvesting [3]. Ordered mesoporous silica materials such as MCM-41 and SBA-15, which constitute ordered arrays of cylindrical channels of uniform size, have been extensively studied because of their well-defined mesoscale structure [4, 5]. Polymers [6], inorganic nanoparticles [7], and supramolecular assemblies [8] have been used as caps to construct mesoporous silica-based drug delivery system. However, many of the existing capping systems have disadvantages such as their poor biocompatibility and toxicity. In chapter 4, a simple mesoporous silica-based drug delivery system with lysozyme caps is demonstrated. The operation of this valve is based on the physical adsorption of lysozyme molecule in the pores of native porous silica, which block and close the pore due to a pH induced conformational change by which the effective size of the protein is changed in a reversible manner. In addition, the energy transfer from fluorescein (donor) to rhodamine b (acceptor) guest molecules adsorbed in the pore space of MCM-41 were studied by fluorescence lifetime imaging microscopy (FLIM) in chapter 5. The mean donor-to-acceptor distance r_{DA} is calculated from the FRET efficiency and compared with the mean separation of dye molecules as obtained from the measured uptake.

The application of biocatalysis is often handicapped by their difficult recovery and their low stability [2]. As enzyme immobilization often results in enhanced stabilization [2], many different immobilization methods have been developed. Mesoporous silica materials have been found as a promising supports for enzyme immobilization because of its unique pore structure [2, 10], regardless of the achievements in biocatalysis applications, the understanding of enzyme activity is still in its infancy.

Protein dynamics has been found related to its function [9]. Dehaloperoxidase-hemoglobin (DHP A) can function as catalysis to oxidatively dehalogenate

haloaromatics [11]. A detailed understanding of the intimate linkage between flexibility of DHP A and its catalysis is a current challenge. In chapter 6, the dynamics of DHP A with substrate (2, 4, 6-trichlorophenol, TCP) were studied by NMR relaxation measurements. The preliminary ^{15}N relaxation experiments reveal the presence of conformational heterogeneity on the μs -ms time scale in the structure of DHP A with TCP.

References of chapter 1

- [1] Trewyn, B. G.; Slowing, I. I.; Giri, S.; Chen, H.; Lin, V. S.-Y. *Acc. Chem. Res.* 2007, 40, 846-853.
- [2] Hartmann, M.; and Jung, D. *J. Mater. Chem.*, 2010, 20, 844-857.
- [3] Ruiz, A. Z.; Li, H.; Calzaferri, G. *Angew. Chem. Int. Ed.* 2006, 45, 5282–5287.
- [4] (a) Kresge, C. T.; Leonowicz, M. E.; Roth, W. J.; Vartuli, J. C.; Beck, J. S. *Nature*, 1992, 359, 710-712. (b) Zhao, D.; Feng, J.; Huo, Q.; Melosh, N.; Fredrickson, G. H.; Chmelka, B. F.; Stucky, G. D. *Science* 1998, 23, 279, 548-552.
- [5] Vallet-Regí, M.; Balas, F.; Arcos, D. *Angew. Chem. Int. Ed.* 2007, 46, 7548-7558.
- [6] Singh, N.; Karambelkar, A.; Gu, L.; Lin, K.; Miller, J. S.; Chen, C. S.; Sailor, M. J.; Bhatia, S. N. *J. Am. Chem. Soc.* 2011, 133, 19582-19585.
- [7] Lai, C.-Y.; Trewyn, B. G.; Jeftinija, D. M.; Jeftinija, K.; Xu, S.; Jeftinija, S.; Lin, V. S. Y. *J. Am. Chem. Soc.* 2003, 125, 4451-4459.
- [8] Nguyen, T. D.; Tseng, H. R.; Celestre, P. C.; Flood, A. H.; Liu, Y.; Stoddart, J. F.; Zink, J. I. *Proc. Natl. Acad. Sci. USA* 2005, 102, 10029-10034.
- [9] Eisenmesser, E. Z.; Bosco, D.; Akke, M.; Kern, D. *Science*, 2002, 1520-1523.
- [10] Hartmann, M. *Chem. Mater.*, 2005, 17, 4577-4593.
- [11] Davis, M. F.; Boby, B. G.; Franzen, S. *Biochemistry* 2010, 49, 1199-1206.

2 Fundamentals

2.1 Mesoporous silica-based targeted drug delivery

2.1.1 Targeted drug delivery

In a traditional drug delivery system, intravascular injection or oral ingestion, the pharmaceutical drug is distributed through the systemic blood circulation throughout the body [1], only a small portion of drugs reaches the diseased organ. Targeted drug delivery aims to enhance the medication in the affected tissues while reducing the amounts of the medication in the remaining non-affected tissues [1]. The delivery system can improve the effective use of drug molecules while avoiding or reducing those side effects as it can be targeted directly to the diseased tissue [1].

2.1.2 Mesoporous silica

The ordered mesoporous silica materials of the SBA-15 (Santa Barbara amorphous silica) and MCM-41 (Mobil Crystalline Materials) have well-defined pore geometry and tunable pore diameter [2, 3]. These materials have been synthesized by using the template molecules, poly(ethylene oxide)-poly(propyleneoxide)-poly(ethylene oxide) triblock copolymer (Pluronic P123) and hexadecyltrimethylammonium bromide ($C_{16}TAB$), respectively [2-4], which is illustrated in Figure 1 [4]. The synthesis of SBA-15 is performed in acidic medium at a pH below pH 2, and the preparation of MCM-41 is performed in basic media [2-4].

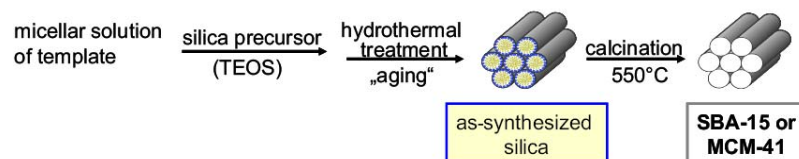


Figure 1. The method of synthesis of SBA-15 and MCM-41. From literature [4].

2.1.3 Mesoporous silica-based drug delivery systems

MCM-41 and SBA-15 have been widely used as carriers to load and protect therapeutic drugs and further control the release of drug molecules [5-9].

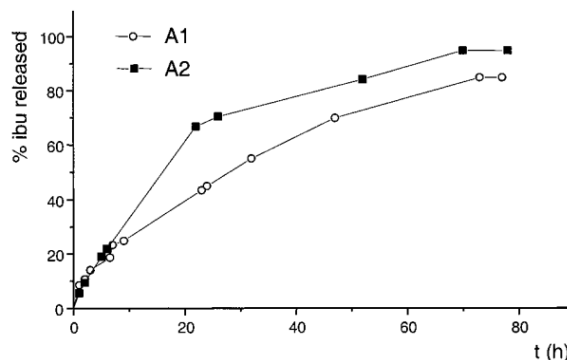


Figure 2. Ibuprofen release from MCM-41A1 and 2. Modified from literature [10].

Vallet-Regi et al first demonstrated that MCM-41 porous silica has the capability for adsorbing and then later releasing ibuprofen guest molecules (an anti-inflammatory drug), as shown in Figure 2 [10]. The MCM-41 silica with different pore sizes (2.5 and 1.8 nm) are used to accommodate guest molecules, and the drug molecules diffuse out of the porous silica when the drug-loaded materials are immersed in a simulated body fluid [10]

Since then, a large numbers of studies on MCM-41 based drug delivery system has been reported [11, 12]. Zink et al. reported a MCM-41-based drug delivery system which uses a novel supramolecular valve with the mobile part to control capping and release of guest molecules (Figure 3 and 4) [13]. The bistable, redox-controllable rotaxane R^{4+} was tethered on the surface of mesoporous silica. In R^{4+} , the movable part of the molecule is cyclobis(paraquat-p-phenylene) ($CBPQT^{4+}$) (blue) component that can be induced to move between a dioxynaphthalene (DNP) station (red) and a tetrathiafulvalene (TTF) station (green) under redox control. The valve is closed by oxidation of the TTF to its dication, inducing the $CBPQT^{4+}$ ring to move to the DNP station, since it is much closer to the pore mouth, the valve is closed. By adding ascorbic acid to reduce the TTF dication to its neutral state, the $CBPQT^{4+}$ ring moves back to the TTF station, the valve is opened, thus the drug molecules can release from the mesoporous silica (Figure 3, 4) [13].

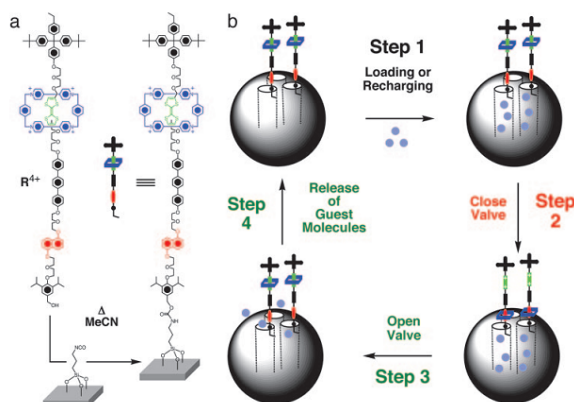


Figure 3. The surface attachment of bistable rotaxanes to silica particles along with a cycle for loading and release of $\text{Ir}(\text{ppy})_3$ guest molecules. From literature [13].

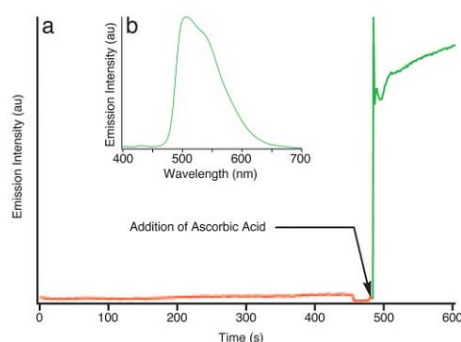


Figure 4. Fluorescence spectroscopy indicating the controlled release of the $\text{Ir}(\text{ppy})_3$ guest molecules from the porous silica. From literature [13]

Inorganic nanoparticles can also be used as caps for the pores of mesoporous silica materials to encapsulate drug molecules inside the MCM-41 and uncapping of the openings of the pores [14-17]. A mesoporous silica based carrier system using nano-sized CdS particles as a valve for controlled drug release was reported by Lin and coworkers (Figure 5 and 6) [14]. In the work, CdS nanoparticles were used to close pores via disulfide linkage between the CdS caps and the mesoporous silica [14]. Opening of the pores was then achieved by a chemical release trigger by which the disulfide bridges between the pore mouth and cap were destroyed [14].

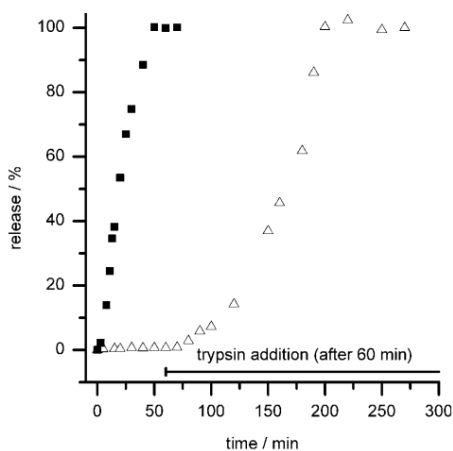


Figure 8. Release for MCM-41 silica with avidin caps (Δ), and release from MCM-41 without avidin caps (\blacksquare) by the enzymatic hydrolysis of the attached protein avidin. From literature [18].

The existing capping systems have disadvantages due to their toxicity and poor biocompatibility. This problem could be solved by using biomolecules as caps because of their good biocompatibility [18]. Recently, Bein et al. developed an avidin-based cap system for MCM-41 mesoporous silica, which uses the biotin–avidin complex (Figure 7, 8) [18]. The avidin can block the pore mouth of mesoporous silica and prevent the leaching of guest molecules, guest molecules release when the attached protein avidin is hydrolyzed by adding trypsin [18].

2.2 Fluorescence

2.2.1 Phenomena of fluorescence

Fluorescence is light emitted by a dye molecule that has absorbed light of one wavelength and then emit light of another longer wavelength [19]. In most cases, the emitted light has a longer wavelength than the absorbed light. It is also possible that the emitted light has the same wavelength as the absorbed light, this is termed "resonance fluorescence" [19]. The wavelength of the emitted light may also be shorter than the absorbed light if one electron to absorb two photons [19].

Some typical fluorescent molecules are shown in Figure 9 [20]. John Frederick William Herschel reported the first observation of fluorescence from a quinine solution excited by sunlight [20].

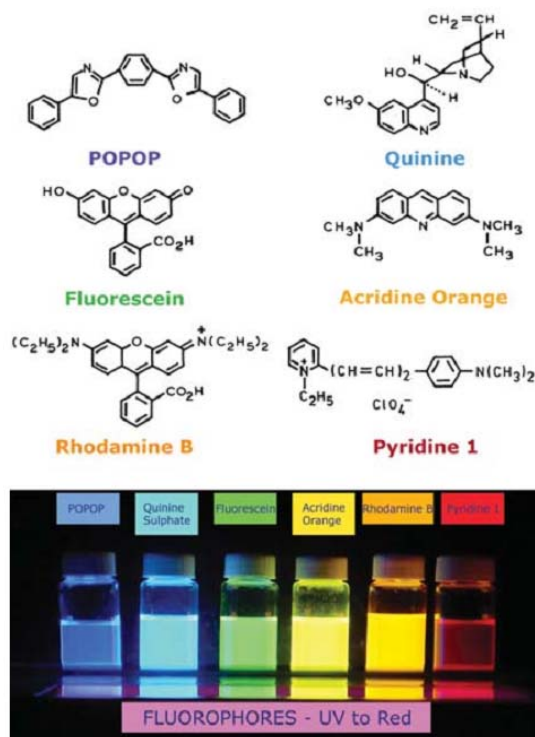


Figure 9. Structures of some typical dyes. From literature [20].

2.2.2 The Jablonski diagram

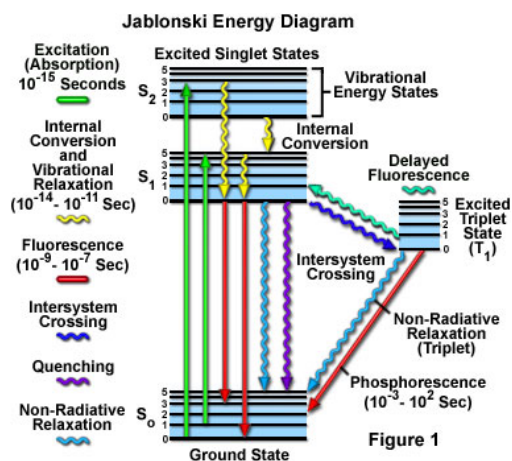


Figure 10. The Jablonski diagram. From literature [21].

The Jablonski diagrams are usually used to describe the processes between the absorption and emission of light [20]. The dye molecules can exist in different energy level, such as, the singlet S_0 (ground), S_1 (first electronic state), and S_2 (second electronic state) are shown in the typical Jablonski diagram (Figure 10)

[20, 21]. There are a number of vibrational energy levels (depicted by 0, 1, 2, etc.) at each of these electronic energy levels. The transitions between the energy levels are demonstrated as vertical lines to illustrate light absorption. After the absorption of electromagnetic radiation, energy may be dissipated through vibrational relaxation or internal conversion [20, 21]. Vibrational relaxation is a non-radiative process [20, 21]. It is indicated as a curved yellow arrow on the Jablonski diagram, between vibrational levels (Figure 10). The excited molecule can also have a transition from a vibration level in a higher electronic state to another vibration level in one lower electronic state, which is indicated on a Jablonski diagram as a curved yellow curve arrow between two vibrational levels in different electronic states (Figure 10) [20, 21]. The vibrational relaxation or internal conversion generally occurs in a picosecond or less, which is completed before emission of fluorescence photons as fluorescence lifetimes are typically near 10^{-8} s [20, 21].

Dye molecules in the S_1 energy level can undergo a spin conversion to the first triplet state (T_1), which is termed intersystem crossing. Emission of electromagnetic radiation from T_1 is called phosphorescence, and is generally shifted to longer wavelengths [20, 21]. The rate constants for triplet emission are smaller than those for fluorescence because the transition from T_1 to the singlet ground state is forbidden [20, 21]. The dye molecules in the excited triplet state has a longer lifetime, is chemically more reactive, and may interact with another molecule to covalent modifications, thus the dye molecule will not be excited again to emit fluorescence photons [22]. This is termed photobleaching.

2.2.3 Fluorescence lifetime

Fluorescence lifetime is the average time the molecule stays in its excited state before returning to the ground state [20]. Many of dye molecules have lifetimes with nanoseconds, but these lifetimes can change over a wide range depending on local environmental conditions [20]. Measurements of fluorescence lifetimes are informative, fluorescence lifetimes are sensitively dependent on protein conformations, and monitoring lifetime fluctuation has been used as studying protein conformational dynamics at single molecule level [23].

2.2.4 Time-Correlated Single Photon Counting (TCSPC)

TCSPC is a very accurate technique to measure fluorescence lifetime, which can record low level light signals with picosecond time resolution [24]. TCSPC technique can detect single photons of a light signal, record the arrival times of the individual photons, and reconstruct of the histogram of the arrival times [23, 25, 26]. Figure 11 shows how the histogram is formed from the measurement of lifetime by TCSPC [26]. Dye molecule is excited by pulsed laser, and emit fluorescence photons, which will be measured by electronics, for each detected photon, the arrival time with respect to the excitation pulse and the chronological arrival time are recorded [23, 26], the histogram of arrival times (with respect to pulse laser) is collected, a typical histogram is a exponential decay curve, as shown in Figure 11 [26], which can be fitted to single or multiple exponential decay function to extract the fluorescence lifetime [20].

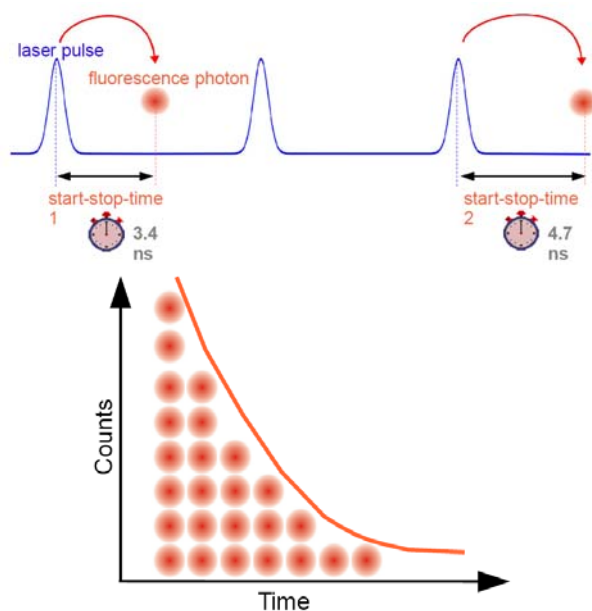


Figure 11. TCSPC measurement principle. Modified from literature [26].

2.3 Fluorescence resonance energy transfer (FRET)

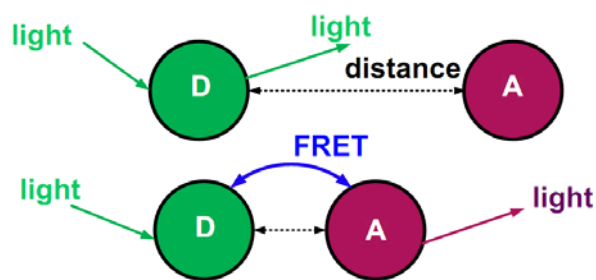


Figure 12. Schematic representation of FRET.

FRET (Figure 12) is the non-radiative transfer of excitation energy from a donor molecule to a nearby acceptor molecule [20, 27]. In turn, the fluorescence lifetime of the donor molecule decreases, the acceptor molecule emits a photon. The efficiency of FRET is sensitively dependent on the inverse sixth power of the distance between donor and acceptor molecules as illustrated in Figure 13 given by equation [20]:

$$E = \frac{R_0^6}{R_0^6 + r^6}$$

where r is the distance between a donor molecule and a acceptor molecule, E is the energy transfer efficiency, where R_0 is the Förster distance, that is, the distance between the donor and acceptor probe at which the energy transfer is (on average) 50% efficient [20, 27].

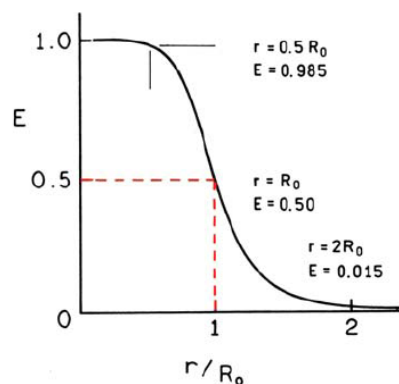


Figure 13. Dependence of the energy transfer efficiency (E) on distance. From literature [20].

2.3.1 Förster distance

The Förster distance is given by equation [21]:

$$R_0 = 0.211[(k^2 n^{-4} Q_D J(\lambda))]^{\frac{1}{6}} \quad \text{in } \text{Å}$$

where k^2 is a factor describing the relative orientation in space between the transition dipoles of the donor molecule and acceptor molecule, $J(\lambda)$ is the overlap integral between the donor fluorescence spectrum and the acceptor absorption spectrum (with the wavelength expressed in nanometers) as illustrated in Figure 14, n is the refractive index of the medium, and Q_D is the quantum yield of the donor molecule [20].

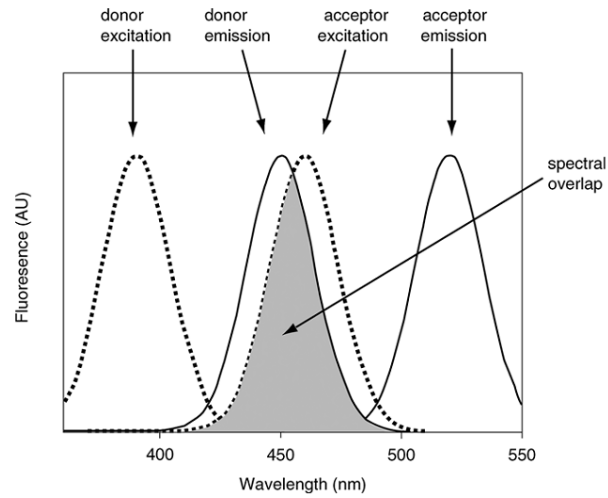


Figure 14. Schematic representation of the FRET spectral overlap integral. From literature [28].

2.3.2 Orientation Factor k^2

k^2 is given by equation:

$$k^2 = (\sin \theta_D \sin \theta_A \cos \phi - 2 \cos \theta_D \cos \theta_A)^2 = (\cos \theta_T - 3 \cos \theta_D \cos \theta_A)^2$$

In which θ_T is the angle between the emission transition dipole of the donor and the transition absorption dipole of the acceptor, θ_D and θ_A are the angles between these dipoles and the vector joining the donor and the acceptor, and ϕ is

the angle between the planes (illustrated in Figure 15) [20]. k^2 can change in a range from 0 to 4 depending on the relative orientation of donor and acceptor [20]. For head-to-tail parallel transition dipoles $k^2 = 4$, and for parallel dipoles $k^2 = 1$ [20]. As the sixth root is taken to calculate the distance, change of k^2 from 1 to 4 results in only a 26% change in r . $k^2 = 2/3$ is generally assumed for calculation of R_0 [20].

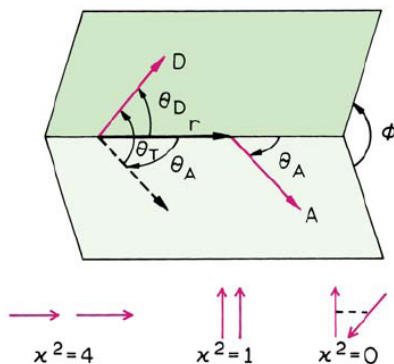


Figure 15. Dependence of the orientation factor κ^2 on the direction of the emission dipole of the donor and the absorption dipole of the acceptor. From literature [20].

FRET efficiency (E) can be measured based on the fluorescence intensities of the donor with acceptor (F_{DA}) and without acceptor (F_D) [20]:

$$E = 1 - \frac{F_{DA}}{F_D}$$

FRET efficiency (E) can also be detected from the lifetime of the donor in presence (τ_{DA}) and absence of the acceptor probe (τ_D) [20]:

$$E = 1 - \frac{\tau_{DA}}{\tau_D}$$

As FRET efficiency is dependent on the inverse sixth power of the distance between the donor and acceptor molecule, FRET method is a sensitive and import technique for investigating a variety of biological phenomena [29, 30]. FRET technique has been used widely to study the conformational dynamics of biomolecules at single molecule level [30]. In addition, FRET microscopy imaging has been applied widely to investigate the molecular interactions inside living cells with improved spatial resolution [29].

2.4 Fluorescence lifetime imaging microscopy (FLIM)

2.4.1 Confocal microscopy

Confocal microscopy was invented by Marvin Minsky, which spatially exclude the signal from the sample volume that reaches the detector and offers more accurate measurements than wide-field optical microscopy [31]. The laser beam is directed into a microscope objective via a dichroic mirror and focused on the sample. The fluorescence light emitted from the sample is collected by the same objective and passed through the dichroic and the emission filter. The pinhole is used as a spatial filter to block fluorescence light not originating from the focal plane, thus providing axial resolution [31]. Afterwards, the light is focused onto the detector (photomultiplier or avalanche photodiode) [31].

In order to obtain a confocal image, samples must be illuminated over the physically smallest possible area, which is known as the diffraction-limited spot.

The diameter of an diffraction-limited illumination spot is $d = 1.22 \frac{\lambda}{NA}$, where λ represents the excitation wavelength, NA is the numerical aperture of the objective used [32].

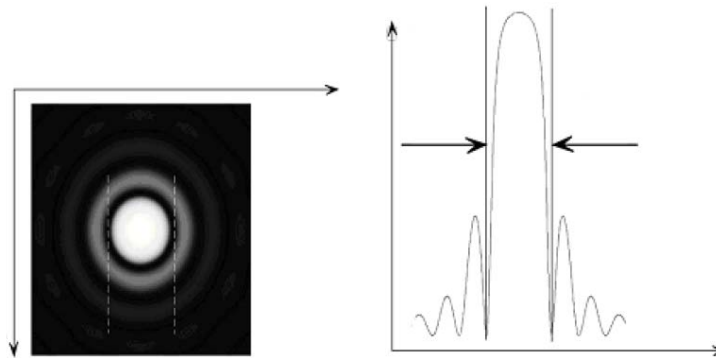


Figure 16. The diffraction-limited spot. An intensity profile (right). Modified from literature [32].

2.4.2 Fluorescence lifetime imaging microscopy (FLIM)

FLIM is a technique for producing an image based on the differences in fluorescence lifetime from a fluorescent sample [20, 33]. Fluorescence lifetimes are measured at each pixel, for each pixel a fluorescence decay curve is measured by TCSPC, the fluorescence lifetime of each pixel are displayed as color contrast (Figure 17) [20, 34]. The local changes in pH, ion concentrations, and temperature can be measured very accurately using FLIM because the lifetime of a fluorescent molecule is sensitive to its local microenvironment [20, 34].

2.4.3 FRET-FLIM

Conventional fluorescence microscopy has a limited spatial resolution (the diffraction limit is about 200 nm) [20, 37]. In order to visualize distances between molecules at a nanometer length scale, FRET studies are used since this process is strongly dependent on the distance r between the donor and acceptor molecules. Donor-to-acceptor distances are derived from the FRET efficiency, which can be measured from the lifetime of donor molecules measured by FLIM [37].

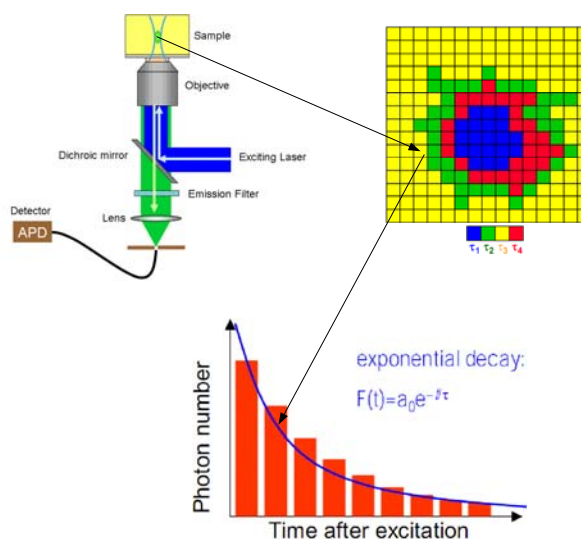


Figure 17. Illustration of FLIM. Modified from literature [35, 36].

2.5 Protein dynamics

Static 3-dimensional structure of protein does not completely explain protein functions, the conformational dynamics of a biomolecule is important to its biological functions. Many molecular processes, like enzymatic reactions, are closely connected to protein dynamics at different time scale [38, 39]. The goal of dynamics studies is to demonstrate how motion relates to function. Protein dynamics with atomic resolution and time resolution from femtoseconds to hours can be studied by Nuclear Magnetic Resonance (NMR) spectroscopy (Figure 18) [38, 39], in addition, single molecule fluorescence spectroscopy are also particularly informative about conformational dynamics, which allows to distinguish the individual behavior of molecules, thus remove time averaging that are present in ensemble methods [30]. Protein dynamics at the fast time scale of picosecond to nanosecond have been studied by measuring spin-lattice relaxation time (T_1) and spin-spin relaxation time (T_2) as well as Heteronuclear Nuclear Overhauser Effect (NOE) [39]. NMR relaxation dispersion measurements have been used to investigate protein dynamics in a slow time-range of microsecond to millisecond [40, 41, 42].

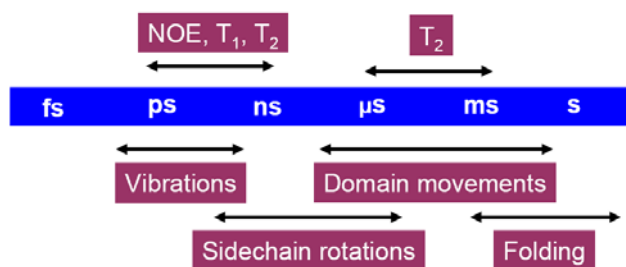


Figure 18. Time scales for protein dynamics studies. Modified from literature [38].

2.6 NMR relaxation analysis

A protein molecule has a much higher number of atoms than a small organic molecule, the basic one-dimension NMR spectrum has overlapping signals, and the spectrum assignment becomes difficult. Therefore, multidimensional NMR experiments have been developed to deal with this problem [43]. NMR spectroscopy has been used to study the dynamics and high resolution 3-dimensional structure of protein [44]. Although NMR spectroscopy is usually limited to smaller proteins (<30-40 KDa) [45], it is often the only way to obtain

structure information on partially or intrinsically unstructured proteins at the atom resolution [46].

In a NMR experiment, the bulk magnetization of the sample is perturbed from its equilibrium state, and the emitted signal is observed as the sample returns to equilibrium. Relaxation is the process by which nonequilibrium magnetization returns to the equilibrium state [47a]. An isotropic system without chemical exchange has two components: longitudinal or spin-lattice relaxation time (T_1) and transverse or spin-spin relaxation time (T_2). T_1 is the time constant to describe rate at which M_z component of magnetization returns to equilibrium after excitation. T_2 is the time constant to describe rate at which M_{xy} component of magnetization returns to equilibrium after excitation [47a].

In the studies of backbone NH group dynamics in proteins, it is typical to measure the ^{15}N longitudinal relaxation rate ($R_1=1/T_1$), the in-phase ^{15}N transverse relaxation rate ($R_2=1/T_2$), and the $\{^1\text{H}\}$ - ^{15}N heteronuclear Overhauser effect (NOE), which is given by the ratio of the ^1H saturated/unsaturated peak heights [47a]. All of these parameters are typically measured using two-dimensional ^1H - ^{15}N Heteronuclear Single-Quantum Coherence (HSQC) experiments [47a].

The relaxation rates are sensitive to molecular movement because the internal and global motions of protein cause the oscillating of local magnetic fields, which induce the restoring of nonequilibrium magnetization to the equilibrium state [47a].

2.6.1 Chemical Shift Anisotropy (CSA)

The chemical shift of a nucleus is a function of the orientation of the molecule in the magnetic field (B_0) (Figure 19) [47a, 48]. As the molecule tumbles in solution or the amide group oscillates relative to the remainder of the molecule, the ^{15}N nucleus is shielded to different extents from the permanent magnetic field (B_0), and hence the position of the ^{15}N nucleus experienced a fluctuating magnetic field, which can induce the relaxation of the ^{15}N nucleus [47a].

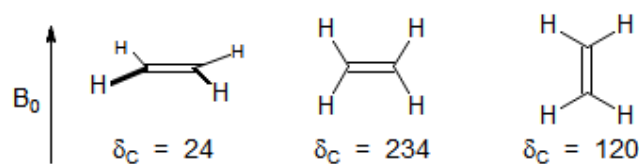


Figure 19. ^{13}C Chemical Shift Anisotropy (CSA). From literature [48].

2.6.2 The dipole-dipole mechanism

The dipole-dipole mechanism results from the fluctuating interaction (coupling) between a pair of magnetic nuclei as the internuclear vector rotates relative to the permanent magnetic field [47a]. As the N-H bond vector rotates, due to either molecular tumbling or internal structural fluctuations of the protein, the magnetic field that the ^1H nucleus induces at the position of the ^{15}N nucleus will vary [47a]. If this field fluctuates at the appropriate frequency, it will induce the relaxation of the ^{15}N nucleus [47a].

2.6.3 The role of conformational exchange

Overall R_2 of back bone amide ^{15}N spin relaxation is dominated by two contributions [47a]: ^1H - ^{15}N dipole-dipole (DD) and ^{15}N chemical shift anisotropy (CSA). However, conformational exchange on the μs - ms time scale can cause R_2 of NMR active atom (^1H or ^{15}N) sites experiencing varying chemical environment to be higher than that without the conformational fluctuations [47a]. Accordingly, we introduce a contribution R_{ex} to account for this excess effect [47a]: $R_2 = R_2^{DD} + R_2^{CSA} + R_{ex}$

2.6.4 Reduced spectral density mapping

The spectral density function $J(\omega)$ expresses the probability distribution of motional frequencies experienced by amide NH bond vectors undergoing random processes [47a]. The three experimentally measured relaxation parameters, R_1 , R_2 , and NOE can be transformed into the spectral density function at the five specific frequencies. The relationships between the three relaxation parameters for NH groups and the relevant values of the spectral

density function are dependent on linear combinations of the spectral density function evaluated at five critical frequencies, $J(0)$, $J(\omega_N)$, $J(\omega_H)$, $J(\omega_H + \omega_N)$ and $J(\omega_H - \omega_N)$, the relationship are described by Equation 1, 2 and 3 [47a]:

Equation 1:

$$R_1\left(\frac{1}{T_1}\right) = R_1^{DD} + R_1^{CSA} = \frac{d^2}{4} [J(\omega_H - \omega_N) + 3J(\omega_N) + 6J(\omega_H + \omega_N)] + c^2 J(\omega_N)$$

$$R_1^{DD} = \frac{d^2}{4} [J(\omega_H - \omega_N) + 3J(\omega_N) + 6J(\omega_H + \omega_N)]$$

$$R_1^{CSA} = c^2 J(\omega_N)$$

Equation 2:

$$R_2\left(\frac{1}{T_2}\right) = R_2^{DD} + R_2^{CSA} = \frac{d^2}{8} [4J(0) + J(\omega_H - \omega_N) + 3J(\omega_N) + 6J(\omega_H + \omega_N) + 6J(\omega_H)] + \frac{c^2}{6} [4J(0) + 3J(\omega_N)]$$

$$R_2^{DD} = \frac{d^2}{8} [4J(0) + J(\omega_H - \omega_N) + 3J(\omega_N) + 6J(\omega_H + \omega_N) + 6J(\omega_H)]$$

$$R_2^{CSA} = \frac{c^2}{6} [4J(0) + 3J(\omega_N)]$$

Equation 3:

$$NOE = 1 + \frac{d^2}{4} T_1 \left(\frac{\gamma_H}{\gamma_N} \right) [6J(\omega_H + \omega_N) - J(\omega_H - \omega_N)]$$

$$d = \left(\frac{\mu_0 h \gamma_N \gamma_H}{8\pi^2} \right) \left(\frac{1}{r_{NH}^3} \right)$$

$$c = \frac{\Delta\sigma_{NH} \omega_N}{\sqrt{3}}$$

where variables are given [47b]:

$\mu_0 = 4\pi \times 10^{-7}$ (m kg s⁻² A⁻²) is the permeability of free space;

$h = 6.6262 \times 10^{-34}$ (m² kg s⁻¹) is Planck's constant;

$\gamma_H = 26.75 \times 10^7$ rad T⁻¹ s⁻¹, the gyromagnetic ratio of proton;

$\gamma_N = -2.71 \times 10^7$ rad T⁻¹ s⁻¹, the gyromagnetic ratio of nitrogen;

$r_{\text{NH}} = 1.02 \times 10^{-10}$ m, the H-N bond length;

$\Delta\sigma_{\text{NH}} = -172 \times 10^{-6}$, the chemical shift anisotropy of the H-N bond of the amide proton, ^{15}N chemical shift anisotropy;

$\omega_{\text{N}} = -\gamma_{\text{N}}B_0$ rad/s, nuclear precession frequency of nitrogen, where B_0 is the magnetic field strength in Tesla (T), when measurement on Bruker 700 MHz NMR system (16.4 T), $\omega_{\text{N}} = 445776981$ rad/s.

The parameters d and c reflect the magnitude of the amide NH bond dipolar coupling interaction and the chemical shift anisotropy respectively [47a, 49]. It is clear from the equations that the determination of three relaxation parameters at one field strength does not allow for the solution of the five spectral densities. However, studies have demonstrated that the contributions of the high-frequency terms, $J(\omega_{\text{H}})$, $J(\omega_{\text{H}} + \omega_{\text{N}})$, and $J(\omega_{\text{H}} - \omega_{\text{N}})$, are roughly equivalent. Therefore, all of the high-frequency spectral densities $J(\omega_{\text{H}})$, $J(\omega_{\text{H}} + \omega_{\text{N}})$, and $J(\omega_{\text{H}} - \omega_{\text{N}})$ can be substituted by a single spectral density term, that is the average of $J(\omega_{\text{H}})$, $J(\omega_{\text{H}} + \omega_{\text{N}})$, and $J(\omega_{\text{H}} - \omega_{\text{N}})$, which can be approximated by $J(0.87\omega_{\text{H}})$ [50]. Therefore, the Equation 1, 2, and 3 can be simplified to Equation 4 to 6:

Equation 4:

$$R_1 = \frac{d^2}{4} [7J(0.87\omega_{\text{H}}) + 3J(\omega_{\text{N}})] + c^2 J(\omega_{\text{N}})$$

Equation 5:

$$R_2 = \frac{d^2}{8} [4J(0) + 13J(0.87\omega_{\text{H}}) + 3J(\omega_{\text{N}})] + \frac{c^2}{6} [4J(0) + 3J(\omega_{\text{N}})]$$

Equation 6:

$$\text{NOE} = 1 + \frac{d^2}{4} T_1 \left(\frac{\gamma_{\text{H}}}{\gamma_{\text{N}}} \right) [5J(0.87\omega_{\text{H}})]$$

The resulting expressions (Equation 7, 8 and 9) for $J(0)$, $J(\omega_{\text{N}})$, and $J(0.87\omega_{\text{H}})$ are derived through the inversion of Equation 4, 5 and 6. This reduced spectral density mapping method permits the calculation of $J(0)$, $J(\omega_{\text{N}})$, and $J(0.87\omega_{\text{H}})$ from a single set of T_1 , T_2 , and $\{^1\text{H}\}$ - ^{15}N NOE values [47, 49].

Equation 7:

$$J(0.87\omega_H) = R_1(NOE - 1) \left(\frac{\gamma_N}{\gamma_H} \right) \left(\frac{4}{5d^2} \right)$$

Equation 8:

$$J(\omega_N) = \frac{R_1 - J(0.87\omega_H) \left(\frac{7d^2}{4} \right)}{\left(\frac{3d^2}{4} + c^2 \right)}$$

Equation 9:

$$J(0) = \frac{R_2 - J(\omega_N) \left(\frac{7d^2}{4} \right) - J(0.87\omega_H) \left(\frac{13d^2}{8} \right)}{\left(\frac{d^2}{2} + \frac{2c^2}{3} \right)}$$

2.6.5 Lipari and Szabo model-free analysis

In Lipari-Szabo model-free analysis, internal and global motions of protein molecule are assumed to be independent [47a, 51-53]. The internal and global motions of protein cause the rotational motions of a bond vector (for example, $^1\text{H}-^{15}\text{N}$), which are defined by correlation function $C(t)$. Correlation function $C(t)$ is the probability that a bond vector (for example, $^1\text{H}-^{15}\text{N}$) has the same position at defined time zero and a later time t [47a]. Correlation function $C(t)$ is described by two exponential processes $C_I(t)$ and $C_O(t)$. We set $C(t) = C_O(t)C_I(t)$, where $C_O(t)$ describes the overall motion and $C_I(t)$ describes the internal motion [51, 52], given by

$$C_I(t) = S^2 + (1 - S^2)e^{-\frac{t}{\tau_e}}$$

where S^2 ($0 \leq S^2 \leq 1$) is the generalized order parameter, which indicates the spatial restriction of internal motion, and τ_e is an effective correlation time of $^1\text{H}-^{15}\text{N}$ internal motion [51, 52].

For overall isotropic motion, one has

$$C_O(t) = \frac{1}{5}e^{-\frac{t}{\tau_m}}$$

where τ_m is the global correlation time, which indicate the overall motion of a protein [47, 51, 52].

If the overall motion is anisotropic, we set [52]

$$C_o(t) = \frac{1}{5} \left[A e^{-\frac{t}{\tau_1}} + (1-A) e^{-\frac{t}{\tau_2}} \right]$$

where A ($0 \leq A \leq 1$), and τ_1, τ_2 are adjustable parameters that can be determined from the relaxation data for a nucleus attached to the protein backbone [52].

As the measurable relaxation parameters are more easily understood in terms of the probabilities of motions at specific frequencies, we set correlation functions on a frequency scale, which is achieved by Fourier transformation [47a, 51, 52] of the correlation function C(t) to give the spectral density function $J(\omega)$:

$$J(\omega) = 2 \int_0^{\infty} (\cos \omega t) C(t) dt$$

By Fourier transformation, the equation for the spectral density in the case of overall isotropic motion is obtained [47a, 52]:

$$J(\omega) = \frac{2}{5} \left[\frac{S^2 \tau_m}{1 + (\omega \tau_m)^2} + \frac{(1-S^2) \tau}{1 + (\omega \tau)^2} \right]$$

In some cases, it is necessary to introduce additional internal motion to explain the relaxation data [53]:

$$C_I(t) = S^2 + (1-S_f^2) e^{-\frac{t}{\tau_f}} + (S_f^2 - S^2) e^{-\frac{t}{\tau_s}}$$

where $S^2 = S_f^2 S_s^2$, the two order parameters S_s^2 and S_f^2 are for the slow and fast motions respectively.

The diffusion-in-a-cone model is used to interpret S^2 [47a]. The N-H bond vector is assumed to diffuse freely within a cone defined by semiangle θ [47a]. The S^2 is related to θ , as shown in Figure 20, S^2 decreases from 1 to 0 with increasing θ from 0° to 90° [47a]. The N-H bond vector is assumed to alternate between two states i and j, described by a separation angle φ in a two-site jump motional model, as show in Figure 20 [47a], S^2 is related to the angle φ . The

combined diffusion-in-a-cone and two-site jump models for internal bond vector motions is proposed to describe internal bond vector, as shown in Figure 20, the N-H bond vector can jump between two cones at slow time scale or diffuse within each cone at fast time scale [47a].

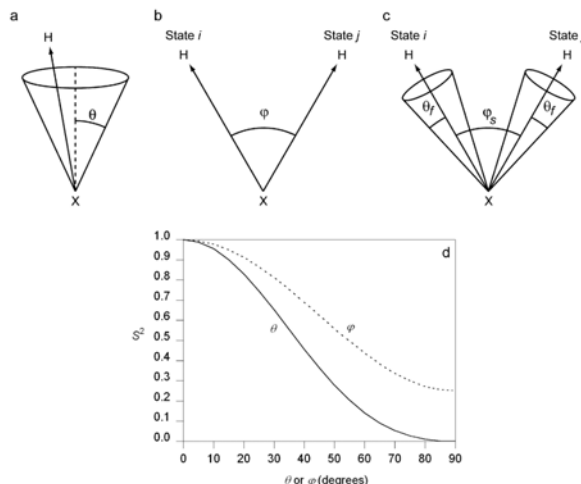


Figure 20. Motional models for interpretation of model-free order parameters. From literature [47].

The model free analysis does not provide a detailed physical picture of the internal motions [47], it defines some specific models to describe the details of the internal and global motions, and then to fit these motional models to the relaxation data to check and determine the “closest” description of motions [47].

2.6.6 CPMG (Carr-Purcell-Meiboom-Gill) relaxation dispersion NMR experiment

The relaxation dispersion NMR experiment uses spin-echo pulse trains to suppress relaxation due to exchange processes on the μs – ms timescale [40, 41]. The CPMG frequency can be calculated from the number of spin-echo pulses applied during an interval of fixed duration [40, 41]. The effective transverse relaxation rate, $R_{2,eff}$ is calculated as a function of a variable number of 180° refocusing pulses applied during an interval of fixed duration T, as shown in Figure21 [40, 41].

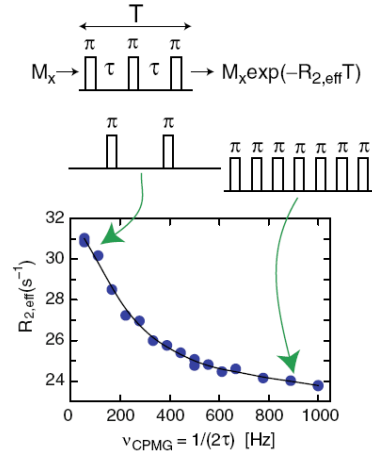


Figure 21. Scheme of CPMG-based NMR relaxation dispersion spectroscopy. From literature [41]

The response of $R_{2,eff}$ to $\nu_{CPMG} = 1/(2\tau)$ can be calculated from the Equation 1 and analyzed with the Equation 2 to extract the kinetic and thermodynamic parameters that govern the exchange process in the case of fast exchange between the state A and state B of protein [54, 55].

Equation 1:

$$R_{2,eff}(\nu_{CPMG}) = -\frac{1}{T} \ln \left[\frac{I(\nu_{CPMG})}{I_0} \right]$$

Here, $I(\nu_{CPMG})$ is the peak intensity in the spectrum measured at ν_{CPMG} , I_0 is the peak intensity in the reference spectrum recorded without the CPMG relaxation delay.

Equation 2:

$$R_{2,eff}(\nu_{CPMG}) = \left(1 - \frac{4\nu_{CPMG}}{k_{ex}} \tanh \frac{k_{ex}}{4\nu_{CPMG}} \right) p_A p_B \left(\frac{\Delta\omega^2}{k_{ex}} \right) + R_{2,eff}(\nu_{CPMG} \rightarrow \infty)$$

In Equation 2, k_{ex} is the sum of forward and reverse rates of inter-conversion, p_A is relative populations of the exchanging species (major contribution: highly populated conformers), p_B is relative populations of the exchanging species (low populated and transient conformers, which play important roles in biological

function), and $\Delta\omega$ is the differences in the chemical shifts for spins in state A and state B [54-56].

2.6.7 Applications to specific proteins

A substantial number of NMR dynamics studies have showed the effects of binding of a ligand on protein dynamics, which revealed that dynamics can play a role in regulating the binding affinity [47a]. Human cyclophilin A (CypA) is a peptidyl-prolyl cis/trans isomerase that catalyzes the interconversion between cis and trans conformations of Suc-Ala-Ala-Pro-Phe-4-NA peptide bonds [39]. The conformational fluctuations of the active site of CypA were studied by NMR relaxation experiment [39]. R_2 experiments (Figure 22) indicated that protein undergoes slow conformational exchange in specific regions of CypA during catalysis [39].

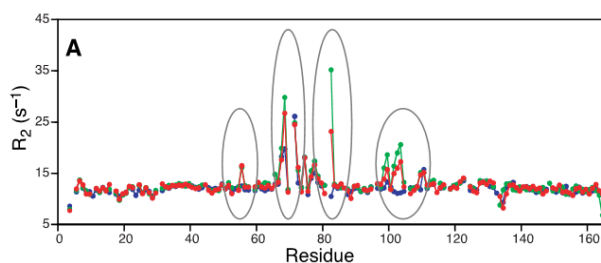


Figure 22. Comparison of ^{15}N R_2 rate constants between free CypA (dark blue) and CypA during catalysis (2.86 mM substrate, red). From literature [39].

References of chapter 2

- [1] http://en.wikipedia.org/wiki/Targeted_drug_delivery.
- [2] Kresge, C. T.; Leonowicz, M. E.; Roth, W. J.; Vartuli, J. C.; Beck, J. S. *Nature* 1992, 359, 710-712.
- [3] Zhao, D.; Feng, J.; Huo, Q.; Melosh, N.; Fredrickson, G. H.; Chmelka, B. F.; Stucky, G. D. *Science* 1998, 279, 548-552.
- [4] Akçakayran, D. PhD thesis (TUB), 2009.
- [5] Vallet-Regí, M.; Balas, F.; Arcos, D. *Angew. Chem. Int. Ed.* 2007, 46, 7548-7558.

- [6] Schlossbauer, A.; Dohmen, C.; Schaffert, D.; Wagner, E.; Bein, T. *Angew. Chem. Int. Ed.* 2011, 50, 6828-6830.
- [7] Cauda, V.; Argyo, C.; Schlossbauer, A.; Bein, T. *J. Mater. Chem.* 2010, 20, 4305-4311.
- [8] Song, S.-W.; Hidajat, K.; Kawi, S. *Langmuir* 2005, 21, 9568-9575.
- [9] Van Speybroeck, M.; Barillaro, V.; Thi, T. D.; Mellaerts, R.; Martens, J.; Van Humbeeck, J.; Vermant, J.; Annaert, P.; Van den Mooter, G.; Augustijns, P. *J. Pharm. Sci.* 2009, 98, 2648-2658.
- [10] Vallet-regi, M.; Rámila, A.; del Real, R. P.; Pérez-Pariente, J. *Chem. Mater.* 2001, 13, 308-311.
- [11] Li, Z.; Barnes, J. C.; Bosoy, A.; Stoddart, J. F.; Zink, J. I.; *Chem. Soc. Rev.* 2012, 41, 2590-2605.
- [12] Vallet-Regí, M.; Balas, F.; Arcos, D. *Angew. Chem. Int. Ed.* 2007, 46, 7548-7558.
- [13] Nguyen, T. D.; Tseng, H. R.; Celestre, P. C.; Flood, A. H.; Liu, Y.; Stoddart, J. F.; Zink, J. I. *Proc. Natl. Acad. Sci. USA* 2005, 102, 10029-10034.
- [14] Lai, C.-Y.; Trewyn, B. G.; Jeftinija, D. M.; Jeftinija, K.; Xu, S.; Jeftinija, S.; Lin, V. S. Y. *J. Am. Chem. Soc.* 2003, 125, 4451-4459.
- [15] Liu, R.; Zhang, Y.; Zhao, X.; Agarwal, A.; Mueller, L. J.; Feng, P. *J. Am. Chem. Soc.* 2010, 132, 1500-1501.
- [16] Vivero-Escoto, J. L.; Slowing, I. I.; Wu, C.; Lin, V. S.-Y. *J. Am. Chem. Soc.* 2009, 131, 3462-3463.
- [17] Zhu, C.; Lu, C.; Song, X.; Yang, H.; Wang, X. *J. Am. Chem. Soc.* 2011, 133, 1278-1281.
- [18] Schlossbauer, A.; Kecht, J.; Bein, T. *Angew. Chem. Int. Ed.* 2009, 48, 3092-3095.
- [19] <http://en.wikipedia.org/wiki/Fluorescence>.
- [20] Lakowicz, J. R. *Principles of Fluorescence Spectroscopy*, 3rd ed.; Springer: New York, 2006.
- [21] <http://www.olympusmicro.com/primer/techniques/fluorescence/fluorescenceintro.html>.
- [22] <http://micro.magnet.fsu.edu/primer/java/fluorescence/photobleaching/index.html>.

- [23] Yang, H.; Luo, G.; Karnchanaphanurach, P.; Louie, T.-M.; Rech, I.; Cova, S.; Xun, L.; Xie, X. S. *Science* 2003, 302, 262-266.
- [24] <http://www.boselec.com/products/sigtcspscwhat.html>.
- [25] Eggeling, C.; Fries, J. R. Brand, L.; Günther, R.; and Seidel, C. A. M. *Proc. Natl. Acad. Sci. USA* 1998, 95, 1556–1561.
- [26] http://www.picoquant.de/technotes/technote_tcspc.pdf.
- [27] Berezin, M. Y.; Achilefu, S. *Chem. Rev.* 2010, 110, 2641-2684.
- [28] Groemping, Y.; Hellmann, N. *Curr. Protoc. Protein Sci.* 2005, 20.8.1-20.8.27.
- [29] Sekar, R. B.; Periasamy, A. *J. Cell. Biol.* 2003, 160, 2003, 629-633.
- [30] (a) Michalet, X.; Weiss, S.; Jäger, M. *Chem. Rev.* 2006, 106, 1785-1813.
(b) Weiss, S. *Science* 1999, 283, 1676-1683.
- [31] (a)http://en.wikipedia.org/wiki/Confocal_microscopy.
(b)<http://www.biophysics.org/portals/1/pdfs/education/schwille.pdf>
- [32] Leica TCS SP5/Leica TCS SP5 X user manual.
- [33] http://en.wikipedia.org/wiki/Fluorescence-lifetime_imaging_microscopy.
- [34] Sun, Y.; Day, R. N.; Periasamy, A. *Nat. Protoc.* 2011, 6, 1324-1340.
- [35] Picoquant manual.
- [36] <http://www.mpip-mainz.mpg.de/~koynov/koynov/research/fcs.html>.
- [37] Wallrabe, H.; Periasamy, A. *Curr. Opin. Biotechnol.* 2005, 16, 19-27.
- [38] (a)Henzler-Wildman, K.; Kern, D. *Nature* 2007, 450, 964-972.
(b)http://www.bioc.aecom.yu.edu/labs/girvlab/nmr/course/COURSE_2012/Lecture_RelaxationDynamics_2012.pdf
- [39] Eisenmesser, E. Z.; Bosco, D.; Akke, M.; Kern, D. *Science* 2002, 297, 1520-1523.
- [40] Korzhnev, D. M.; Kay, L. E.; *Acc. Chem. Res.* 2008, 41, 442-451.
- [41] Hansen, D. F.; Vallurupalli, P.; Kay, L. E. *J Biomol. NMR* 2008, 41, 113-120.
- [42] Eisenmesser, E. Z.; Millet, O.; Labeikovsky, W.; Korzhnev, D. M.; Wolf-Watz, M.; Bosco, D. A.; Skalicky, J. J.; Kay, L. E.; Kern, D. *Nature* 2005, 438, 117-121.
- [43] Aue, W. P.; Bartholdi, E.; Ernst, R. R. *J. Chem. Phys.* 1976, 64, 2229-2246.
- [44] Wuthrich, Kurt. *NMR of proteins and nucleic acids*. Wiley, 1986.

- [45] Snyder, D. A., et al. *J. Am. Chem. Soc.* 2005, 127, 16505-16511.
- [46] http://en.wikipedia.org/wiki/Nuclear_magnetic_resonance_spectroscopy.
- [47] (a) Jarymowycz, V. A.; Stone, M. J., *Chem. Rev.* 2006, 106, 1624-1671.
(b) Kneller, J. M.; Lu, M.; Bracken, C. J. *Am. Chem. Soc.* 2002, 124, 1852-1853.
- [48] <http://www.chem.wisc.edu/areas/reich/nmr/08-tech-01-relax.htm>.
- [49] Henkels, C. H.; Chang, Y.; Chamberlin, S. I.; Oas, T. G. *Biochemistry* 2007, 46, 15062-15075.
- [50] Quinternet, M.; Tsan, P.; Selme, L.; Beaufils, C.; Jacob, C.; Boschi-Muller, S.; Averlant-Petit, M.-C.; Branlant, G.; Cung, M.-T. *Biochemistry*, 2008, 47, 12710-12720.
- [51] Lipari, G.; Szabo, A. *J. Am. Chem. Soc.* 1982, 104, 4546-4559.
- [52] Lipari, G.; Szabo, A. *J. Am. Chem. Soc.* 1982, 104, 4559-4570.
- [53] Clore, G. M.; Szabo, A.; Bax, A.; Kay, L. E.; Driscoll, P. C.; Gronenborn, A. M. *J. Am. Chem. Soc.* 1990, 112, 4989-4991.
- [54] Wang, C.; Grey, M. J.; Palmer, A. G. *J. Biomol. NMR* 2001, 21, 361-366
- [55] Bieri, M.; Gooley, P. *BMC Bioinformatics* 2011, 12, 421.
- [56] Baldwin, A. J.; Kay, L. E. *Nat. Chem. Biol.* 2009, 5, 808-814.

3 Experimental section

The section 3.2 to 3.6 demonstrate the preparation and characterization of mesoporous silica materials, which are used for Chapter 4 and Chapter 5, and the adsorption of lysozyme and rhodamine b on mesoporous silica, the release experiment of rhodamine b are shown in the section 3.3. The section 3.4.5 shows the measurements on mesoporous silica doped with the fluorescein and rhodmine by Fluorescence lifetime imaging microscopy (FLIM).

The section 3.7 to 3.10 shows the preparation and purification of ^{15}N labeled DHP A, and the NMR experiments for chapter 6.

3.1 Chemicals

Lysozyme (Sigma-Aldrich, L6876, protein $\geq 90\%$), Tetraethyl orthosilicate (TEOS) (ABCR, AV14965, 98%), Hexa-decyltrimethylammonium bromide (CTAB) (Sigma-Aldrich, H5882, $\geq 98\%$), Tetradecyltrimethylammonium bromide (TTAB) (Aldric, $\geq 99\%$), Atto 647N-NHS (ATTO-TEC, AD 647N-31), Sodium phosphate dibasic dehydrate (Sigma-Aldrich, 30142, $\geq 99.5\%$), Sodium phosphate monobasic monohydrate (Sigma-Aldrich, 71504, $\geq 99\%$), Deuterium oxide (Sigma-Aldrich, 151882, 99.9 atom % D), Biotin (Sigma-Aldrich, B4501, $\geq 99\%$), Hemin (Sigma-Aldrich, 51280, $\geq 98\%$), Ampicillin sodium salt (Sigma-Aldrich, A0166), Thiamine (Fisher scientific, BP892), and Ammonium chloride (Cambridge isotope laboratories, ^{15}N , 99%). All chemicals were used as received.

3.2 Preparation of MCM-41 silica particles

Mesoporous silica nanoparticles (designated MCM16-N) were synthesized using a procedure similar to the reported procedure [1]: 1.0 g of CTAB was dissolved in 480 mL of deionized water, and 3.5 mL of 2 M NaOH (aq) was

added to the solution. After raising temperature to 80 °C, 5.0 mL of TEOS was added under vigorous stirring, and the reaction mixture was kept at this temperature for 2 h under continued stirring. The precipitate was separated from the supernatant by filtration, washed extensively with deionized water, dried and calcined in air at 550 °C to remove the organic template from the mesopores. Conventional MCM-41 silica of a somewhat smaller pore size (designated MCM14) was synthesized according to our earlier work using TTAB as the structure-directing template [2]. Also, conventional MCM-41 silica was prepared by using CTAB as the structure-directing template [2].

3.3 Loading, capping and release experiments

Samples for the pH-responsive drug release experiments were prepared as follows. 2 mg of MCM-41(C16) or MCM-41(C14) was suspended in 1 mL of a 0.6 mM rhodamine B buffer solution (50 mM phosphate buffer, pH 7) and stirred for 24 h at room temperature. 0.4 mL of a 9 mg/mL solution of lysozyme in phosphate buffer (50 mM, pH7) was then added to the suspension and the mixture was stirred for another 24 h. The precipitate was then separated from the supernatant by centrifugation (9000 rpm) and placed in a 1 mL phosphate buffer solution (50 mM, pH 2). After 24 h, the supernatant with the excess amount of rhodamine B was removed by centrifugation (9000 rpm). The sample was washed 5 times with pH 2 buffer solution. To investigate the pH-responsive release, dye-loaded silica particles were redispersed in 30ml pH 2 buffer solution. Activation of guest molecule release from mesoporous silica was accomplished by adjusting the pH values of the solution with addition of 12 M NaOH solution. Release profiles were obtained by plotting the absorbance intensity of rhodamine B in solution at 555 nm as a function of time.

3.4 Characterization of silica host materials

3.4.1 SAXS

Small-angle X-ray scattering profiles of the MCM-41 samples were measured on a SAXSess mc² instrument (Anton Paar, Austria). Data reduction and desmearing was performed using the Saxsquant 3.50 software.

3.4.2 TEM

TEM images were obtained with a 200 kV TECNAI G² 20 S-TWIN. Images of the MCM-41(C16) nanoparticles and MCM-41(C14) particles are shown in Figure 2a,

3.4.3 Nitrogen Sorption

Nitrogen adsorption isotherms (77 K) were measured by gas volumetry using a Quantachrome Quadrisorb SI instrument in combination with the Quantachrome Quadrawin Data Acquisition and Reduction software.

3.4.4 CLSM analysis

Loading of the mesoporous silica materials with rhodamine B was checked by confocal laser scanning microscopy (CLSM). CLSM images were obtained on a LEICA SP 5II system. The samples were prepared by transferring a drop of sample solution onto a cover slip. The cover slip was then sandwiched with another cover slip.

3.4.5 Fluorescence lifetime imaging

Fluorescence lifetime imaging microscopy (FLIM) was performed using a Leica TCS SP5 II confocal microscope system. A 470 nm picosecond pulsed laser (40 MHz, PicoQuant, Berlin, Germany) was used as the excitation source. The laser beam was delivered to the sample through an apochromatic 63 \times , 1.2 NA water immersion objective and the emitted fluorescence was collected using the same objective. The fluorescence was collected and filtered by suitable emission filters before being detected by single photon avalanche photodiodes (SPAD). The experiments were performed using two detectors to monitor the fluorescence of the donor (500-550 nm emission filter) and of the acceptor (647-703 nm emission filter) after excitation at 470 nm. Fluorescence was measured

using a time-correlated single photon counting (TCSPC) module in the time-tagged time-resolved (TTTR) mode.

3.5 Protein adsorption

Protein adsorption in the MCM-41 materials was measured at pH 7 using 50 mM phosphate buffer. Samples with a given amount of silica and increasing amounts of protein were prepared and equilibrated at 25 °C for 48 h by means of a multiple axel rotor. After centrifugation the supernatant was analyzed by UV/Vis spectroscopy.

3.6 lysozyme labeling

Atto647N-labeled Lysozyme was prepared by reacting 2.5 mg/ml mM aliquots of protein with a 2-fold molar excess of Atto 647N-NHS ester in 100 mM NaHCO₃. Excess dye was removed using a PD-10 column pre-equilibrated with 50 mM pH 7 phosphate buffer. The labeling efficiency was estimated to be ~ 40% based on the absorbance method described by the dye manufacturer.

3.7 Expression and purification of ¹⁵N labeled DHP A [3-8]

The pET 16b vector containing the 6XHis-tagged DHP A DNA insert was transformed into BL21 (DE3) Escherichia coli cells, and were plated onto LB agar plates containing 100 µg/mL Amp and allowed to grow for about 12 h at 37 °C. Transfer one or more E. coli colonies to 5 ml LB broth supplemented with 100 µg/mL ampicillin and grow cells at 37 °C in a shaking incubator for 1d. Spin down the cells at 1200 g for 15 min at 25 °C. Re-suspend a fraction of cells (pellet) in 10 ml of isotopically labeled M9 minimal media and grow cells at 37 °C for 17 h. Pour the starter culture into 90 ml of isotopically labeled M9 minimal media supplemented with 60 mg/L hemin and grow cells at 37 °C for 6 h. Pour the 100 ml of culture into remaining 900 ml of isotopically enriched M9 media supplemented with 60 mg/L hemin and grow the cells at 37 °C for 12 h.

Induce overexpression with 0.25 mM Isopropyl-beta-D-1-thiogalactopyranoside(IPTG), the growth temperature was reduced to room temperature and cells were allowed to grow for 23 h. The cells were collected via centrifugation at 7000 g at 4 °C for 20 min and then allowed to freeze overnight at -70 °C. The cells were resuspended in a 50 ml of lysis buffer (50 mM NaH₂PO₄, 300 mM NaCl, and 10 mM imidazole, adjust to pH 8 with NaOH), lysozyme, DNase I, and RNase A were added to a final concentration of 5 mg/mL, and 0.05 mg/ml, 0.17 mg/mL, respectively. The cell slurry was allowed to stir at 4 °C for 2h. The cells were centrifuged at 17000 g for 30 min, and the supernatant solution was collected. The supernatant solution was then applied to a Ni-NTA agarose column, and washed with 50 mM NaH₂PO₄, 300 mM NaCl, and 20 mM imidazole buffer (pH 8), and eluted with 50 mM NaH₂PO₄, 300 mM NaCl, and 250 mM imidazole buffer (pH 8). The isolated His-DHP A was oxidized by K₃[Fe(CN)₆] and buffer exchanged in 20 mM KH₂PO₄ buffer (pH 6) by using a Sephadex G-25 column. The protein was further purified on a CM 52 column. The His-DHP A was washed and eluted with 20mM pH 6 KH₂PO₄ buffer and 150 mM KH₂PO₄ buffer (pH 7), respectively. Purified His-DHP A was exchanged in 100 mM potassium phosphate buffer (pH 7) by G-25 column. The protein was concentrated to a final concentration of about 1.6 mM by using an Amicon Ultra device (10, 000 MWCO, Millipore). KCN was added to an approximately 10-fold excess, and then 10% of 100 mM potassium phosphate D₂O buffer (corresponding to pH 7) was added for NMR measurement.

M9 minimal medium containing ¹⁵NH₄Cl as the sole N source and glucose as sole C source [3, 4]

For 1 liter media, 6.5 g Na₂HPO₄, 3g KH₂PO₄ and 0.5g NaCl, 1g ¹⁵NH₄Cl, 4 g glucose, 10 mg thiamin, 10 mg biotin, 100 mg ampicillin, 11 mg CaCl₂, 120 mg MgSO₄ were dissolved in 1 liter water and then filter sterilize.

3.8 NMR spectroscopy

NMR samples: 1.6 mM ^{15}N labeled DHP A with 3 mM TCP, and 0.65 mM ^{15}N labeled DHP A without TCP. All NMR experiments were performed on 700 MHz or 500 MHz AVANCE Bruker NMR spectrometer at 25 °C. T_1 , T_2 and $\{^1\text{H}\}$ - ^{15}N heteronuclear NOE measurements were made on a 700 MHz AVANCE Bruker spectrometer. T_2 values (DHP A with TCP) were obtained with different durations of the delay T (s): 0.015, 0.03, 0.045, 0.06, 0.075, 0.09, 0.105, 0.12, 0.155, 0.17, 0.195, and 0.21. T_1 values (DHP A with TCP) were determined with the delay T (s): 0.01, 0.02, 0.04, 0.07, 0.11, 0.14, 0.18, 0.22, 0.28, 0.33, 0.39, 0.46, 0.54, 0.65, 0.79, 1, and 1.2. T_2 values (DHP A) were obtained with different durations of the delay T (s): 0.02, 0.04, 0.06, 0.08, 0.11, 0.14, 0.17, and 0.24. R_1 values (DHP A) were determined with T (s): 0.01, 0.02, 0.04, 0.07, 0.11, 0.14, 0.18, 0.22, 0.28, 0.33, 0.39, 0.46, 0.54, 0.65, 0.79, and 1.2. $\{^1\text{H}\}$ - ^{15}N heteronuclear NOE values were measured from the ratio of the intensity of $\{^1\text{H}$ - $^{15}\text{N}\}$ -HSQC peaks in the presence and absence of proton saturation [9].

3.9 NMR data processing

All spectra were processed using Bruker software suite Topspin (version 3.1) [10]. The ^1H dimension was zero-filled to 4096 points while the indirectly detected ^{15}N dimension was zero-filled to 2048 points. Both dimensions were apodized with shifted qsine.

The processed spectra were analyzed with Bruker protein dynamics center [10]. T_1 and T_2 relaxation times of an amide ^{15}N nucleus were obtained by fitting the cross peak intensity over the time delay series, $I(t)$, to a two parameter single-

exponential decay function $I(t) = I_0 \times \exp\left(-\frac{t}{T_1}\right)$ and $I(t) = I_0 \times \exp\left(-\frac{t}{T_2}\right)$

where $I(0)$ is the best-fit value for the peak intensity at zero time [9].

3.10 UV-Vis enzymatic assays [5, 6, 8]

^{15}N labeled DHP A was oxidized via addition of excess $\text{K}_3[\text{Fe}(\text{CN})_6]$. The excess ferricyanide was removed, and DHP A was buffer exchanged into in 100 mM pH 7 potassium phosphate buffer by a SephadexG-25 gel-filtration column. The absorption data were measured on a Hewlett-Packard 8453 multiwavelength spectrometer. Spectra were collected every 5 s over a 92 s time frame. The conditions used for the assays were 2.5 μM DHP A, 120 μM TCP, and 1250 μM H_2O_2 . Turnover of the halophenols was determined by the disappearance of the absorption bands of TCP at 313 nm at potassium phosphate buffer and appearance of product absorption bands of 2, 6-dichloro-1,4-benzoquinone (2,6-DCQ) at 272 nm.

References of chapter 3

- [1] Radu, D. R.; Lai, C.-Y.; Jeftinija, K.; Rowe, E. W.; Jeftinija, S.; Lin, V. S. Y. *J. Am. Chem. Soc.* 2004, 126, 13216-13217.
- [2] Jähnert, S.; Vaca Chávez, F.; Schaumann, G. E.; Schreiber, A.; Schönhoff, M.; Findenegg, G. H. *Phys. Chem. Chem. Phys.* 2008, 10, 6039-6051.
- [3] Tugarinov, V.; Kanelis, V.; Kay, L. E. *Nat. Protoc.* 2006, 1, 749-754.
- [4] Lundström, P.; Vallurupalli, P.; Hansen, D F.; Kay, L. E. *Nat. Protoc.* 2009, 4, 1641-1648.
- [5] Davis, M. F.; Bobby, B. G.; Franzen, S. *Biochemistry* 2010, 49, 1199-1206.
- [6] Davis, M. F.; Gracz, H.; Vendeix, F. A. P.; de Serrano, V.; Somasundaram, A.; Decatur, S. M.; Franzen, S. *Biochemistry* 2009, 48, 2164-2172.
- [7] Belyea, J.; Gilvey, L. B.; Davis, M. F.; Godek, M.; Sit, T. L.; Lommel, S. A.; Franzen, S. *Biochemistry* 2005, 44, 15637-15644.
- [8] Ma, H.; Thompson, M. K.; Gaff, J.; Franzen, S. *J. Phys. Chem. B* 2010, 114, 13823-13829.

- [9] Farrow, N. A.; Muhandiram, R.; Singer, A. U.; Pascal, S. M.; Kay, C. M.; Gish, G.; Shoelson, S. E.; Pawson, T.; Forman-Kay, J. D.; and Kay, L. E. *Biochemistry* 1994, 33, 5984-6003.
- [10] <http://www.bruker.com/en/products/mr/nmr/nmr-software/software.htm>.

4 Lysozyme as a pH-responsive valve for controlled release of guest molecules from mesoporous silica *

4.1 Introduction

Stimuli-responsive controlled-release systems are receiving much attention because of their potential application in targeted drug delivery [1]. Surface-functionalized, end-capped mesoporous silica particles hold great promise for controlled-release carriers, due to their well-defined pore geometry, tunable pore size, large pore volume and chemical stability [2]. Different kinds of capping agents, including inorganic nanoparticles [3], organic molecules [4], supramolecular assemblies [5], and polymers [6] have been employed to construct mesoporous silica-based carrier systems for controlled drug release. However, regardless of these achievements, many of the existing capping systems have disadvantages including their toxicity and poor biocompatibility. In particular, despite recent reports on mesoporous silica-based devices equipped with protein caps [7], the utility of mesoporous silica involving biomolecules for real delivery systems is still in its infancy.

Here we report a simple and effective system for controlled drug delivery which uses lysozyme as a pH-responsive valve to block and unlock the pores of MCM-41 silica particles. Hen egg lysozyme is a small globular protein (129 amino acid residues) of prolate spheroid shape (dimensions 3.0×3.0×4.5 nm) [8], stabilized by four internal disulfide bridges, and with a net charge of +7.5e at pH 7 and +17e at pH 2 [9]. Its hydrodynamic radius R_h is 1.9 nm (at pH 4.5) [10], but a study based on dielectric relaxation measurements [11] indicated an increase to a significantly higher value ($R_h = 2.3$ nm) at pH 3, suggesting an increase of the effective size of the lysozyme molecule in the strongly acidic

* modified from published article Lysozyme as a pH-Responsive valve for controlled release of guest molecules from mesoporous silica, Mengjun Xue, Gerhard H. Findenegg, Langmuir, 2012, 28, 17578-17584.

regime, which was attributed to inner repulsive electrostatic interactions caused by the high net charge in this pH regime. pH-induced denaturation or conformational changes are well-known for structurally less stable proteins, such as cytochrome-c [12] or serum albumin [13].

MCM-41 type mesoporous silica nanoparticles constitute arrays of cylindrical pores of uniform size that can be controlled to a precision of a few Ångstrom in a range from 2 to 5 nm. Silica has its isoelectric point in the strongly acidic regime (IEP \sim 2), implying that silica surfaces are negatively charged under most conditions [14]. The adsorption level of lysozyme at silica surfaces and on silica nanoparticles is strongly varying with pH, from almost no adsorption at the IEP of silica to high levels at pH 7 and beyond [15]. In mesoporous silica the adsorption level of proteins can be limited by the pore size. For typical MCM-41 materials the pore size is only marginally larger than the effective diameter of lysozyme molecules. Uptake of lysozyme into the pores is slow and not exceeding low levels over a period of days, suggesting that adsorption is restricted to the region near the pore entrances [16]. In an attempt to study the pH dependent adsorption behavior of lysozyme in MCM-41 nanoparticles we observed an unexpected pH reversible pore blocking effect by lysozyme when pH was lowered from pH 7 to pH 2. This observation suggests that the protein molecules adsorbed near the pore entrances endow these materials with a capability of a molecular switch. Hence, a pH-responsive lysozyme@MCM-41 carrier system may be obtained if lysozyme in the pores can form gates for drug molecules at low pH.

The present work represents a proof of principle for a controlled release system based on this concept. MCM-41 particles are loaded with the cationic dye rhodamine B, which serves as a model drug, and the adsorption and pH-responsive pore blocking of lysozyme is used to confine the drug in the carrier particles. To release the drug, the pores are unlocked by returning to the original pH value.

4.2 Results

4.2.1 Characterization of mesoporous silica

MCM16-N nanoparticles are shown in TEM in Figure 1a. They have a typical size of 100 to 200 nm and exhibit ordered arrays of mesopores that span the entire particle (see inset). The high degree of structural order of the material is confirmed by XRD. The diffraction profile (Figure 1b) exhibits the leading Bragg peaks of a 2D hexagonal lattice. The lattice constant a_0 derived from the peak positions of the two materials is given in Table 1. The nitrogen adsorption isotherms

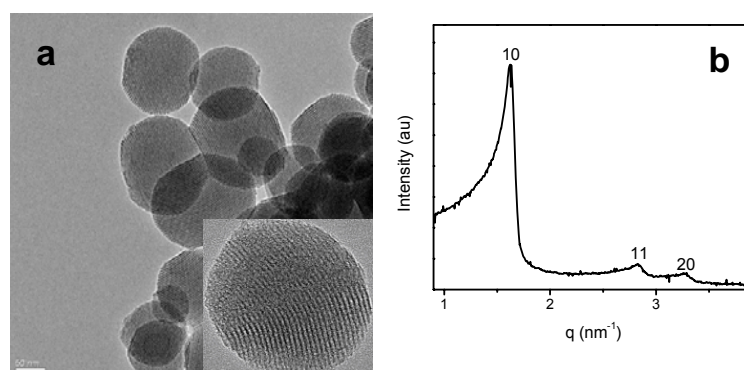


Figure 1. MCM16-N silica nanoparticles: (a) TEM image; (b) XRD profile

for the two materials, shown in Figure 2a, exhibit type IV characteristics with negligible (MCM14) or narrow (MCM16-N) pore condensation hysteresis, as to be expected for open cylindrical pores of 3 to 4 nm diameter [17]. The adsorption isotherms were analysed by the nonlocal density functional theory (NLDFT) kernel for cylindrical silica pores [18]. The pore size distribution (PSD) resulting from this analysis is shown in Figure 2b, and the specific pore volume, specific surface area, mean pore diameter D_{DFT} of the two samples are given in Table 1. Also given in this table is the mean pore diameter D_{KJS} as derived from the pore condensation pressure by the KJS method [19]. For both materials D_{KJS} is lower than D_{DFT} by about 0.1 nm. Below we adopt the following mean pore diameters D for the two materials: 3.7 nm (MCM16-N) and 3.5 nm (MCM14). For both samples we thus find a wall thickness $w = a_0 - D$ between 0.7 and 0.8 nm, i.e., typical values for MCM-41 materials [18, 20].

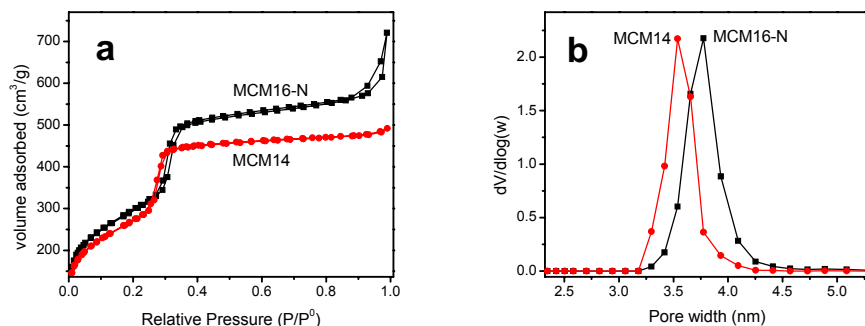


Figure 2. Characterization of MCM14 and MCM16-N silica by nitrogen adsorption: (a) Adsorption–desorption isotherms; (b) pore size distribution based on NLDFT analysis of the adsorption data.

Table 1: Characterization of the two MCM-41 materials by nitrogen adsorption and XRD.^a

Sample	$v_p / \text{cm}^3 \text{g}^{-1}$	$a_s / \text{m}^2 \text{g}^{-1}$	$D_{\text{DFT}} / \text{nm}$	$D_{\text{KJS}} / \text{nm}$	a_0 / nm
MCM16-N	0.96	1070	3.77 ± 0.1	3.67 ± 0.1	4.47 ± 0.05
MCM14	0.76	970	3.54 ± 0.1	3.45 ± 0.1	4.24 ± 0.05

^a v_p , specific pore volume; a_s , specific surface area; D_{DFT} and D_{KJS} , pore diameter derived by the NLDFT method [18] and the KJS method [19]; a_0 , lattice parameter of the pore lattice.

4.2.2 Lysozyme adsorption

The uptake of lysozyme in MCM14 silica was studied at pH 7 and pH 2 in 50 mM phosphate buffer. In the adsorption measurements, solutions of 1 to 5 mg/mL lysozyme were contacted with a fixed amount of silica (6 mg/mL) and equilibrated for 48 h at 25 °C by means of a multiple axel rotor. After centrifugation the supernatant was analyzed by UV/Vis spectroscopy, and the adsorbed amount was determined from the change in absorbance at 278 nm (see Figure 3). For MCM14 silica at

4 Lysozyme as a pH-responsive valve for controlled release of guest molecules from mesoporous silica

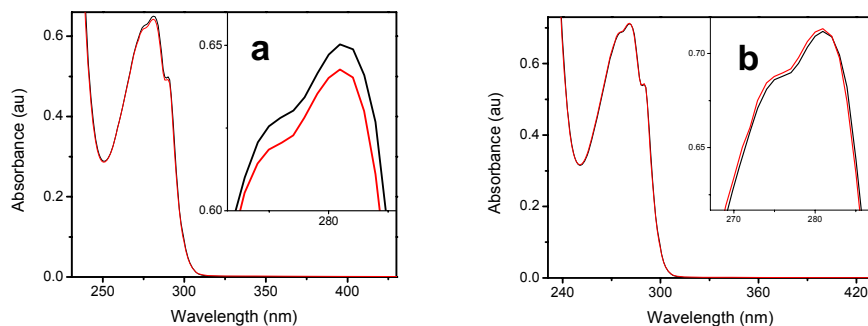


Figure 3. Adsorption of lysozyme determined from the UV absorbance of the buffered solution before (black curve) and 24 h after adding the silica (red curve): (a) pH 7, (b) pH 2.

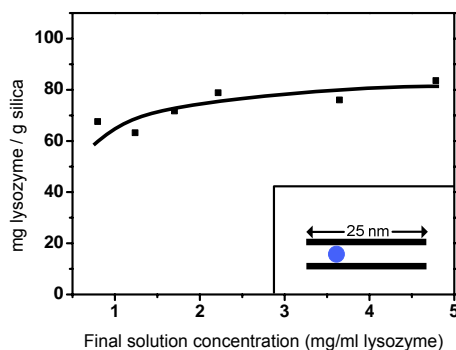


Figure 4. Adsorption isotherm of lysozyme in MCM14 at pH 7. The curve is drawn as a guide to the eye. The inset illustrates the low adsorption level of the protein in MCM14.

pH 7, a protein uptake up to 80 mg/g silica was found after 48 h, as shown in Figure 4. This low uptake, which corresponds to one protein molecule per about 25 nm along the pore channels, is attributed to transport limitation of the protein in the pores in the regime close to size exclusion of the protein. To test this supposition, the distribution of the protein in the particles after 24 h contact with the solution at pH 7 was visualized by CLSM, using Atto 647N labeled lysozyme. Representative CSLM images, shown in Figure 5, indicate that the protein is not evenly distributed within the particles but present only in their outer region. This finding may be affected by the protein label, as it is known that Atto 647N labeled molecules may strongly stick to glass surfaces [21], but this cannot be the main cause for the observed behavior. Hence we conclude

that at pH 7 the lysozyme molecules can enter the pores of MCM14 but remain mostly near the pore entrances of the particles, where the concentration is then significantly higher than the average concentration as determined by the adsorption measurements. A similar behavior was found for the larger protein BSA in SBA-15 with pores of nearly 13 nm diameter [22].

Unlike at pH 7, almost no uptake of lysozyme in MCM14 silica is detectable at pH 2, as shown in Figure 3b by the negligible change in absorbance of the supernatant at pH 2. This finding is in line with adsorption studies of lysozyme at nonporous silica and can be attributed to the absence of an electrostatic driving force for adsorption near the IEP of silica [15]. Interestingly, however, we find that lysozyme that was adsorbed in the pores of MCM14 at pH 7 is not desorbed when the pH of the sample is changed to pH 2. This is indicated by the CLSM image in Figure 5d.

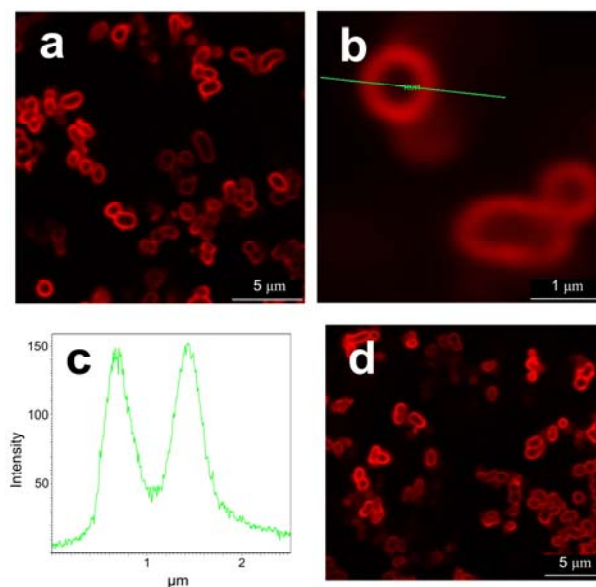


Figure 5. Confocal laser scanning microscopy images: (a) Atto647N-labeled lysozyme adsorption in MCM14 in pH 7 buffer; (b) magnification of a silica particle loaded with labeled lysozyme at pH 7; (c) fluorescence intensity profile of the particle; (d) fluorescence image showing that labeled lysozyme adsorbed at pH 7 is not desorbed after changing to pH 2.

4.2.3 pH-responsive pore blocking and unlocking

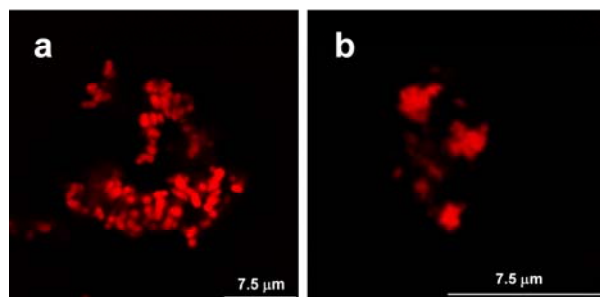


Figure 6. Confocal laser scanning microscopy images prove the uptake of rhodamine b in the pores capped with lysozyme: (a) MCM14; (b) MCM16-N

The effectiveness of the lysozyme@MCM-41 adduct as a pH-responsive valve to block and unlock the pores of the mesoporous silica was tested using rhodamine B as a model drug. Samples for these tests were prepared as explained in Section 2.5, and loading with rhodamine B was confirmed by CLSM, as shown in Figure 6. The dye release behavior from MCM16-N samples with and without lysozyme caps is shown in Figure 7a, where the concentration of released dye is plotted as a function of time. It can be seen that the dye is quickly released from the reference sample containing no lysozyme (Figure 7a, curve 1), but effective capping is observed for the same material in the presence of lysozyme, as indicated by the nearly constant lower absorbance of the sample at pH 2 prior to base activation (Figure 7a, curve 2). The initial increase in absorbance in curve 2 indicates that not all pores of MCM16-N have been capped effectively. Leakage may occur from pores with diameters larger than the mean diameter ($D = 3.7$ nm) which are not blocked by lysozyme molecules. This explanation is supported by the results for sample MCM14 ($D = 3.5$ nm), shown in Figure 7b, which indicate that initial leakage of dye from this material at pH 2 was much reduced in comparison with the 3.7 nm material. Hence it appears that a subtle change in pore diameter of about 0.2 nm (cf. Table 1) significantly affects the capping efficiency of lysozyme at pH 2. On the other hand, fast release of the dye takes place from both silica materials when switching from pH 2 to pH 7, as indicated by vertical arrows in Figure 7.

4.3 Discussion and conclusion

The results presented in Figure 7 show that lysozyme@MCM-41 can act as a pH-responsive valve for controlled drug release. A possible working scheme of this carrier system is sketched in Figure 8. After loading of the silica carrier with the drug, lysozyme is added and adsorbed near the pore entrances at pH 7. When changing pH to the strongly acidic regime (pH 2) the lysozyme molecules undergo a conformational change by which they get jammed in the pores and prevent dye molecules from leaving the pores. On returning to neutral pH, lysozyme molecules return to their original conformation and open a pathway for the release of dye molecules.

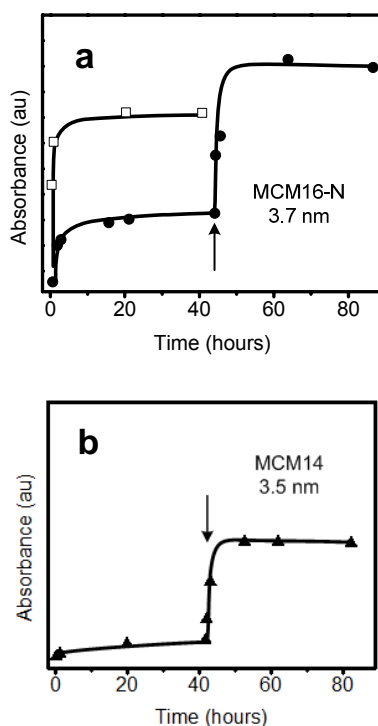


Figure 7. Release characteristics of rhodamine B in MCM-41 materials capped with lysozyme, showing the absorbance intensity of released rhodamine B as a function of time. The vertical arrows mark the moment at which pH is changed from pH 2 to 7: (a) MCM16-N without cap (1) and with lysozyme caps (2); (b) MCM14 with lysozyme caps. Curves are drawn to guide the eye.

The nature of the pH-induced conformational change of lysozyme that is causing the pore blocking is not clear. The reported increase of the

hydrodynamic radius of lysozyme at low pH [11] suggests some expansion of the molecules, caused by internal repulsive charge interactions at the high net charge of the protein at pH 2. Such an expansion may cause jamming of lysozyme in the pores at this low pH. Pronounced pH-reversible conformational changes have been reported for other globular proteins such as cytochrome c [12] and serum albumin [13]. A pH-induced expansion of the protein may also explain the very pronounced influence of pore size on the pore blocking ability of lysozyme (cf. Figure 7a and b). However, experimental evidence for a pH-induced expansion of lysozyme molecules in solution is not as clear as for cytochrome c. Measurements of the hydrodynamic radius of lysozyme by DLS performed in our laboratory gave a value $R_h = 1.85 \pm 0.05$ nm for the pH range from 7 to 2, without any trend to higher values at lower pH. It seems likely, therefore, that a pH induced conformational change of lysozyme molecules is caused by its interaction with the pore walls. It is desirable to test this conjecture by coarse-grained molecular simulation such as in ref. 8.

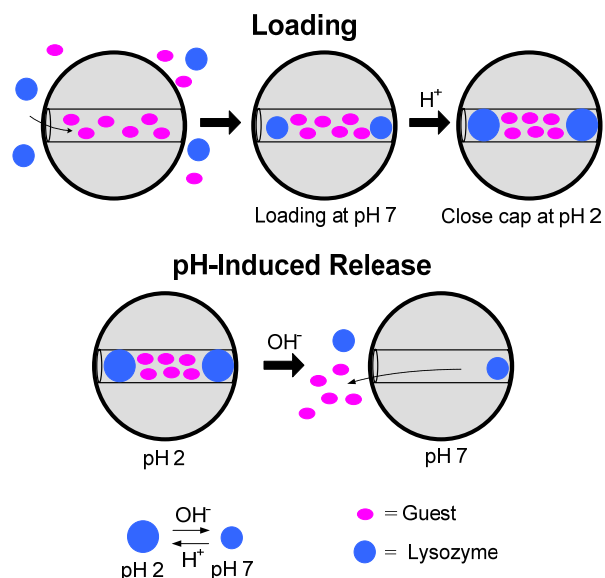


Figure 8. Schematic illustration of a pH responsive nanogated carrier system based on mesoporous silica capped by lysozyme. pH responsiveness is based on the expansion of the protein molecules as their net charge increases with decreasing pH.

The experiments recorded in Figure 7 show that fast release of the dye from the silica carrier can be triggered by returning from pH 2 to pH 7. This indicates

that the lysozyme nanovalves unlock the pores at neutral pH. As the lysozyme molecules shrink to their original size at pH 7, the free space between protein and the pore walls will allow water molecules to move in and out the pores, but the free space may not allow the dye molecules to pass by the protein. To explain the observed fast release of the dye we propose an osmotic driving force, resulting from water moving into the pores due to the high concentration of dye in the pore space. The resulting osmotic pressure may then cause the protein to be pushed out of the pores. Once the pores are free, part of the dye can diffuse out to equilibrate with the water phase outside. This model offers a plausible explanation for the quick release of the dye after activation the pH release trigger, and may also explain the initial release at pH 2 from wider pores (MCM16-N) in which the expanded protein molecules are not firmly jammed.

In the literature a similar mesoporous silica based carrier system using nano-sized particles jammed in the cylindrical pores as a valve for controlled drug release was reported by Lin and coworkers [3a]. In that work, size-defined CdS nanocrystals were used to close organically functionalized pores via chemical linkage in the pore mouth. Opening of the pores was then achieved by a chemical release trigger by which the disulfide bridges between the pore mouth and cap were destroyed [3a]. Using protein molecules to cap the pores in the silica matrix has advantages against inorganic particles, mostly because of the intrinsic ability of soft matter to adapt to pH without the need of chemical linkers between the cap and the pore walls. However, the nature of the pH-induced conformational changes of lysozyme confined in the pore channels is not yet understood, and further research is needed to elucidate the mechanisms involved.

In summary, we have shown that proteins can be used as pH-sensitive valves for the delivery of drug from mesoporous silica. The operation of this valve is based on the physical adsorption of lysozyme in the pores of native porous silica and a pH-induced change in conformation of the protein in the pore space. An advantage of this system lies in the use of therapeutic biomolecules and native porous silica. Thus, the creation of toxic species can be avoided. Another advantage of our capping method is that drug molecules can be easily

encapsulated inside the porous silica without surface functionalization. This means that the mesoporous silica carrier and the lysozyme caps do not need to be derivatized to have chemically reactive groups to be attached to the surface through covalent bonds. The drug delivery system is promising for in vivo controlled-release biomedical applications. This proof of concept might provide a general route for the use of other proteins based on the conformational changes as capping agents in the field of controlled delivery nanodevices.

References of chapter 4

- [1] (a) Allen, T. M.; Cullis, P. R. *Science* 2004, 303, 1818-1822. (b) Qiu, Y.; Park, K. *Adv. Drug Deliv. Rev.* 2001, 53, 321-339. (c) Giri, S.; Trewyn, B. G.; Lin, V. S.-Y. *Nanomedicine* 2007, 2, 99-111.
- [2] (a) Vallet-Regí, M.; Balas, F.; Arcos, D. *Angew. Chem. Int. Ed.* 2007, 46, 7548-7558. (b) Trewyn, B. G.; Slowing, I. I.; Giri, S.; Chen, H.; Lin, V. S.-Y. *Acc. Chem. Res.* 2007, 40, 846-853. (c) Akcakayiran, D.; Mauder, D.; Hess, C.; Sievers, T. K.; Kurth, D. G.; Shenderovich, I.; Limbach, H.-H.; Findenegg, G. H. *J. Phys. Chem. B* 2008, 112, 14637-14647.
- [3] (a) Lai, C.-Y.; Trewyn, B. G.; Jeftinija, D. M.; Jeftinija, K.; Xu, S.; Jeftinija, S.; Lin, V. S. Y. *J. Am. Chem. Soc.* 2003, 125, 4451-4459. (b) Liu, R.; Zhang, Y.; Zhao, X.; Agarwal, A.; Mueller, L. J.; Feng, P. *J. Am. Chem. Soc.* 2010, 132, 1500-1501. (c) Vivero-Escoto, J. L.; Slowing, I. I.; Wu, C.; Lin, V. S.-Y. *J. Am. Chem. Soc.* 2009, 131, 3462-3463. (d) Zhu, C.; Lu, C.; Song, X.; Yang, H.; Wang, X. *J. Am. Chem. Soc.* 2011, 133, 1278-1281.
- [4] (a) Mal, N. K.; Fujiwara, M.; Tanaka, Y. *Nature* 2003, 421, 350. (b) Bernardos, A.; Aznar, E.; Marcos, M. D.; Martínez-Mañez, R.; Sancenón, F.; Soto, J.; Barat, J. M.; Amorós, P. *Angew. Chem. Int. Ed.* 2009, 48, 5884-5887.
- [5] (a) Zhao, Y.; Li, Z.; Kabehie, S.; Botros, Y. Y.; Stoddart, J. F.; Zink, J. I. *J. Am. Chem. Soc.* 2010, 132, 13016-13025. (b) Nguyen, T. D.; Tseng,

- H. R.; Celestre, P. C.; Flood, A. H.; Liu, Y.; Stoddart, J. F.; Zink, J. I. *Proc. Natl. Acad. Sci. USA* 2005, 102, 10029-10034.
- [6] (a) Yang, Q.; Wang, S.; Fan, P.; Wang, L.; Di, Y.; Lin, K.; Xiao, F. *Chem. Mater.* 2005, 17, 5999-6003. (b) Liu, R.; Liao, P.; Liu, J.; Feng, P. *Langmuir*, 2011, 27, 3095-3099. (c) Liu, R.; Zhao, X.; Wu, T.; Feng, P. *J. Am. Chem. Soc.* 2008, 130, 14418-14419. (d) Singh, N.; Karambelkar, A.; Gu, L.; Lin, K.; Miller, J. S.; Chen, C. S.; Sailor, M. J.; Bhatia, S. N. *J. Am. Chem. Soc.* 2011, 133, 19582-19585. (e) Radu, D. R.; Lai, C.-Y.; Jeftinija, K.; Rowe, E. W.; Jeftinija, S.; Lin, V. S. Y. *J. Am. Chem. Soc.* 2004, 126, 13216-13217.
- [7] (a) Schlossbauer, A.; Kecht, J.; Bein, T. *Angew. Chem. Int. Ed.* 2009, 48, 3092-3095. (b) Climent, E.; Bernardos, A.; Martínez-Mañez, R.; Maquiera, A.; Marcos, M. D.; Pastor-Navarro, N.; Puchades, R.; Sancenón, F.; Soto, J.; Amorós, P. *J. Am. Chem. Soc.* 2009, 131, 14075-14080. (c) Zhao, Y.; Trewyn, B. G.; Slowing, I. I.; Lin, V. S.-Y. *J. Am. Chem. Soc.* 2009, 131, 8398-8400. (d) Luo, Z.; Cai, K.; Hu, Y.; Zhao, L.; Liu, P.; Duan, L.; Yang, W. *Angew. Chem. Int. Ed.* 2011, 50, 640-643. (e) Coll, C.; Mondragón, L.; Martínez-Mañez, R.; Sancenón, F.; Marcos, M. D.; Soto, J.; Amorós, P.; Pérez-Payá, E. *Angew. Chem. Int. Ed.* 2011, 50, 2138-2140.
- [8] Kubiak, K.; Mulheran, P. A. *J. Phys. Chem. B* 2009, 113, 12189-12200.
- [9] Posse, E.; Vitals, A. L.; de Arcuri, B. F.; Farias, R. N.; Morero, R. D. *Biochim. Biophys. Acta* 1990, 1024, 390.
- [10] Parmar, A.S.; Muschol, M. Hydration and Hydrodynamic Interactions of Lysozyme: Effect of Chaotropic versus Kosmotropic Ions, *Biophys. J.* 2009, 97, 590-598.
- [11] Bonincontro, A.; Francesco, A. D.; Onori, G. *Colloids Surf. B* 1998, 12, 1-5.
- [12] (a) Cinelli, S.; Spinozzi, F.; Itri, R.; Finet, S.; Carsughi, F.; Onori, G.; Mariani, P. *Biophys. J.* 2001, 81, 3522-3533; (b) Werner, J. A.; Joggerst, R.; Dylar, R. B.; Goodwin, P. M. *Proc. Natl. Acad. Sci. USA* 2006, 103, 11130-11135.

- [13] Tsai, D.-H.; DelRio, F.W.; Keene, A.M.; Tyner, K.M.; MacCuspie, R.I.; Cho, T.J.; Zachariah, M.R.; Hackley, V.A. *Langmuir* 2011, 27, 2464-2477.
- [14] Iler, R. K., *The Chemistry of Silica*, Wiley-VCH, New York, Weinheim, 1979
- [15] (a) van der Veen, M.; Norde, W.; Cohen-Stuart, M. *Colloids Surf B* 2004, 35, 33-40; (b) Bharti, B.; Meissner, J.; Findenegg, G. H. *Langmuir* 2011, 27, 9823-9833.
- [16] (a) Vinu, A.; Murugesan, V.; Hartmann, M. *J. Phys. Chem. B* 2004, 108, 7323-7330. (b) Katiyar, A.; Ji, L.; Smirniotis, P. G.; Pinto, N. G. *Micropor. Mesopor. Mater.* 2005, 80, 311-320. (c) Sezões, F.; Ribeiro Carrott, M. M. L.; Mourão, P. A. M.; Russo, P. A.; Carrott, P. J. M. *Mater. Sci. Forum*, 2010, 636-637, 54-59.
- [17] Jähnert, S.; Vaca Chávez, F.; Schaumann, G. E.; Schreiber, A.; Schönhoff, M.; Findenegg, G. H. *Phys. Chem. Chem. Phys.* 2008, 10, 6039-6051.
- [18] Ravikovitch, P. I.; Wei, D.; Chueh, W. T.; Haller, G. L.; Neimark, A. V. *J. Phys. Chem. B* 1997, 101, 3671-3679.
- [19] (a) Kruk, M.; Jaroniec, M.; Sayari, A., *Chem. Mater.* 1999, 11, 492-500; (b) Jaroniec, M.; Solovyov, L. A., *Langmuir* 2006, 22, 6757-6760.
- [20] Shenderovich, I. G.; Mauder, D.; Akcakayiran, D.; Buntkowsky, G.; Limbach, H.-H.; Findenegg, G. H. *J. Phys. Chem. B* 2007, 111, 12088-12096.
- [21] Kolmakov, K.; Belov, V. N.; Bierwagen, J.; Ringemann, C.; Müller, V.; Eggeling, C.; Hell, S. W. *Chem. Eur. J.* 2010, 16, 158-166.
- [22] Katiyar, A.; Pinto, N. G. *Small* 2006, 2, 644-648.

5 Energy transfer between dye molecules in MCM-41 studied by fluorescence lifetime imaging*

5.1 Introduction

Sunlight is absorbed by the light-harvesting antenna system in the leaves of living plants, where it is transferred by specifically arranged chlorophyll molecules for the photo-energy conversion [1a,b]. A variety of artificial light-harvesting antenna materials has been developed in recent years for use in light-emitting device, solar cell [1b]. The construction of such antenna systems has proven to be difficult because of the limited degree of organization of organic dye molecules. Dye molecules have a tendency to form aggregates which are known to cause fast thermal relaxation of electronic excitation energy. Localization of the dye molecules in nanopores of zeolites has opened up new possibilities for the use of nanoporous materials for light harvesting applications [2, 3]. The nanoscale spaces in zeolites are expected to play a major role in preventing aggregation and organizing the adsorbed dye molecules to desirable structures inside the pores. Ordered mesoporous silica materials such as MCM-41 and SBA-15, which constitute arrays of cylindrical channels of uniform size arranged side by side in a 2d-hexagonal packing, have been extensively studied because of their well-defined mesoscale structure [4-7]. Effective transfer of excitation energy between coumarin 485 and pyrromethene 567 dyes adsorbed in mesoporous silica thin films has been reported [4]. The effect of pore size and pore structure on the energy transfer between dye molecules has been studied for a series of mesoporous hosts (MCM-41, SBA-15, MCM-48). It has been found that at low dye concentrations dye molecules confined in nanosized cavities show enhanced resonance energy transfer efficiency [5]. Fluorescence lifetime imaging microscopy (FLIM) allows mapping of fluorescence lifetimes with nanosecond time resolution and diffraction-limited spatial resolution of approximately 200 nm [8]. Accordingly, energy transfer phenomena measured by FLIM can provide temporal and spatial information. Observing and

* modified from the manuscript Energy transfer between dye molecules in MCM-41 studied by fluorescence lifetime imaging, Mengjun Xue, Gerhard H. Findenegg. To be submitted.

understanding of energy transfer processes in unidirectional channel systems is of considerable interest in the context of artificial light-harvesting antenna materials.

FRET involves the non-radiative transfer of energy from an excited molecule (donor) to a different molecule (acceptor) in its vicinity. Since the efficiency of resonance energy transfer is proportional to the inverse sixth power of the distance from donor to acceptor, measurement of FRET efficiency can be used to determine the distance between the two dye molecules on a nanometer length scale. Techniques to detect FRET in the context of microscopy are usually based on the fluorescence intensity of either the donor or the acceptor. Alternatively, FRET may be determined from the fluorescence lifetime. Since donor fluorescence and energy transfer to the acceptor are competing processes the time the donor molecule stays in the excited state will be decreased by FRET. The determination of FRET efficiency based on fluorescence lifetime measurements using FLIM avoids some of the drawbacks of fluorescence-intensity-based techniques. The specific aim of the present work has been to study the distribution of dye molecules in the MCM-41 matrix. We use a common FRET pair, fluorescein (donor) and rhodamine b (acceptor) and vary the concentration of the acceptor over two decades at constant donor concentration. From the FRET efficiencies we can determine the mean distance between donor and acceptor as a function of the acceptor concentration in the matrix and thus assess the distribution of the two dyes in the porous matrix. As a longer-term goal we plan to adopt this method for studying the distribution of proteins and other biomolecules in the channels of MCM-41 or SBA-15 by using biomolecules labeled with either the donor or acceptor of a FRET pair.

5.2 Results

5.2.1 Characterization of MCM-41

The MCM-41 powder used in this work was synthesized according to our earlier work [9] using hexadecyltrimethylammonium bromide ($C_{16}TAB$) as the structure-directing amphiphilic species. The properties of the sample were checked by nitrogen adsorption and small-angle X-ray scattering (SAXS).

Figure 1 shows the nitrogen adsorption/desorption isotherm and SAXS profile of the MCM-41 material used in this work. From nitrogen adsorption a specific surface area (BET method) $a_{\text{BET}} = 930 \text{ m}^2/\text{g}$ and specific pore volume $v_p = 0.86 \text{ cm}^3/\text{g}$ was derived. The mean pore diameter D was derived from the pore condensation pressure $(p/p_0)_{\text{pc}} = 0.369$ by the method proposed by Kruk et al [10]. A value $D_{\text{KJS}} = 4.0 \text{ nm}$ was obtained. SAXS scans of the MCM-41 sample (Fig. 1b) exhibit the leading Bragg reflections of a 2D-hexagonal lattice. From the position of the (10) peak, $q_{10} = 1.498 \text{ nm}^{-1}$, we derive a pore center-to-center distance $a_0 = 4.8 \text{ nm}$ and a wall thickness $w = a_0 - D = 0.8 \text{ nm}$.

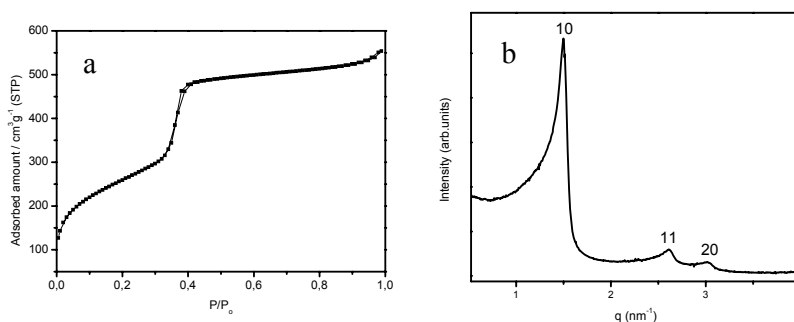


Figure 1. Characterization of the MCM-41 sample: (a) Nitrogen adsorption/desorption isotherms; (b) Small-angle XRD.

5.2.2 MCM-41 particles doped with fluorescein and rhodamine b

A set of samples of nearly equal concentration of the donor (fluorescein) but different concentrations of the acceptor (rhodamine b) was studied in this work. Samples were prepared by contacting a mass m_s of MCM-41 ($m_s = 2 \text{ mg}$) with a fixed volume ($V = 1 \text{ mL}$) of a phosphate buffered solution (pH 7) of fluorescein of initial concentration $c_D^0 = 1.25 \text{ } \mu\text{M}$ (donor-only sample), and solutions with $c_D^0 = 1.25 \text{ } \mu\text{M}$ plus $c_A^0 = 1.25 \cdot f \text{ } \mu\text{M}$ of rhodamine b, with $f = 0.1, 0.5, 1, 2,$ and 10 (donor-plus-acceptor samples). After equilibration (2 d) the silica was removed from the supernatant by centrifugation and washed with buffer solution to remove dye molecules attached to the outer surface of the silica particles. The uptake of the two dyes in MCM-41 was determined by measuring the concentrations of donor and acceptor in the supernatant (c_D^e and c_A^e),

respectively) using UV spectroscopy. The specific uptake was calculated as

$$n_k = \frac{(c_k^o - c_k^e)V}{m_s}, \text{ where } k = \text{D, A.}$$

Table 1. MCM-41 samples doped with donor and acceptor.

Sample	$n_D/\mu\text{mol/g}$	$n_A/\mu\text{mol/g}$	x_A	D:A
a	0.290	0.059	0.17	1:0.2
b	0.265	0.295	0.52	1:1.1
c	0.292	0.611	0.68	1:2.1
d	0.290	1.255	0.81	1:4.3
e	0.176	5.9	0.97	1:34

It was found that the acceptor dye was preferentially adsorbed in the silica matrix. This is plausible because the cationic rhodamine b will interact more favorably with the silica surface than the zwitterionic fluorescein at pH 7. The specific amounts of donor and acceptor in the five samples (a – e) studied in this work are given in Table 1. Note that the amount of donor is similar in most of the samples but the overall amount of dye is strongly increasing from a to e. The composition of the dye mixture in the matrix is expressed by the acceptor mole

fraction $x_A = \frac{n_A}{n_D + n_A}$ and the donor-to acceptor molar ratio D:A. Below we

refer to these samples by approximate values of the molar ratio, viz., 1:0.2 (a), 1:1 (b), 1:2 (c), 1:4 (d), 1:34 (e).

5.2.3 Fluorescence lifetime analysis

Fluorescence lifetime imaging microscopy (FLIM) was performed using a Leica TCS SP5 II confocal microscope system. Fluorescence lifetime was measured using a time-correlated single photon counting (TCSPC) module in the time-tagged time-resolved (TTTR) mode. Fluorescence decay curves of the five samples containing donor and acceptor in different molar ratios (Table 1) and of an acceptor-only sample, all detected through the donor channel. Figure 2 shows the fluorescence decay curve of fluorophores fluorescein (D) and rhodamine b (A) in MCM-41. The fact that the decay of the acceptor-only sample can be detected by the detector channel indicates cross-talk between donor and

acceptor channels, which must be taken into account in the data analysis. The intensity decays $I(t)$ were analyzed in terms of a multi-exponential function, viz.,

$$I(t) = \sum_{i=1}^n \alpha_i e^{-\frac{t}{\tau_i}} \quad (1)$$

where α_i is the amplitude and τ_i the lifetime of the lifetime component indicated by index i . Values of the parameters α_i and τ_i were obtained through nonlinear least-squares fitting, using the SymPhoTime v. 4.3 software (PicoQuant) [11]. The goodness-of-fit was assessed from the value of the reduced χ^2 parameter, which in all cases was close to 1, indicating a good fit. The fractional contribution of lifetime component τ_i is defined by the amplitudes of the n contributions as

$$A_i = \frac{\alpha_i}{\sum_i \alpha_i} \quad (2)$$

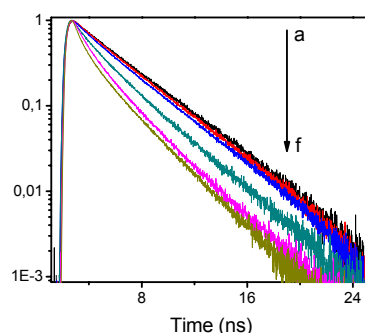


Figure 2. Fluorescence decay of fluorophores fluorescein (D) and rhodamine b (A) in MCM-41 as measured by detector 1 for different donor:acceptor molar ratios (D:A): (a) 1:0; (b) 1:1.1; (c) 1:2; (d) 1:4; (e) 1:34; (f) 0:1. The decays have been normalized to allow direct comparison.

FLIM images of MCM-41 particles doped with fluorescein as the donor (D) and rhodamine b as the acceptor (A) were analyzed with the aim to determine the FRET efficiency of the donor-acceptor pair in the MCM-41 matrix at different molar ratios D:A. As a representative example, FLIM images for the molar ratio D:A = 1:1 are presented in Figure 3. Fluorescence intensity images of a MCM-41 particle in the donor channel and the acceptor channel are shown in Figure 3a and Figure 3b, respectively, together with the brightness of the pixel codes for the number of detected photons. The region of the silica particle was selected as

the region of interest (ROI) for further analysis. The donor channel displays fluorescence emission of the donor but also some emission from the acceptor, due to crosstalk. The acceptor channel displays fluorescence emission of the acceptor caused by Förster energy transfer from the donor and by direct excitation. The fluorescence lifetime map of the donor channel is presented in Figure 3c, together with the pixel code for the relevant range of lifetimes. In most cases the lifetime map indicated a homogeneous distribution of lifetimes over the entire MCM-41 particle. The fluorescence signals of all pixels within ROI were linked in the procedure to analyze the fluorescence decays. This overall intensity decay in the donor channel is shown in Figure 3d, together with the residuals of the fit by a two-exponential decay function (see below). For each donor-to-acceptor molar ratio, as well as for the donor-only sample, images of several MCM-41 particles were recorded and analyzed in order to assess the statistical errors of the method.

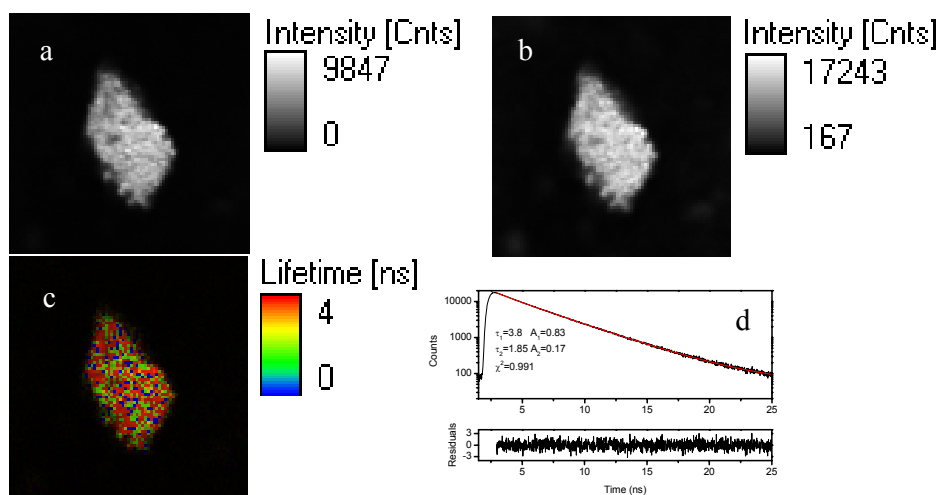


Figure 3. FLIM-FRET measurements of the sample with D:A at molar ratio of 1:1.1. (a) Intensity image in channel 1; (b) intensity image in channel 2 (acceptor channel); (c) lifetime image (channel 1); (d) intensity decay of the pixels in the MCM-41 particle and fit by the two-exponential model, together with the residuals (bottom panel). Data collection time 15 min. The scale of diagrams (a)-(c) is $30 \mu\text{m} \times 30 \mu\text{m}$, the resolution is 512×512 pixels.

The fluorescence decay of the donor-only samples could be represented by a decay function with mean lifetime $\tau_D = 3.80$ ns. For silica particles containing

donor and acceptor the fluorescence decays were analyzed with the two-exponential or the three-exponential model. In all cases τ_1 was kept constant and equal to τ_D . For the two lowest acceptor concentrations (D:A up to 1:1) the two-exponential model with three adjustable parameters (τ_2 , α_1 and α_2) was found to give excellent fits with $\chi^2 < 1$ and without systematic structure in the residual plots, as shown in Figure 4 (a and b). For the sample with a donor-to acceptor molar ratio D:A = 1:2 the two-exponential function also gives a good fit, but in this case a marginally better fit was obtained with a three-exponential function with fixed values $\tau_1 = 3.80$ ns and $\tau_2 = 2.40$ ns and four adjustable parameters (τ_2 , α_1 , α_2 and α_3), as shown in Fig 4. The value of τ_2 used in this fit is equal to the mean lifetime of the acceptor in an acceptor-only sample. For the two samples of highest acceptor concentrations (D:A = 1:4 and 1:34) only the three-exponential model gives a good representation of the decay curves while in the fits with the two-exponential model systematic deviations appear in the residuals (Figure 4).

Table 2 summarizes the lifetime components τ_i and their fractional contributions A_i (eq. 2) as obtained by the fit procedure for the five samples of different donor-to-acceptor ratios. The error bars for τ_3 and A_3 indicate the spread of the respective values as determined for different MCM-41 particles of the same sample. The component with lifetime τ_2 represents the contribution of the acceptor to the fluorescence decay in the donor channel. From its fractional contribution A_2 it can be seen that this contribution is negligibly small in the samples of low acceptor concentration but reaches 50% at the highest acceptor concentrations. This contribution must be subtracted in the further analysis of the lifetime data. The component with lifetime τ_1 , which appears in all samples, is equal to the intrinsic fluorescence lifetime of the donor (τ_D). The fractional contribution of this component decreases from 90% at the lowest acceptor concentration to about 10% at the highest acceptor concentration. The shorter-lifetime component τ_3 which appears in the presence of the acceptor is attributed to donor molecules quenched by FRET. The fractional contribution of this component increases from less than 10% to ca. 40% over the range of donor-to-acceptor molar ratios studied.

5 Energy transfer between dye molecules in MCM-41 studied by fluorescence lifetime imaging

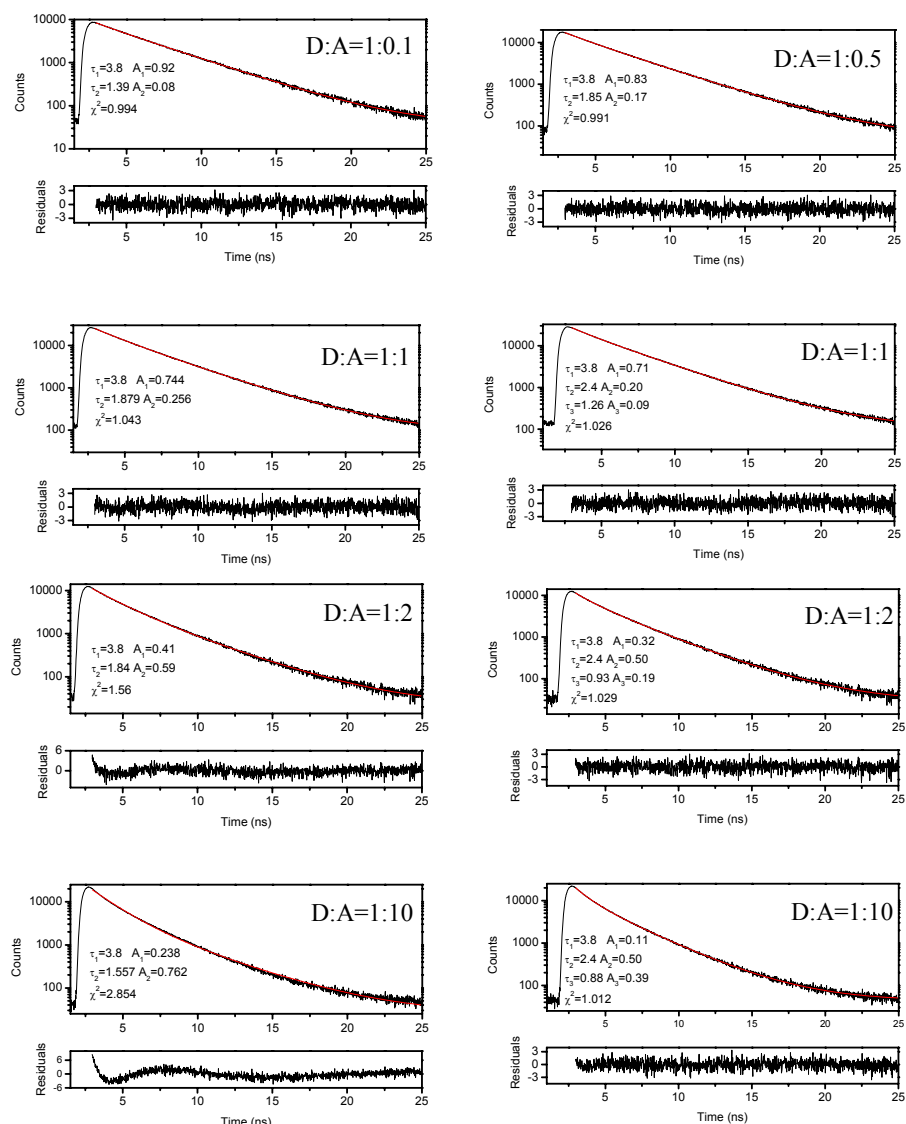


Figure 4. Comparison of the fits of the TCSPC data in the MCM-41 particles.

Table 2. Analysis of the TCSPC data for the FRET pair fluorescein (D) and rhodamine b (A) at different donor to acceptor molar ratio D:A in the MCM-41 matrix. Lifetimes τ_i (in ns) and relative contribution A_i of the lifetime component.

D:A	τ_1 / ns	τ_2 / ns	τ_3 / ns	A_1	A_2	A_3	χ^2
1:0	3.8						
1:0.2	3.8		1.39	0.92		0.08	0.994
1:1.1	3.8		1.85	0.83		0.17	0.991
	3.8	2.4	1.72	0.82	0.05	0.13	0.989
1:2.1	3.8	2.4	1.26	0.71	0.20	0.09	1.026
1:4.3	3.8	2.4	0.93	0.32	0.50	0.19	1.029
1:3.4	3.8	2.4	0.88	0.11	0.50	0.39	1.012

5.2.4 FRET efficiency

The FRET efficiency is defined as the fraction of photons that is transferred from the donor to the acceptor by the resonance process. If donor and acceptor

of a FRET pair have a fixed distance from each other the energy transfer will cause a decrease of the donor life time from the value in the absence of the acceptor (τ_D) to a value τ_{DA} and the transfer efficiency is given by [12]

$$E = 1 - \frac{\tau_{DA}}{\tau_D} \quad (3)$$

In the present case we have no fixed D-A pairs but expect a distribution of donor-to-acceptor distances in the sample. Accordingly, we do not observe a single-exponential decay of the donor in the presence of the acceptor. Instead the donor decay can be represented by a two-exponential function with lifetimes τ_1 and τ_3 . In this case the FRET efficiency is calculated using the amplitude-weighted average lifetime $\langle \tau \rangle = \sum_i A_i \tau_i$ instead of τ_{DA} , but taking into account the lifetime components of the donor only. Hence we replace τ_{DA} of eq. 3 by $\langle \tau \rangle = (A_1 \tau_1 + A_3 \tau_3) / (A_1 + A_3)$, where we normalize the amplitudes of the donor components. Values of the average lifetime and of the transfer efficiency E calculated in this way are given in Table 3.

Table 3. FRET analysis of TCSPC donor lifetime at different D:A molar ratios in the MCM-41 matrix. FRET efficiency E (eq 3) and donor to acceptor distance r_{DA} (eq 4).

D:A	τ_D / ns	τ_{DAv} / ns	E	r_{DAv} / nm
1:0.2	3.8	3.61	0.051	8.96
1:1.1	3.8	3.47	0.087	8.13
	3.8	3.52	0.08	8.36
1:2.1	3.8	3.51	0.08	8.36
1:4.3	3.8	2.73	0.28	6.43
1:34	3.8	1.52	0.6	5.14

From the FRET efficiency a mean distance r_{DA} between donor and acceptor molecules in the pore space was calculated by the Förster equation

$$r_{DA} = R_0 \left(\frac{1-E}{E} \right)^{\frac{1}{6}} \quad (4)$$

where R_0 is the Förster distance defined as the donor-to-acceptor distance at which the resonance energy transfer efficiency is 50%. For the fluorescein-rhodamine pair $R_0 = 5.5$ nm [13]. Resulting values of r_{DA} are also given in Table 3.

5.3 Discussion and conclusion

We have studied the distribution of donor and acceptor molecules of the FRET pair fluorescein – rhodamine b in the pore space of MCM-41 using FLIM. The main finding is that the mean distance of donor-acceptor pairs, r_{DA} , decreases from nearly 10 nm to about 5 nm as the acceptor concentration increases by more than a factor 100 at constant donor concentration in the matrix. This is shown in Figure 5, where r_{DA} is plotted as a function of the mole fraction of the acceptor, $x_A = N_A/(N_D+N_A)$. To assess the significance of this finding we can estimate the mean distance of donor-acceptor pairs from the amounts of donor and acceptor in the sample. When the N dye molecules are distributed uniformly over the entire volume V_s of the porous solid, the mean volume per molecule is $v_M = V_s/N$ and a mean next-neighbor distance is $d = \sqrt[3]{v_M}$. Furthermore, if donor and acceptor molecules in the pore volume are distributed as in a *random mixture* the mean distance of a donor-acceptor pair, d_{DA} , will be given by the mean next-neighbor distance d , independent of the relative concentrations of donor and acceptor molecules. It was estimated from the number of donor and acceptor molecules in the matrix (Table 1) and the volume of the solid, $V_s = m_s(v_p + 1/\rho_s)$, using the specific pore volume v_p and a silica density $\rho_s = 2.2 \text{ g/cm}^3$. Values of d are compared with the experimental values of r_{DA} in Figure 5. It can be seen that at low acceptor mole fraction x_A (i.e., low overall loadings) r_{DA} is smaller by a factor 2 than d . However, as x_A increases the estimated mean next-neighbor distance d decreases more strongly than r_{DA} and attains values similar to r_{DA} for $x_A \rightarrow 1$ (i.e., at the highest loading of the silica matrix).

The finding that at sufficiently high loadings the mean donor-to-acceptor distance r_{DA} derived from the FLIM-FRET analysis agrees with the value estimated from the number of molecules in of the matrix gives support to the data analysis presented here. Specifically, this concerns the method to eliminate the acceptor lifetime contribution τ_2 from the donor channel, as well as the choice of the amplitude-averaged mean value of the lifetimes τ_1 and τ_3 in the

calculation of the transfer efficiency E . The concordant values of r_{DA} and d in this regime also indicate that our method of sample preparation leads to a homogeneous distribution of the two dyes over the mesopore volume of the MCM-41 sample. Otherwise, if the adsorbed dye molecules were accumulating near the pore entrances, r_{DA} values significantly lower than d should be found. We note that at the highest loading studied in this work r_{DA} comes close to the pore center-to-center distance of MCM-41 ($a_0 = 4.8$ nm). At this and higher loadings one expects that the periodic structure of the mesopore lattice will start to play an important role by imposing correlations in the distribution function of the guest molecules in the matrix.

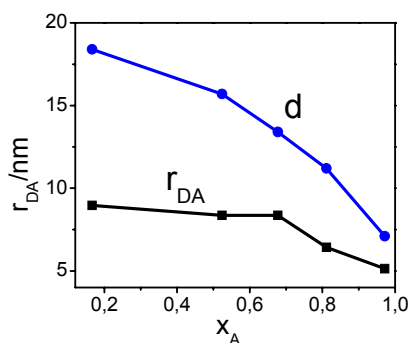


Figure 5. FRET efficiency and corresponding molecular distance r_{DA} curves.

At low mole fractions of the acceptor (low overall loadings of the matrix) the mean donor-to-acceptor distance r_{DA} derived from FRET is significantly smaller than the mean next-neighbor distance d (Figure 5). This finding can be rationalized by remembering that d represents the mean value of a distribution of next-neighbor distances, and that this distribution will become wider as the loading decreases. Since the FRET efficiency decreases with the inverse sixth power of the donor-to-acceptor distance, proximate D-A pairs will contribute mostly to the transfer efficiency. Accordingly, r_{DA} will deviate from the mean distance d the more the greater the width of the distribution function, i.e., the lower the loading of the sample. Indirect support for this conjecture comes from the lifetimes in Table 2, when we identify the components τ_1 and τ_3 as the lifetimes of unperturbed donor and donor undergoing FRET, respectively. Calculating the transfer efficiency by eq 3 with $\tau_{DA} = \tau_3$ (instead of $\tau_{DA} = \langle \tau \rangle$) we find donor-to acceptor distances r'_{DA} of 5.0 nm and 4.5 nm at the lowest and

highest loading of the sample. Whereas at the highest loading r'_{DA} is similar to $r_{DA} = 5.1$ nm, the value of r'_{DA} at the lowest loading is smaller by nearly a factor 2 than the value $r_{DA} = 9.0$ of Table 3. Hence the growing deviation of the measured mean donor-to-acceptor distances r_{DA} from the mean separation d displayed in Figure 5 indicates that the influence of proximate FRET pairs becomes the more important the smaller the concentration of dye molecules in the matrix.

In conclusion, this study has shown that important information about the distribution of donor and acceptor molecules in the pore space of mesoporous materials can be derived from fluorescence lifetime measurements by means of FLIM. Further work is needed to separate the effect of donor-to-acceptor molar ratio D:A from the overall concentration of dye molecules on the measured mean donor-to-acceptor distance r_{DA} .

References of chapter 5

- [1] (a) Yatskou, M. M.; Meyer, M.; Huber, S.; Pfenniger, M.; Calzaferri, G. *ChemPhysChem* 2003, 4, 567-587. (b) Calzaferri, G.; Huber, S.; Maas, H.; Minkowski, C. *Angew. Chem. Int. Ed.*, 2003, 42, 3732-3758.
- [2] Ruiz, A. Z.; Li, H.; Calzaferri, G. *Angew. Chem. Int. Ed.* 2006, 45, 5282-5287.
- [3] Inagaki, S.; Ohtani, O.; Goto, Y.; Okamoto, K.; Ikai, M.; Yamanaka, K.; Tani, T.; Okada, T. *Angew. Chem. Int. Ed.* 2009, 48, 4042-4046.
- [4] Scott, B. J.; Bartl, M. H.; Wirmsberger, G.; Stucky, G. D. *J. Phys. Chem. A* 2003, 107, 5499-5502.
- [5] Wang, L.; Liu, Y.; Chen, F.; Zhang, J.; Anpo, M. *J. Phys. Chem. C* 2007, 111, 5541-5548.
- [6] Itoh, T.; Yano, K.; Inada, Y.; Fukushima, Y. *J. Am. Chem. Soc.* 2002, 124, 13437-13441.
- [7] Itoh, T.; Yano, K.; Kajino, T.; Itoh, S.; Shibata, Y.; Mino, H.; Miyamoto, R.; Inada, Y.; Iwai, S.; Fukushima, Y. *J. Phys. Chem. B* 2004, 108, 13683-13687.

- [8] Wallrabe, H.; Periasamy, A. *Curr. Opin. Biotechnol.* 2005, 16, 19-27.
- [9] Jähnert, S.; Vaca Chávez, F.; Schaumann, G. E.; Schreiber, A.; Schönhoff, M.; Findenegg, G. H. *Phys. Chem. Chem. Phys.* 2008, 10, 6039-6051.
- [10] Kruk, M.; Jaroniec, M.; Sayari, A. *Langmuir* 1997, 13, 6267-6273.
- [11] http://www.picoquant.de/products/sw_mt/sw_mt.htm.
- [12] Lakowicz, J. R. *Principles of Fluorescence Spectroscopy*, 3rd Ed., Springer, New York, 2006.
- [13] Posokhova, Y. O.; Merzlyakova, M.; Hristovab, K.; Ladokhina, A. S. *Anal. Biochem.*, 2008, 380, 134-136.

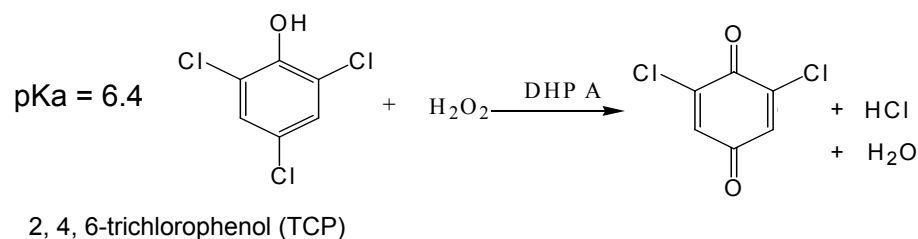
6 Intrinsic dynamics of DHP A underlies its enzymatic function

6.1 Introduction

Currently the main focus of understanding of enzyme function is determination of static 3-dimensional structure obtained from X-ray crystallography [1-2]. However, it is becoming increasingly well recognized that protein dynamics often play important roles in its function as well [1-9]. A detailed understanding of the intimate linkage between protein flexibility and its catalysis is a current challenge [1-2]. Dehaloperoxidase-hemoglobin (DHP A) is a monomer in solution [10] that has high structural homology with myoglobin [11-13]. The novelty of DHP is that it can oxidatively dehalogenate haloaromatics while maintaining oxygen storage function [14, 15]. In this chapter, we demonstrate that the intrinsic dynamics of DHP A is a key characteristic of catalysis. The dynamics of DHP A with substrate (2, 4, 6-trichlorophenol, TCP) were studied by NMR relaxation measurements.

6.2 Results and discussion

Figure 1 shows the activity of ^{15}N labeled DHP A with TCP. Complete conversion of TCP to 2, 6-DCQ is observed upon adding H_2O_2 over the course of the assay (Figure 1). The oxidation of TCP can be checked by the decrease in absorption at 313 nm and the gradually increase in absorption band of 2, 6-DCQ product at 272 nm.



Scheme: DHP A catalyzes the oxidative dehalogenation of trihalophenol to the dihalogenated quinone in the presence of H_2O_2 [16].

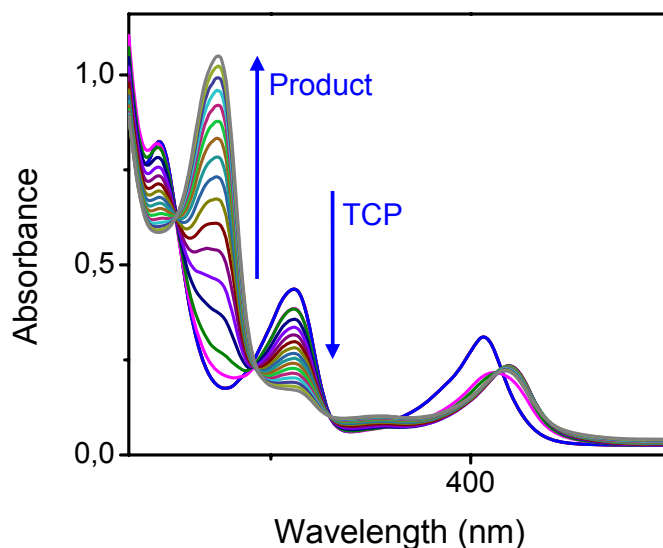


Figure 1. UV-vis enzymatic assay showing DHP A activity. The figure represent a 92 s assay going from 0 s (blue) to 92 s. The TCP molecule is completely converted to product 2, 6-DCQ in the presence of ^{15}N labeled DHP A.

6.2.1 Binding site of DHP A for TCP

Backbone amide chemical shift assignments were completed based on the previous work [16]. By analyzing the overlaid spectra for DHP A with and without TCP, the overall chemical shift change was calculated using $\Delta\delta = [(\Delta\delta_{\text{H}})^2 + (0.1\Delta\delta_{\text{N}})^2]^{1/2}$ [17], which reflects the total weighted change in ^1H and ^{15}N chemical shift for a given peak in the 2D ^1H - ^{15}N HSQC map. The potential binding site was identified by analyzing the overall chemical shift change $\Delta\delta$ of DHP A with TCP and without TCP, four residues, LEU62, MET63, ASP121, and ARG122 show an overall chemical shift $\Delta\delta > 0.02$ ppm (Figure 2-4).

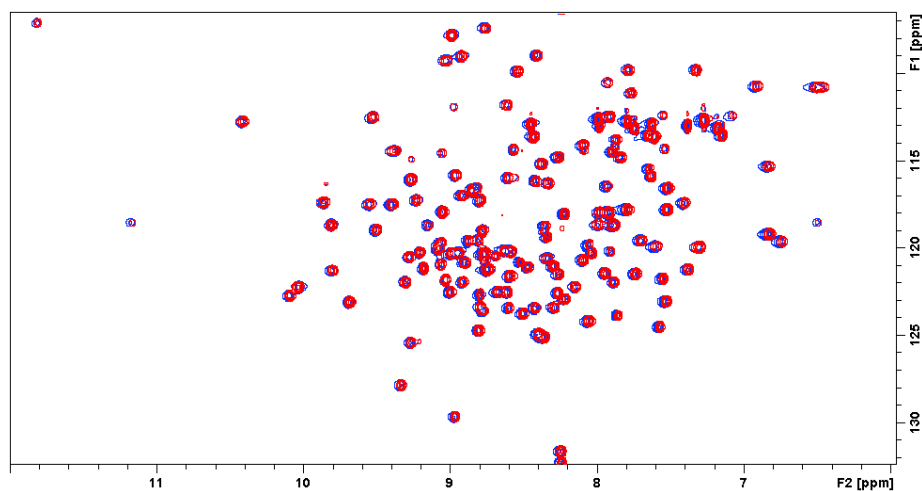


Figure 2. Overlay of ^1H - ^{15}N HSQC map of DHP A (blue curve) and DHP A with TCP (red) collected at 500 MHz.

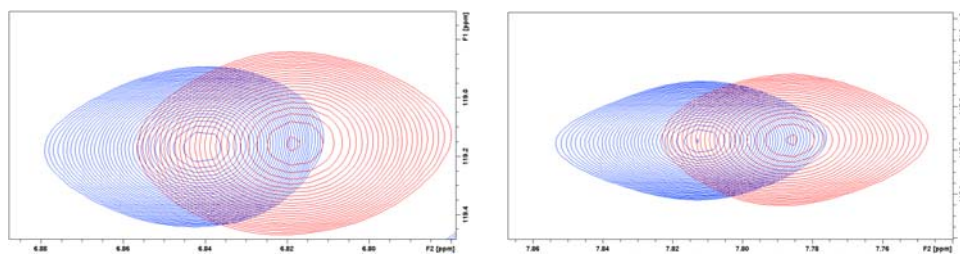


Figure 3. Close-up view of ^1H - ^{15}N shift perturbation for LEU 62 (left) and MET 63(right) collected at 500 MHz.

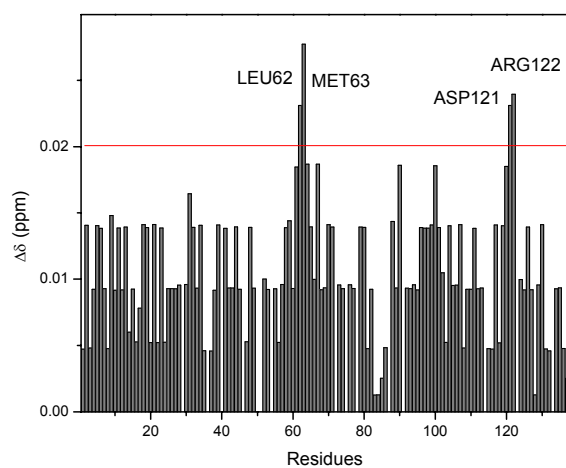


Figure 4. Plot of TCP-induced chemical shift perturbations ($\Delta\delta$) versus amino acid residue (those with $\Delta\delta > 0.02$ ppm labeled, indicating the potential binding site).

6.2.2 Backbone ^{15}N relaxation

The ^1H and ^{15}N chemical shift frequencies were detected for backbone amide NH groups that give rise to cross peaks in the HSQC spectrum of DHP A. Although there are 137 residues in DHP A, due to 2 proline residues (Pro 29 and Pro 75) that lack H^{N} protons, and there were a few regions in the 2-D spectra that significant spectral overlaps and weak signals, such that only 115 residues could be analyzed.

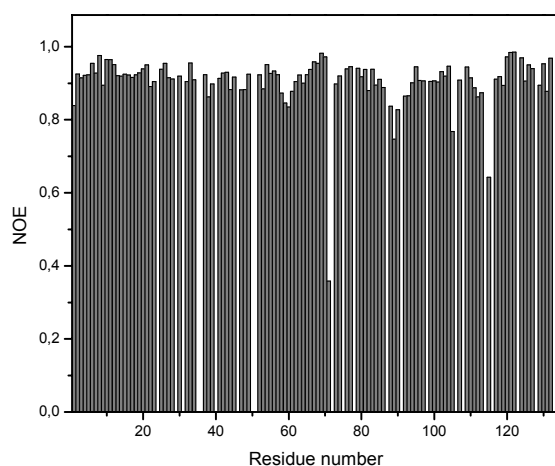


Figure 5. Backbone dynamics of DHP A with TCP based on ^{15}N relaxation data. $\{^1\text{H}\}$ - ^{15}N NOE values are plotted as a function of residue number. The relaxation data was recorded on a 16.4 T (700 MHz) spectrometer.

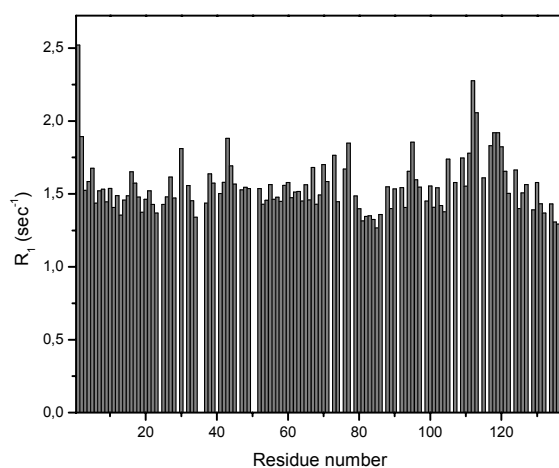


Figure 6. Relaxation rate $R_1=1/T_1$ are plotted as a function of residue number. The relaxation data was recorded on a 16.4 T (700 MHz) spectrometer.

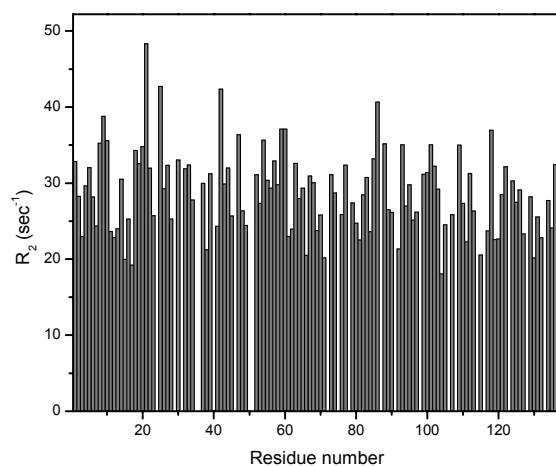


Figure 7. Relaxation rate $R_2=1/T_2$ are plotted as a function of residue number. The relaxation data was recorded on a 16.4 T (700 MHz) spectrometer.

To characterize protein dynamics, ^{15}N relaxation experiments (T_1 , T_2 , and $\{^1\text{H}\}$ - ^{15}N NOE) were measured on DHP A with and without TCP, respectively. The observed change in amide cross peak intensity is described by the single-exponential decay equation for the ^{15}N - T_1 and ^{15}N - T_2 experiments. $\{^1\text{H}\}$ - ^{15}N heteronuclear NOE values were obtained from the ratio of the intensity of $\{^1\text{H}\}$ - $^{15}\text{N}\}$ -HSQC peaks in the presence and absence of ^1H saturation. The observed ^{15}N relaxation parameters for the 115 residues of DHP A with TCP are shown in

Figures 5-7. The average R_1 rate at 700 MHz was 1.55 s^{-1} , while the average R_2 at 700 MHz was 28.89 s^{-1} , respectively. The average heteronuclear NOE was 0.907. The lower-than-average NOE values found at the residues of DHP A are likely to be caused by increased motions on the ps-ns time scale [18, 19]. Elevated R_2 value indicates conformational processes on the slow μs -ms time scale [18a, 19], such as ILE9, LYS47, VAL59 and PHE60.

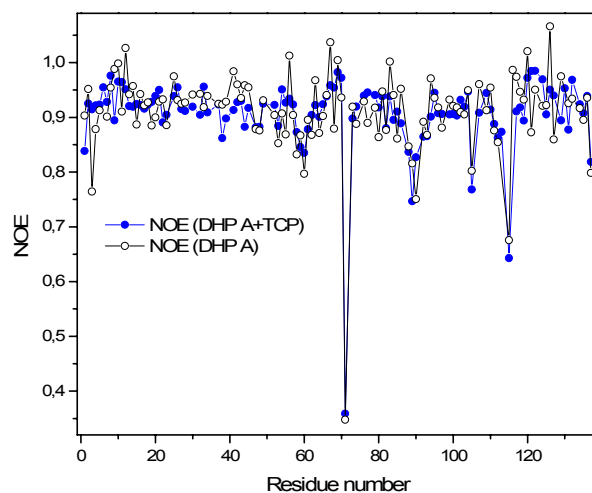


Figure 8. NOE of DHP A only sample (black), and DHP A in the presence of TCP (blue). The relaxation data was recorded on a 16.4 T (700 MHz) spectrometer.

Figure 8 and 9 show the $\{^1\text{H}\}$ - ^{15}N heteronuclear NOE values and R_1 of DHP A with and without TCP. The low NOE values are observed for the residues 71 and residue 115, which indicate the flexible regions (Figure 8) [19, 20]. Residues between 60 and 65, the residue 120 and 121 display consistently elevated R_1 values comparing to the DHP A only sample in the same segment, indicating that these residues exhibit higher nanosecond motions upon binding [20], as show in Figure 9. Interestingly, the helix region of residue 62, and residue 63 and the helix region of residue 121 and residue 122 also show larger chemical shift perturbations in the presence of TCP (Figure 4). The observed R_2 rate for the residues of DHP A without TCP is shown in Figures 10, the average R_2 rate at 700 MHz was 11.51 s^{-1} .

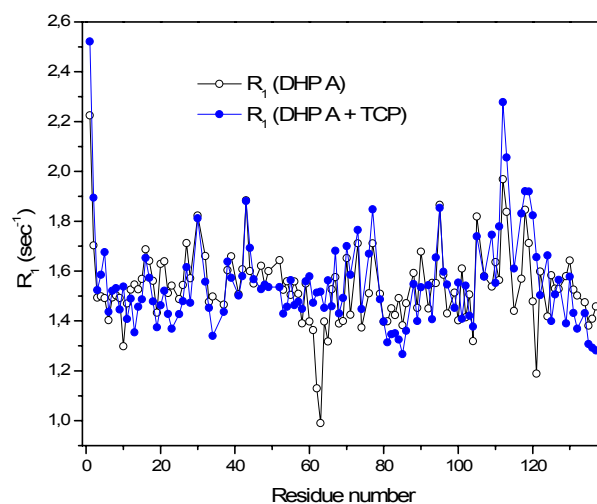


Figure 9. R_1 of DHP A only sample (black), and DHP A in the presence of TCP (blue). The relaxation data was recorded on a 16.4 T (700 MHz) spectrometer.

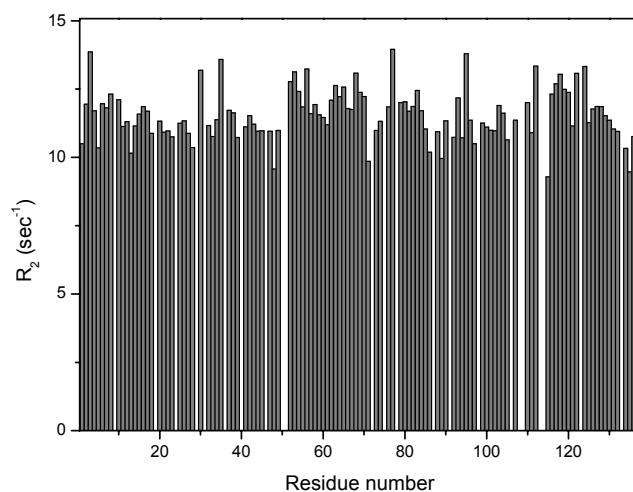


Figure 10. Relaxation rate $R_2=1/T_2$ are plotted as a function of residue number. The relaxation data was recorded on a 16.4 T (700 MHz) spectrometer.

6.2.3 Reduced spectral density mapping

Reduced spectral density mapping is a method to study the motion of each ^1H - ^{15}N bond vector at 3 different frequencies 0, ω_{N} and $0.87\omega_{\text{H}}$ from the experimentally derived relaxation parameters [20, 21]. In this method, the three

spectral density functions, $J(0)$, $J(\omega_N)$ and $J(0.87\omega_H)$ can be calculated from relaxation parameters, R_1 , R_2 and $\{^1\text{H}\}$ - ^{15}N NOE based on the following equations [18a, 19]:

Equation 1:

$$J(0.87\omega_H) = R_1(\text{NOE} - 1) \left(\frac{\gamma_N}{\gamma_H} \right) \left(\frac{4}{5d^2} \right)$$

Equation 2:

$$J(\omega_N) = \frac{R_1 - J(0.87\omega_H) \left(\frac{7d^2}{4} \right)}{\left(\frac{3d^2}{4} + c^2 \right)}$$

Equation 3:

$$J(0) = \frac{R_2 - J(\omega_N) \left(\frac{7d^2}{4} \right) - J(0.87\omega_H) \left(\frac{13d^2}{8} \right)}{\left(\frac{d^2}{2} + \frac{2c^2}{3} \right)}$$

Where the parameters d and c have been defined in Chapter 2.

The relaxation data as shown in Figure 5, 6 and 7 allowed us to extract the spectral density functions at 3 different frequencies: $J(0)$, $J(71 \text{ MHz})$, corresponding to $J(\omega_N)$ on a 700 MHz spectrometer, and $J(609 \text{ MHz})$, corresponding to $J(0.87\omega_H)$ on a 700 MHz spectrometer, as shown in Figure 11, 12 and 13.

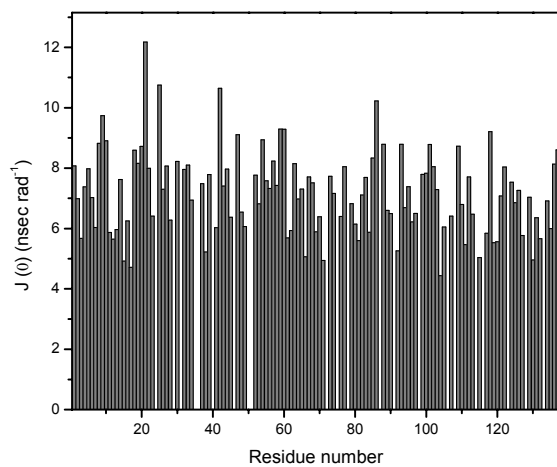


Figure 11. Reduced spectral density mapping analysis of DHP A with TCP using the ^{15}N relaxation data in Figure 5, 6 and 7. $J(0)$ is displayed as a function of protein sequence.

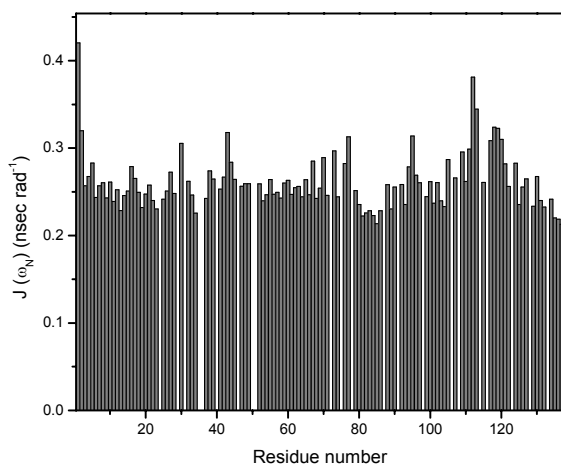


Figure 12. Reduced spectral density mapping analysis of DHP A with TCP using the ^{15}N relaxation data in Figure 5, 6 and 7. $J(\omega_{\text{N}})$ is displayed as a function of protein sequence.

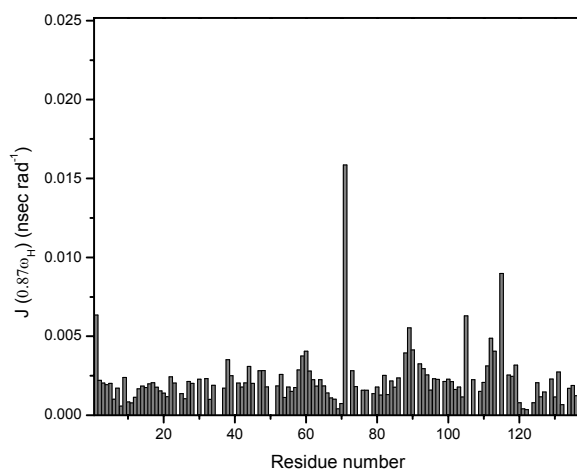


Figure 13. Reduced spectral density mapping analysis of DHP A with TCP using the ^{15}N relaxation data in Figure 5, 6 and 7. $J(0.87\omega_{\text{H}})$ is displayed as a function of protein sequence.

The average $J(0)$, $J(\omega_{\text{N}})$, and $J(0.87\omega_{\text{H}})$ values are 7.19 ns/radian, 0.26 ns/radian, 0.0023 ns/radian, respectively.

6.2.4 Interpretation of $J(\omega_{\text{N}})$ and $J(0.87\omega_{\text{H}})$ via Lipari-Szabo mapping

The reduced spectral density method does not separate the relative contributions of internal amide NH bond motions from overall global tumbling [18a]. The Lipari-Szabo model-free method [22-24] can be used to separate the relative effect of these motions on ^{15}N relaxation, which assumes an equation (Equation 4) between overall protein tumbling, the internal motions and the spectral density function [18a, 22, 23]:

Equation 4:

$$J(\omega) = \left(\frac{2}{5}\right) \left(\frac{S^2 \tau_m}{1 + (\omega \tau_m)^2} + \frac{(1 - S^2) \tau}{1 + (\omega \tau)^2} \right)$$

In which τ_m is the global tumbling correlation time of protein; S^2 is the generalized order parameter for the N-H bond vector, τ_e is effective correlation time of internal motions, which is related to τ by the equation $1/\tau = 1/\tau_m + 1/\tau_e$ [18a].

The Lipari-Szabo mapping technique uses simple graphical relationships to extract S^2 and τ_e from $J(\omega_N)$ and $J(0.87\omega_H)$ [18]. Using the crystal structure of DHP A, the rotational diffusion tensor parameters, D_{zz} ($1.68E+07 \text{ s}^{-1}$), D_{yy} ($1.91E+07 \text{ s}^{-1}$) and D_{xx} ($2.06E+07 \text{ s}^{-1}$) were simulated by the program HydroNMR [25]. The correlation time τ_m estimated by this method is 9 ns [25]. Figure 14 and 15 show the determination of the order parameter (S^2) for the backbone amide groups of THR71 and PHE115 by the Lipari-Szabo mapping. This analysis is based on the comparison of the experimentally determined spectral densities, $J(0.87\omega_H)^{\text{obs}}$ and $J(\omega_N)^{\text{obs}}$, to those predicted spectral densities (in the case of isotropic tumbling, internally rigid protein) denoted as $J(0.87\omega_H)^{\text{calculation}}$ and $J(\omega_N)^{\text{calculation}}$ [18a]. In the case of no internal motions and absolute NH bond rigidity ($S^2 = 1$), Equation 4 is simplified to Equation 5 [18a]. Equation 5:

$$J(\omega) = \left(\frac{2}{5}\right) \left(\frac{\tau_m}{1 + (\omega\tau_m)^2} \right)$$

The simulated spectral densities at $0.87\omega_H$ and ω_N for a rigid protein can be obtained at any correlation time τ_m ; this yields a $\{J(\omega_N)^{\text{calculation}}, J(0.87\omega_H)^{\text{calculation}}\}$ pair for each given τ_m . The triangular-shaped rigid tumbling curve composed of $\{J(\omega_N)^{\text{calculation}}, J(0.87\omega_H)^{\text{calculation}}\}$ points ($0 < \tau_m < 50 \text{ ns}$) is shown in Figure 14, 15. The point on the rigid tumbling curve corresponding to the simulated correlation time for DHP A (9 ns) is labeled as a blue square in Figure 14 and is denoted as $\{J(\omega_N)^{9\text{ns}}, J(0.87\omega_H)^{9\text{ns}}\}$. Any backbone ^{15}N on DHP A which is completely rigid should overlap with $\{J(\omega_N)^{9\text{ns}}, J(0.87\omega_H)^{9\text{ns}}\}$ [18a]. The presence of fast internal motions (for example, THR71 and PHE115) shows a shift away from the $\{J(\omega_N)^{9\text{ns}}, J(0.87\omega_H)^{9\text{ns}}\}$ point into the space within the triangle (Figure 14). A line can be drawn from the $\{J(\omega_N)^{9\text{ns}}, J(0.87\omega_H)^{9\text{ns}}\}$ point through the $\{J(0.87\omega_H)^{\text{obs}}$ and $J(\omega_N)^{\text{obs}}\}$ point to another point on the rigid tumbling curve [18a], the point of $\{J(0.87\omega_H)^{\tau}$ and $J(\omega_N)^{\tau}\}$ pair corresponds to the reduced spectral densities calculated from Equation 4 if only internal motions cause ^{15}N relaxation [18a].

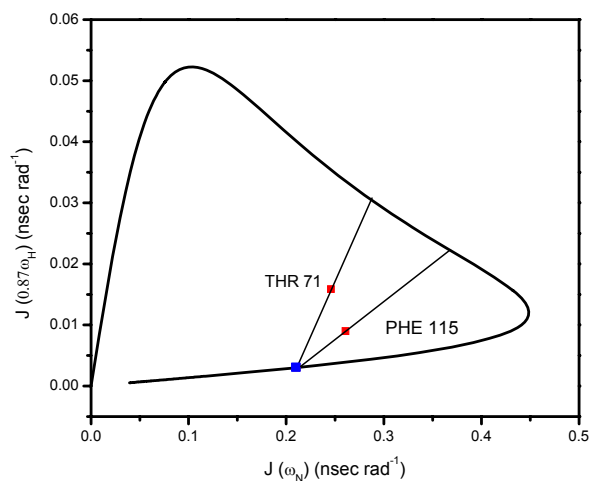


Figure 14. Lipari Szabo mapping method for THR71 and PHE115 (red squares). The blue square is the simulated $\{J(\omega_N), J(0.87\omega_H)\}$ pair (9 ns).

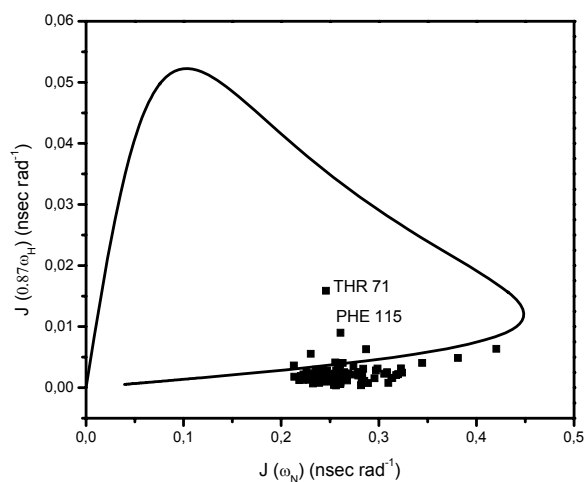


Figure 15. All of the data plotted.

S^2 is obtained by the distance of the observed point to the τ point over the distance from the τ_m point (9 ns) to the τ point (Figure 14), as shown in Equation 6 [18a]:

$$S^2 = \frac{\sqrt{[J(\omega_N)^{obs} - J(\omega_N)^\tau]^2 + [J(0.87\omega_H)^{obs} - J(0.87\omega_H)^\tau]^2}}{\sqrt{[J(\omega_N)^{\tau_m} - J(\omega_N)^\tau]^2 + [J(0.87\omega_H)^{\tau_m} - J(0.87\omega_H)^\tau]^2}}$$

The order parameters for THR 71 and PHE115 determined using this approach are 0.5 and 0.7, respectively. Since most of the observed $J(0.87\omega_H)^{obs}$ and

$J(\omega_N)^{\text{obs}}$ points cluster on the Lipari-Szabo map (Figure 15), the internal correlation times and S^2 for most of the amides are not reported by this method.

6.2.5 Lipari-Szabo model free analysis

The dynamic analysis was complemented with the Lipari-Szabo model free analysis [22-24]. The amide bond (NH) length was fixed to 1.02 Å, and ^{15}N chemical shift anisotropy was estimated as -172 ppm in our calculations. The global correlation time τ_m is calculated by using the most rigid residues using the program of Bruker Dynamics Center [26, 27]. For these calculations, suitable residues were selected. The residues with low T_2 values that undergo conformation exchange were excluded based on $T_2 < T_2(\text{mean}) - \text{SD}$, where SD is the standard deviation of T_2 , residues with large T_2 compared to T_1 were removed based on $\frac{[T_2 - T_2(\text{mean})]}{T_2} > 3 \frac{[T_1 - T_1(\text{mean})]}{T_1}$, and those residues with NOE value < 0.7 were removed [26, 27]. The selective residues yielded the global correlation time with an average estimate of 12 ns calculated by Bruker Dynamics Center based on fitting each of the selected residues to Equation 5 (the final τ_m is the average over all fitted τ_m of each residue) [27, 28]:

Equation 5:

$$J(\omega) = \left(\frac{2}{5}\right) \left(\frac{\tau_m}{1 + (\omega\tau_m)^2}\right)$$

The $J(0)$ is equal to $(2/5)\tau_m$ in the absence of internal motions [20]. A $J(0)$ value is less than $(2/5)\tau_m$, which indicates the subnanosecond flexibility of the N-H bond vector; a $J(0)$ is larger than $(2/5)\tau_m$, which indicates slow micro- to millisecond motions (R_{ex}) [20]. The $(2/5)\tau_m$ is 4.8 ns for DHP A with TCP, the $J(0)$ for most of the residues of DHP A with TCP is larger than 4.8 ns, it indicates that the relaxation R_2 is dominated by R_{ex} throughout the sequence, as shown in Figure 11.

The internal and global motions of protein molecule are separated by Lipari-Szabo model free analysis using the program of Bruker Dynamics Center [26, 27]. R_{ex} and S^2 (Figure 16 and 17) were extracted from each residue of DHP A

by fitting the $J(0)$, $J(\omega_N)$, and $J(0.87\omega_H)$ of each residue to five commonly used models (M1, M2, M3, M4 and M5).

The five models for the spectral density functions used in the program Bruker Dynamics Center are shown in following [26, 27]:

M1:

$$J(\omega) = \left(\frac{2}{5}\right) \tau_m \left[\frac{S^2}{1 + (\omega\tau_m)^2} \right]$$

M2

$$J(\omega) = \left(\frac{2}{5}\right) \tau_m \left[\frac{S^2}{1 + (\omega\tau_m)^2} + \frac{(1 - S^2)(\tau_m + \tau_e)\tau_e}{(\tau_m + \tau_e)^2 + (\omega\tau_m\tau_e)^2} \right]$$

M3

$$J(\omega) = \left(\frac{2}{5}\right) \tau_m \left[\frac{S^2}{1 + (\omega\tau_m)^2} \right] + R_{ex}$$

M4

$$J(\omega) = \left(\frac{2}{5}\right) \tau_m \left[\frac{S^2}{1 + (\omega\tau_m)^2} + \frac{(1 - S^2)(\tau_m + \tau_e)\tau_e}{(\tau_m + \tau_e)^2 + (\omega\tau_m\tau_e)^2} \right] + R_{ex}$$

M5

$$J(\omega) = \left(\frac{2}{5}\right) \tau_m \left[\frac{S^2}{1 + (\omega\tau_m)^2} + \frac{(1 - S_f^2)(\tau_m + \tau_f)\tau_f}{(\tau_m + \tau_f)^2 + (\omega\tau_m\tau_f)^2} \cdot \frac{(S_f^2 - S^2)(\tau_m + \tau_s)\tau_s}{(\tau_m + \tau_s)^2 + (\omega\tau_m\tau_s)^2} \right]$$

The average R_{ex} is 15.3 s^{-1} , the residues with larger exchange rates (Figure 16, GLY1, ILE9, LYS47, VAL59, PHE60, MET86, GLN88, and GLY112) were observed. The preliminary results from model-free analysis give information about the dynamics of DHP A in the presence of TCP.

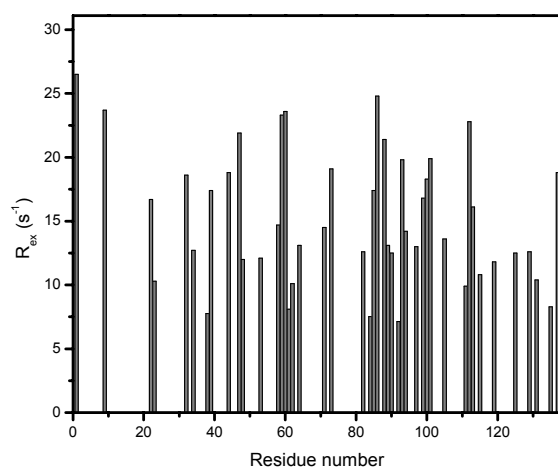


Figure 16. Model free analysis (Model 4) of ^{15}N relaxation data of DHP A with TCP, R_{ex} were extracted using the Bruker dynamics center program from the relaxation data shown in Figure 5, 6 and 7.

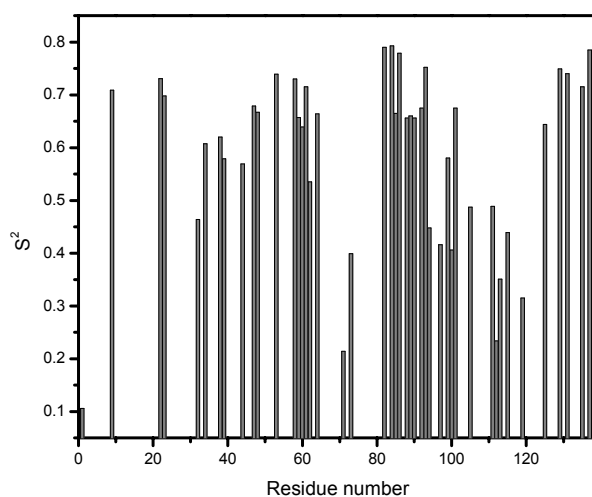


Figure 17. Model free analysis (Model 4) of ^{15}N relaxation data of DHP A with TCP, S^2 were extracted using the Bruker dynamics center program from the relaxation data shown in Figure 5, 6 and 7.

6.3 Conclusions

NMR relaxation measurements were used to study the dynamics of DHP A in solution in the presence of TCP. DHP A was labeled with ^{15}N , and NMR relaxation parameters T_1 and T_2 and $\{^1\text{H}\}$ - ^{15}N NOE were measured and

analyzed by reduced spectral density mapping and the Lipari-Szabo model free method. The preliminary ^{15}N relaxation data show the presence of slow conformational exchange in DHP A with TCP. As DHP A is important for catalytic oxidization of substrate (TCP), any information on the intrinsic dynamics of DHP A may correlate to essential motions involved in the catalytic oxidization reaction. Further work is needed to corroborate these findings and their significance for the catalytic oxidization reaction.

References of chapter 6

- [1] Hansen, D. F.; Vallurupalli, P.; Kay, L. E. *J Biomol NMR*, 2008, 41, 113-120.
- [2] Eisenmesser, E. Z.; Bosco, D.; Akke, M.; Kern, D. *Science*, 2002, 1520-1523.
- [3] Mittermaier, A.; Kay, L. E., *Science*, 2006, 312, 224-228
- [4] Eisenmesser, E. Z.; Millet, O.; Labeikovsky, W.; Korzhnev, D. M.; Wolf-Watz, M.; Bosco, D. A.; Skalicky, J. J.; Kay, L. E.; Kern, D. *Nature* 2005, 438, 117-121.
- [5] Henzler-Wildman, K. A.; Lei, M.; Thai, V.; Kerns, S. J.; Karplus, M.; Kern, D.; *Nature*, 2007, 450, 913-916.
- [6] Henzler-Wildman, K.; Kern, D.; *Nature*, 2007, 450, 964-972.
- [7] Korzhnev, D. M.; Kay, L. E. *Acc. Chem. Res.*, 2008, 41, 442-451
- [8] Kay, L. E., *Nat. Struct. Biol.*, 1998, 5, 513-517
- [9] Fraser, J. S.; Clarkson, M. W.; Degnan, S. C.; Erion, R.; Kern, D.; Alber, T.; *Nature*, 2009, 462, 669-673.
- [10] Thompson, M. K.; Franzen, S.; Davis, M. F.; Oliver, R. C.; Krueger, J. K.; *J. Phys. Chem. B*, 2011, 115, 4266-4272.
- [11] Lebioda, L.; LaCount, M. W.; Zhang, E.; Chen, Y. P.; Han, K.; Whitton, M. M.; Lincoln, D. E.; Woodin, S. A. 1999, *Nature* 401, 445.
- [12] Chen, Z.; De Serrano, V.; Betts, L.; Franzen, S. 2009, *Acta Crystallogr., Sect. D: Biol. Crystallogr.* 65, 34-40.
- [13] de Serrano, V.; Chen, Z. X.; Davis, M. F.; Franzen, S. 2007, *Acta Crystallogr., Sect. D: Biol. Crystallogr.* 63, 1094-1101.
- [14] Belyea, J.; Gilvey, L. B.; Davis, M. F.; Godek, M.; Sit, T. L.; Lommel, S. A.; Franzen, S. *Biochemistry*, 2005 44, 15637-15644.

- [15] Osborne, R. L.; Taylor, L. O.; Han, K. P.; Ely, B.; Dawson, J. H. *Biochem. Biophys. Res. Commun.* 2004, 324, 1194-1198.
- [16] Davis, M. F.; Bobby, B. G.; Franzen, S. *Biochemistry* 2010, 49, 1199-1206.
- [17] Manvilla, B. A.; Wauchope, O.; Seley-Radtke, K. L.; Drohat, A. C. *Biochemistry*, 2011, 50, 10540-10549.
- [18] (a) Henkels, C. H.; Chang, Y.; Chamberlin, S. I.; Oas, T. G. *Biochemistry* 2007, 46, 15062-15075. (b) Andrec, M.; Montelione, G. T.; Levy, R. M. J. *Biomol. NMR* 2000, 18, 83-100.
- [19] Jarymowycz, V. A; Stone, M. J., *Chem. Rev.* 2006, 106, 1624-1671.
- [20] Twomey, E. C.; Cordasco, D. F.; Wei, Y. *Biochim Biophys Acta.* 2012, 1824, 1382-1393.
- [21] Farrow, N. A.; Zhang, O.; Forman-Kay, J. D.; Kay, L. E., *Biochemistry*, 1995, 34, 868-878.
- [22] Lipari, G.; Szabo, A. J. *Am. Chem. Soc.*, 1982, 104, 4546-4559.
- [23] Lipari, G.; Szabo, A. J. *Am. Chem. Soc.*, 1982, 104, 4559-4570
- [24] Clore, G. M.; Szabo, A.; Bax, A.; Kay, L. E.; Driscoll, P. C.; Gronenborn, A. M. *J. Am. Chem. Soc.*, 1990, 112, 4989-4991
- [25] de la Torre, J. G.; Huertas, M. L; Carrasco, B. J. *Magn. Reson.* 2000, 147, 138-146.
- [26] <http://www.bruker.com/en/products/mr/nmr/nmr-software/software.html>
- [27] Software Manual (version 2.0) of Bruker Dynamics Center
- [28] Kay, L. E.; Torchia, D. A.; Bax, A. *Biochemistry*, 1989, 28, 8972-8979.

7 Summary and outlook

It was found that lysozyme can be used as a pH sensitive valve for the controlled release of drug from mesoporous silica. The operation of this valve is based on pH-induced conformational change of lysozyme confined in the pores of native porous silica. An advantage of our capping method is that drug molecules can be easily encapsulated inside the porous silica without surface functionalization. Another advantage of this system is that the creation of toxic species can be avoided because of the use of biomolecules and native porous silica. This delivery system may be an ideal carrier for targeting oral drug administration applications through a pH-responsive mechanism. For example, in the stomach (at low pH), the enlarged lysozyme molecule can block the pore outlets and thus the drug release is decreased. In the intestine (at high pH), lysozyme can open the pathway for the release of drug molecules. This proof of concept might provide a general route for the use of other proteins capping agents for the delivery system. For example, the conformation state of BSA is sensitive to pH [1], and the different pore size of porous silica materials can be prepared [2], thus, it is possible to find a porous silica with a “proper” pore size which can fit the conformational change of BSA, a new drug delivery system based on mesoporous silica and protein might be obtained.

The study in chapter 5 has shown that important information about the distribution of donor and acceptor molecules in the pore space of mesoporous materials can be derived from fluorescence lifetime measurements by means of FLIM. Further work is needed to separate the effect of donor-to-acceptor molar ratio D:A from the overall concentration of dye molecules on the measured mean donor-to-acceptor distance r_{DA} . The FRET-FLIM method outlined in the case study will be applied to measure distances between protein molecules localized in the pores of mesoporous silica. For this purpose the proteins have to be labeled with D and A dyes. The fluorescence lifetime of the labeled lysozyme in porous silica can be determined as a function of the known protein concentration in the matrix using FLIM. Of particular interest is the question if the protein molecules tend to form clusters in the pores.

The ^{15}N relaxation analysis (reduced spectral density mapping and model free analysis) reveal the presence of conformational heterogeneity on the μs - ms time scale in DHP A with TCP. Since DHP A is essential for inducing oxidization of substrate (TCP), any information pertaining to the inherent motions of DHP A may correlate to important motions involved in the catalytic cycle of TCP. Although in the method of model-free analysis or reduced spectral density mapping, this exchange contribution to R_2 (designated R_{ex}) can be identified for DHP A with TCP, but its physical interpretation remains obscure [3]. The microsecond to millisecond motions of DHP A are of primary interest as the slow time scale motion of protein is relevant to its function [4], NMR CPMG (Carr-Purcell-Meiboom-Gill) relaxation dispersion experiment (as shown in chapter 2.6.6) [5] are necessary to confirm the presence of exchange R_{ex} and accurately estimate the microscopic chemical exchange rates (k_{ex}) for residues involved in exchange processes.

References of chapter 7

- [1] Tsai, D.-H.; DelRio, F.W.; Keene, A.M.; Tyner, K.M.; MacCuspie, R.I.; Cho, T.J.; Zachariah, M.R.; Hackley, V.A. *Langmuir* 2011, 27, 2464-2477.
- [2] (a) Kresge, C. T.; Leonowicz, M. E.; Roth, W. J.; Vartuli, J. C.; Beck, J. S. *Nature*, 1992, 359, 710-712. (b) Zhao, D.; Feng, J.; Huo, Q.; Melosh, N.; Fredrickson, G. H.; Chmelka, B. F.; Stucky, G. D. *Science* 1998, 279, 548-552.
- [3] Jarymowycz, V. A.; Stone, M. J. *Chem. Rev.* 2006, 106, 1624–1671.
- [4] Eisenmesser, E. Z.; Millet, O.; Labeikovsky, W.; Korzhnev, D. M.; Wolf-Watz, M.; Bosco, D. A.; Skalicky, J. J.; Kay, L. E.; Kern, D. *Nature* 2005, 438, 117-121.
- [5] (a) Korzhnev, D. M.; Kay, L. E. *Acc. Chem. Res.*, 2008, 41, 442-451. (b) Mittermaier, A.; Kay, L. E. *Science* 2006, 312, 224-228.

Appendix

A1 Publications

Mengjun Xue and Gerhard H. Findenegg, Lysozyme as a pH-Responsive Valve for Controlled Release of Guest Molecules from Mesoporous Silica. *Langmuir* 2012, 28, 17578-17584.

Bhuvnesh Bharti, Mengjun Xue, Jens Meissner, Viviana Cristiglio, and Gerhard H. Findenegg, Assembling Wormlike Micelles in Tubular Nanopores by Tuning Surfactant–Wall Interactions. *Journal of the American Chemical Society*, 2012, 134, 14756-14759.

Mengjun Xue and Gerhard H. Findenegg, Energy Transfer between Dye Molecules in MCM-41 Studied by Fluorescence Lifetime Imaging, to be submitted.

Mengjun Xue, Hanna Gracz, Gerhard H. Findenegg, Stefan Franzen, Intrinsic Dynamics of DHP A Underlies Its Enzymatic Function. In preparation.

Mengjun Xue and Gerhard H. Findenegg, Single Molecule Fluorescence Spectroscopy Studies of Unfolded Protein in Mesoporous Silica. In preparation.

A2 Tables of NMR data

Table 1. ^{15}N relaxation NMR data for DHP A with TCP at 25 °C and 700MHz.

Peak name	NOE	R_1 (sec $^{-1}$)	R_2 (sec $^{-1}$)
GLY [1]	0.838	2.522	32.824
PHE [2]	0.925	1.894	28.264
LYS [3]	0.915	1.524	22.946
GLN [4]	0.922	1.585	29.606
ASP [5]	0.923	1.677	32.013
ILE [6]	0.955	1.437	28.160
ALA [7]	0.928	1.522	24.346
THR [8]	0.976	1.531	35.226
ILE [9]	0.894	1.446	38.769
ARG [10]	0.965	1.537	35.567
GLY [11]	0.964	1.408	23.626
ASP [12]	0.951	1.489	22.807
LEU [13]	0.920	1.354	23.970
ARG [14]	0.919	1.457	30.492
THR [15]	0.924	1.487	19.966
TYR [16]	0.923	1.653	25.244
ALA [17]	0.916	1.573	19.210
GLN [18]	0.923	1.479	34.300
ASP [19]	0.928	1.374	32.555
ILE [20]	0.939	1.463	34.800
PHE [21]	0.950	1.521	48.332
LEU [22]	0.891	1.428	31.952
ALA [23]	0.905	1.369	25.719
LEU [25]	0.939	1.428	42.713
ASN [26]	0.955	1.479	29.236
LYS [27]	0.915	1.616	32.335
TYR [28]	0.912	1.473	25.262
ASP [30]	0.919	1.812	33.052
ARG [32]	0.905	1.557	31.870
ARG [33]	0.956	1.453	32.376
TYR [34]	0.909	1.340	27.780
ASN [37]	0.924	1.436	29.954
TYR [38]	0.862	1.638	21.228
VAL [39]	0.898	1.573	31.205
LYS [41]	0.913	1.502	24.310
SER [42]	0.928	1.580	42.373
ASP [43]	0.930	1.882	29.882
GLN [44]	0.883	1.693	31.975
GLU [45]	0.917	1.568	25.672
LYS [47]	0.882	1.528	36.346
SER [48]	0.883	1.545	26.345
MET [49]	0.925	1.536	24.444
PHE [52]	0.923	1.536	31.107
GLY [53]	0.884	1.429	27.340
ASP [54]	0.951	1.457	35.624
HIS [55]	0.927	1.564	30.375
THR [56]	0.934	1.463	29.344

Appendix

GLU [57]	0.923	1.477	32.909
LYS [58]	0.873	1.449	29.749
VAL [59]	0.846	1.559	37.092
PHE [60]	0.835	1.578	37.087
ASN [61]	0.878	1.473	22.978
LEU [62]	0.904	1.513	23.948
MET [63]	0.922	1.517	32.591
MET [64]	0.900	1.452	27.976
GLU [65]	0.924	1.563	29.330
VAL [66]	0.938	1.459	20.504
ALA [67]	0.958	1.682	30.939
ASP [68]	0.954	1.430	30.054
ARG [69]	0.982	1.493	23.742
ALA [70]	0.972	1.701	25.798
THR [71]	0.359	1.585	20.169
CYS [73]	0.898	1.766	31.092
VAL [74]	0.920	1.448	28.714
LEU [76]	0.939	1.670	25.843
ALA [77]	0.945	1.848	32.351
ASP [79]	0.941	1.486	27.407
ALA [80]	0.918	1.397	24.703
ASN [81]	0.938	1.314	22.522
THR [82]	0.880	1.346	28.453
LEU [83]	0.938	1.350	30.736
VAL [84]	0.895	1.325	23.618
GLN [85]	0.910	1.267	33.190
MET [86]	0.889	1.360	40.644
GLN [88]	0.837	1.548	35.137
HIS [89]	0.746	1.400	26.492
SER [90]	0.827	1.535	26.138
LEU [92]	0.865	1.543	21.329
THR [93]	0.865	1.407	35.048
THR [94]	0.901	1.655	26.956
GLY [95]	0.945	1.854	29.774
ASN [96]	0.907	1.598	25.109
PHE [97]	0.906	1.547	26.181
LYS [99]	0.905	1.452	31.165
LEU [100]	0.906	1.554	31.378
PHE [101]	0.903	1.409	35.027
VAL [102]	0.932	1.542	32.203
ALA [103]	0.919	1.421	29.202
LEU [104]	0.946	1.377	18.037
VAL [105]	0.768	1.739	24.512
TYR [107]	0.908	1.578	25.827
ARG [109]	0.944	1.746	34.981
ALA [110]	0.914	1.553	27.329
SER [111]	0.887	1.780	22.265
GLY [112]	0.863	2.278	31.265
GLN [113]	0.873	2.056	26.326
PHE [115]	0.643	1.610	20.521
SER [117]	0.911	1.831	23.732
GLN [118]	0.918	1.920	36.935

Appendix

SER [119]	0.894	1.920	22.567
TRP [120]	0.972	1.824	22.630
ASP [121]	0.984	1.655	28.465
ARG [122]	0.985	1.504	32.154
GLY [124]	0.969	1.664	30.264
LYS [125]	0.905	1.399	27.480
ASN [126]	0.950	1.507	29.119
LEU [127]	0.940	1.565	23.315
SER [129]	0.894	1.390	28.182
ALA [130]	0.953	1.578	20.162
LEU [131]	0.877	1.432	25.545
SER [132]	0.968	1.369	22.806
ALA [134]	0.924	1.431	27.707
GLY [135]	0.907	1.307	24.076
MET [136]	0.939	1.292	32.417
LYS [137]	0.819	1.281	34.276

Table 2. Amide ^1H and amide ^{15}N resonances and ^{15}N relaxation NMR data for DHP A at 25 °C and 700MHz.

Peak name	^{15}N - ^1H (ppm)	^{15}N (ppm)	NOE	R_1 (sec $^{-1}$)	R_2 (sec $^{-1}$)
GLY [1]	9.565	112.310	0.903	2.225	10.500
PHE [2]	8.601	123.249	0.951	1.703	11.943
LYS [3]	8.601	114.232	0.764	1.493	13.860
GLN [4]	8.258	121.358	0.878	1.499	11.702
ASP [5]	8.791	122.468	0.913	1.492	10.351
ILE [6]	7.900	120.045		1.403	11.959
ALA [7]	7.363	121.077	0.901	1.494	11.813
THR [8]	9.208	120.155	0.954	1.502	12.313
ILE [9]	8.795	123.249	0.988	1.492	
ARG [10]	8.809	116.404	0.998	1.299	12.114
GLY [11]	8.234	106.169	0.911	1.470	11.130
ASP [12]	7.877	121.827	1.026	1.525	11.306
LEU [13]	7.571	124.374	0.942	1.546	10.155
ARG [14]	8.860	116.607	0.957	1.526	11.147
THR [15]	7.627	115.779	0.887	1.569	11.586
TYR [16]	7.989	118.545	0.942	1.688	11.854
ALA [17]	9.083	119.811	0.922	1.641	11.691
GLN [18]	7.905	114.388	0.927	1.561	10.876
ASP [19]	8.350	118.608	0.885	1.433	
ILE [20]	9.064	120.842	0.900	1.629	11.327
PHE [21]	9.009	122.421	0.928	1.639	10.917
LEU [22]	9.565	117.373	0.933	1.512	10.968
ALA [23]	8.508	123.593	0.885	1.542	10.753
LEU [25]	9.241	117.123	0.975	1.488	11.247
ASN [26]	8.972	115.670	0.931	1.545	11.340
LYS [27]	8.615	122.405	0.925	1.712	10.881
TYR [28]	8.332	116.154	0.927	1.571	10.360
ASP [30]	9.519	118.905	0.941	1.823	13.186
ARG [32]	8.420	115.998	0.943	1.660	11.169
ARG [33]	7.877	114.029	0.918	1.477	10.767

Appendix

TYR [34]	7.516	116.436	0.939	1.498	11.383
ASN [37]	8.786	118.889	0.925	1.466	11.725
TYR [38]	8.925	116.842	0.923	1.604	11.628
VAL [39]	8.058	124.140	0.929	1.659	10.726
LYS [41]	7.516	117.639	0.984	1.507	11.113
SER [42]	10.117	122.702	0.960	1.608	11.534
ASP [43]	9.709	122.983	0.935	1.885	11.211
GLN [44]	8.805	117.170	0.958	1.600	10.954
GLU [45]	8.313	120.920	0.954	1.550	10.974
LYS [47]	8.624	115.935	0.878	1.621	10.958
SER [48]	7.919	112.341	0.876	1.543	9.567
MET [49]	8.401	124.843	0.931	1.600	10.984
PHE [52]	8.044	120.186	0.904	1.644	12.772
GLY [53]	8.545	109.810	0.853	1.525	13.124
ASP [54]	9.041	121.686	0.907	1.559	12.412
HIS [55]	8.897	120.702	0.869	1.504	11.846
THR [56]	8.939	108.919	1.013	1.558	13.232
GLU [57]	8.424	123.343	0.904	1.509	11.602
LYS [58]	7.692	119.420	0.832	1.390	11.937
VAL [59]	7.594	119.795	0.867	1.550	11.554
PHE [60]	7.914	116.295	0.797	1.398	11.462
ASN [61]	8.749	121.092	0.895	1.364	11.198
LEU [62]	6.802	119.045	0.868	1.130	12.097
MET [63]	7.771	117.623	0.967	0.990	12.629
MET [64]	8.253	114.670	0.871	1.398	12.219
GLU [65]	7.724	121.342	0.903	1.318	12.568
VAL [66]	8.369	118.889	0.941	1.527	11.790
ALA [67]	8.670	122.374	1.037	1.576	11.750
ASP [68]	8.800	119.358	0.879	1.389	13.079
ARG [69]	7.831	114.654	1.004	1.400	12.376
ALA [70]	7.543	121.608	0.936	1.652	12.227
THR [71]	8.211	117.842	0.348	1.424	9.854
CYS [73]	8.986	103.465	0.919	1.711	10.985
VAL [74]	8.290	123.296	0.888	1.374	11.319
LEU [76]	9.811	121.124	0.929	1.511	11.850
ALA [77]	9.347	127.702	0.890	1.712	13.960
ASP [79]	7.525	122.905	0.918	1.509	12.010
ALA [80]	8.225	122.827	0.864	1.396	12.033
ASN [81]	9.287	115.967	0.947	1.399	11.685
THR [82]	9.069	117.842	0.877	1.450	11.867
LEU [83]	9.305	120.405	1.002	1.424	12.446
VAL [84]	9.848	118.608	0.941	1.492	11.710
GLN [85]	9.894	117.248	0.861	1.383	11.034
MET [86]	10.080	122.171	0.952	1.471	10.186
GLN [88]	9.398	117.358	0.847	1.593	10.936
HIS [89]	9.398	114.310	0.816	1.453	9.958
SER [90]	7.914	117.904	0.750	1.678	11.337
LEU [92]	7.293	119.827	0.892	1.450	10.735
THR [93]	9.023	109.138	0.868	1.553	12.170
THR [94]	10.409	112.560	0.971	1.552	10.720
GLY [95]	8.406	108.810	0.936	1.865	13.795
ASN [96]	7.882	118.545	0.918	1.585	11.362

PHE [97]	6.815	115.185	0.881	1.430	10.499
LYS [99]	7.404	117.358	0.932	1.514	11.259
LEU [100]	6.732	119.498	0.921	1.402	11.103
PHE [101]	7.636	115.264	0.918	1.611	10.992
VAL [102]	8.768	123.514	0.910	1.414	10.978
ALA [103]	8.471	120.983	0.905	1.506	11.898
LEU [104]	8.772	120.233	0.950	1.318	11.614
VAL [105]	8.610	121.467	0.802	1.819	10.639
TYR [107]	8.916	121.842	0.960	1.579	11.364
ARG [109]	8.981	120.170	0.913	1.538	
ALA [110]	8.081	120.514	0.954	1.636	12.011
SER [111]	7.854	113.716	0.876	1.564	10.903
GLY [112]	8.624	111.732	0.854	1.968	13.343
GLN [113]	8.587	120.123		1.838	
PHE [115]	7.951	121.311	0.676	1.440	9.286
SER [117]	8.332	119.201	0.974	1.569	12.696
GLN [118]	9.194	121.045	0.947	1.846	13.035
SER [119]	7.970	117.826	0.932	1.713	12.495
TRP [120]	7.849	123.702	1.021	1.478	12.379
ASP [121]	8.531	120.624	0.873	1.189	11.150
ARG [122]	8.058	119.733	0.950	1.599	13.074
GLY [124]	8.758	107.247	0.921	1.418	13.333
LYS [125]	8.137	122.108	0.922	1.583	11.274
ASN [126]	8.879	119.483	1.066	1.529	11.772
LEU [127]	9.268	125.312	0.859	1.529	11.868
SER [129]	8.081	113.888	0.975	1.580	11.519
ALA [130]	8.355	124.921		1.643	11.359
LEU [131]	9.310	121.874	0.925	1.526	11.039
SER [132]	8.378	115.045	0.934	1.501	10.944
ALA [134]	8.267	122.452	0.917	1.475	10.334
GLY [135]	8.248	105.544	0.895	1.381	9.468
MET [136]	8.809	124.593	0.936	1.409	10.759
LYS [137]	9.009	133.734	0.798	1.458	8.011

Table 3. Spectral densities ($J(0)$, $J(\omega_N)$ and $J(0.87\omega_H)$) derived from backbone ^{15}N relaxation NMR data obtained for DHP A in the presence of TCP.

name	$J(0)$ (nsec rad^{-1})	$J(\omega_N)$ (nsec rad^{-1})	$J(0.87\omega_H)$ (nsec rad^{-1})
GLY [1]	8.07E-09	4.20E-10	6.36E-12
PHE [2]	6.99E-09	3.20E-10	2.21E-12
LYS [3]	5.68E-09	2.57E-10	2.03E-12
GLN [4]	7.37E-09	2.67E-10	1.94E-12
ASP [5]	7.98E-09	2.83E-10	2.02E-12
ILE [6]	7.02E-09	2.44E-10	1.02E-12
ALA [7]	6.04E-09	2.57E-10	1.71E-12
THR [8]	8.82E-09	2.60E-10	5.78E-13
ILE [9]	9.74E-09	2.43E-10	2.39E-12
ARG [10]	8.91E-09	2.61E-10	8.35E-13
GLY [11]	5.87E-09	2.39E-10	7.82E-13
ASP [12]	5.65E-09	2.52E-10	1.14E-12
LEU [13]	5.96E-09	2.29E-10	1.68E-12

Appendix

ARG [14]	7.62E-09	2.46E-10	1.84E-12
THR [15]	4.92E-09	2.51E-10	1.75E-12
TYR [16]	6.25E-09	2.79E-10	2.00E-12
ALA [17]	4.71E-09	2.65E-10	2.07E-12
GLN [18]	8.59E-09	2.50E-10	1.78E-12
ASP [19]	8.16E-09	2.32E-10	1.54E-12
ILE [20]	8.72E-09	2.48E-10	1.40E-12
PHE [21]	1.22E-08	2.58E-10	1.19E-12
LEU [22]	7.99E-09	2.40E-10	2.44E-12
ALA [23]	6.41E-09	2.30E-10	2.04E-12
LEU [25]	1.07E-08	2.41E-10	1.37E-12
ASN [26]	7.29E-09	2.51E-10	1.05E-12
LYS [27]	8.07E-09	2.72E-10	2.14E-12
TYR [28]	6.28E-09	2.48E-10	2.03E-12
ASP [30]	8.23E-09	3.06E-10	2.28E-12
ARG [32]	7.96E-09	2.62E-10	2.32E-12
ARG [33]	8.10E-09	2.46E-10	1.01E-12
TYR [34]	6.94E-09	2.26E-10	1.90E-12
ASN [37]	7.48E-09	2.42E-10	1.71E-12
TYR [38]	5.22E-09	2.74E-10	3.52E-12
VAL [39]	7.78E-09	2.65E-10	2.51E-12
LYS [41]	6.03E-09	2.53E-10	2.03E-12
SER [42]	1.06E-08	2.67E-10	1.78E-12
ASP [43]	7.41E-09	3.18E-10	2.05E-12
GLN [44]	7.97E-09	2.84E-10	3.10E-12
GLU [45]	6.37E-09	2.64E-10	2.03E-12
LYS [47]	9.11E-09	2.56E-10	2.82E-12
SER [48]	6.54E-09	2.59E-10	2.83E-12
MET [49]	6.06E-09	2.59E-10	1.81E-12
PHE [52]	7.76E-09	2.59E-10	1.85E-12
GLY [53]	6.81E-09	2.40E-10	2.58E-12
ASP [54]	8.93E-09	2.47E-10	1.12E-12
HIS [55]	7.57E-09	2.64E-10	1.79E-12
THR [56]	7.32E-09	2.47E-10	1.51E-12
GLU [57]	8.23E-09	2.49E-10	1.76E-12
LYS [58]	7.43E-09	2.43E-10	2.88E-12
VAL [59]	9.29E-09	2.60E-10	3.75E-12
PHE [60]	9.29E-09	2.63E-10	4.06E-12
ASN [61]	5.69E-09	2.47E-10	2.81E-12
LEU [62]	5.93E-09	2.55E-10	2.26E-12
MET [63]	8.15E-09	2.56E-10	1.84E-12
MET [64]	6.97E-09	2.44E-10	2.25E-12
GLU [65]	7.31E-09	2.64E-10	1.86E-12
VAL [66]	5.06E-09	2.47E-10	1.41E-12
ALA [67]	7.70E-09	2.85E-10	1.10E-12
ASP [68]	7.51E-09	2.42E-10	1.02E-12
ARG [69]	5.89E-09	2.54E-10	4.17E-13
ALA [70]	6.39E-09	2.89E-10	7.39E-13
THR [71]	4.94E-09	2.46E-10	1.59E-11
CYS [73]	7.73E-09	2.97E-10	2.82E-12
VAL [74]	7.16E-09	2.44E-10	1.81E-12
LEU [76]	6.40E-09	2.82E-10	1.58E-12

Appendix

ALA [77]	8.04E-09	3.13E-10	1.58E-12
ASP [79]	6.82E-09	2.52E-10	1.38E-12
ALA [80]	6.14E-09	2.36E-10	1.79E-12
ASN [81]	5.60E-09	2.22E-10	1.27E-12
THR [82]	7.11E-09	2.26E-10	2.52E-12
LEU [83]	7.69E-09	2.28E-10	1.30E-12
VAL [84]	5.87E-09	2.23E-10	2.17E-12
GLN [85]	8.33E-09	2.13E-10	1.77E-12
MET [86]	1.02E-08	2.28E-10	2.36E-12
GLN [88]	8.79E-09	2.58E-10	3.94E-12
HIS [89]	6.60E-09	2.30E-10	5.54E-12
SER [90]	6.49E-09	2.55E-10	4.14E-12
LEU [92]	5.26E-09	2.58E-10	3.26E-12
THR [93]	8.79E-09	2.36E-10	2.95E-12
THR [94]	6.69E-09	2.78E-10	2.56E-12
GLY [95]	7.38E-09	3.14E-10	1.59E-12
ASN [96]	6.22E-09	2.69E-10	2.31E-12
PHE [97]	6.50E-09	2.60E-10	2.27E-12
LYS [99]	7.79E-09	2.44E-10	2.14E-12
LEU [100]	7.83E-09	2.62E-10	2.28E-12
PHE [101]	8.78E-09	2.37E-10	2.13E-12
VAL [102]	8.04E-09	2.61E-10	1.64E-12
ALA [103]	7.29E-09	2.40E-10	1.79E-12
LEU [104]	4.44E-09	2.33E-10	1.15E-12
VAL [105]	6.05E-09	2.87E-10	6.29E-12
TYR [107]	6.41E-09	2.66E-10	2.26E-12
ARG [109]	8.73E-09	2.96E-10	1.52E-12
ALA [110]	6.79E-09	2.62E-10	2.08E-12
SER [111]	5.47E-09	2.99E-10	3.13E-12
GLY [112]	7.71E-09	3.81E-10	4.88E-12
GLN [113]	6.47E-09	3.45E-10	4.06E-12
PHE [115]	5.04E-09	2.61E-10	8.98E-12
SER [117]	5.84E-09	3.09E-10	2.54E-12
GLN [118]	9.21E-09	3.24E-10	2.46E-12
SER [119]	5.53E-09	3.23E-10	3.18E-12
TRP [120]	5.56E-09	3.10E-10	7.97E-13
ASP [121]	7.07E-09	2.82E-10	4.08E-13
ARG [122]	8.04E-09	2.56E-10	3.55E-13
GLY [124]	7.53E-09	2.83E-10	7.93E-13
LYS [125]	6.85E-09	2.36E-10	2.06E-12
ASN [126]	7.26E-09	2.55E-10	1.17E-12
LEU [127]	5.77E-09	2.65E-10	1.47E-12
SER [129]	7.03E-09	2.34E-10	2.29E-12
ALA [130]	4.96E-09	2.67E-10	1.16E-12
LEU [131]	6.35E-09	2.40E-10	2.74E-12
SER [132]	5.66E-09	2.33E-10	6.77E-13
ALA [134]	6.91E-09	2.42E-10	1.70E-12
GLY [135]	5.99E-09	2.20E-10	1.89E-12
MET [136]	8.13E-09	2.19E-10	1.23E-12
LYS [137]	8.61E-09	2.13E-10	3.63E-12

A3

Assembling wormlike micelles in tubular nanopores by tuning surfactant-wall interactions*

Bhuvnesh Bharti,[†] Mengjun Xue,[†] Jens Meissner,[†] Viviana Cristiglio[‡]
and Gerhard H. Findenegg^{*†}

[†]Technische Universität Berlin, Institut für Chemie, Stranski Laboratorium,
Strasse des 17. Juni 124, D-10623 Berlin, Germany

[‡]Institut Laue Langevin, Large Scale Structures group, 6, rue Jules Horowitz,
BP 156 F 38042, Grenoble, France.

Corresponding Author

findenegg@chem.tu-berlin.de

Molecular assemblies are strongly influenced by confinement in space. The constraints imposed by the bounding surfaces can induce new structures and open pathways to materials with unique properties [1]. This concept has been demonstrated for diblock copolymers (formed by two chemically different polymers joined together on one end), for which the microphase separation in cylindrical pores can lead to cylindrical or helical structures or concentric layers, depending on the size ratio of the two blocks and the repeat period of the block copolymer in relation to the pore size [2-4]. Confinement-induced self-organization of block copolymers has been observed in pores of typically 100 nm, but simulation studies have reported similar phenomena for short-chain amphiphiles in nanotubes of typically 10 nm diameter. A cornucopia of polymorphic surfactant assembly structures, including single- and double-stranded wormlike or spiral micelles, was presented in a study by Arai et al. [5]. However, this study was focusing on the self-assembly in an isolated pore and cannot tell if the confinement-induced aggregates also exist at equilibrium with a bulk solution. It is well-established that wormlike micelles in many ways behave like classical polymers, except that their size is steadily equilibrated by self-assembly of surfactant monomers according to the ambient conditions [6].

* modified from published article Assembling wormlike micelles in tubular nanopores by tuning surfactant-wall interactions. Bhuvnesh Bharti, Mengjun Xue, Jens Meissner, Viviana Cristiglio, Gerhard H. Findenegg, *Journal of the American Chemical Society*, 2012, 134, 14756-14759.

For a flexible or semi-flexible chain the number of possible configurations in confined space is smaller than in dilute solutions, resulting in a loss of configurational entropy. Accordingly, polymers avoid entering into pores of a size less than their effective molecular diameter [7], unless this entropy loss is balanced by attractive interaction with the pore walls. The influence of attractive and repulsive polymer-surface interactions on the partitioning of polymer chains between a pore and a reservoir has been highlighted in a theoretical study by Freed et al. [8], but experimental verification of these predictions is yet to be achieved.

Since wormlike micelles behave as *living polymers*, they may serve as model system for studying polymer partitioning between bulk solution and narrow pores. With this motivation we have studied self-assembly structures of a surfactant in cylindrical pores of diameter less than 10 nm. The surfactant in the pore space is in equilibrium with a bulk solution where it is forming extended wormlike micelles. We aim to find out if the formation of wormlike micelles in the pores, although entropically disfavored, can be induced by adjusting the interactions with the pore wall. As a sensitive and precise *in situ* method for modulating the interaction of the surfactant with the pore walls we adopt co-adsorption of low-molecular weight substance, which competes with the surfactant for the same adsorption sites at the surface.

Micellar aggregates of the nonionic surfactant $C_{12}E_5$ formed by adsorption from solution into the cylindrical pores of SBA-15 silica were examined *in situ* by small-angle neutron scattering (SANS). SBA-15 constitutes 2D ordered arrays of cylindrical pores of uniform size disposed parallel to each other and separated by thin silica walls [9, 10]. The pore size of SBA-15 (ca. 8 nm) is distinctly larger than the cross-sectional diameter of wormlike micelles of the surfactant $C_{12}E_5$ (ca. 5 nm). In preceding studies [11, 12] it was found that this surfactant is forming adsorbed patchy bilayers, indicating relatively strong interactions with the pore walls. To modulate this interaction and induce the formation of cylindrical micelles, a strongly adsorbed amino acid (lysine) was used as the surface modifier in the present work [13]. Slurry samples of SBA-15 with the surfactant and lysine were studied by SANS, using a H_2O/D_2O solvent mixture

which matches the scattering length density of the silica matrix (see Experimental Section).

Scattering from the slurry samples represents a sum of two contributions [11, 12]: Bragg scattering (I_{Bragg}) from the pore lattice, which provides information about the averaged radial concentration profile of surfactant in a pore, and diffuse scattering (I_{diff}) which depends on the way in which the surfactant aggregates are distributed in the matrix. Here we focus on the Bragg scattering term which enables us to discriminate between different structural scenarios of radial distribution of surfactant in a pore. For an array of long cylindrical objects [11]

$$I_{Bragg}(q) = KS(q)P(q) \quad (1)$$

where $S(q)$ is the structure factor of the pore lattice, $P(q)$ is the form factor of a unit cell, and K is a constant. The spherically averaged structure factor of a 2D-hexagonal lattice is given by $s(q) = q^{-2} \sum_{hk} m_{hk} S_{hk}(q)$ with m_{hk} the multiplicity factor of a reflection with Miller indices hk ($m_{hk} = 6$ for the (10), (11), and (20) reflections). The Bragg peaks $S_{hk}(q)$ were modeled by Gaussian functions $S_{hk}(q) = a_{hk} \exp[-b(q - q_{hk})^2]$ located at positions $q_{hk} = \left(\frac{4\pi}{a_0\sqrt{3}}\right) \left(h^2 + k^2 + hk\right)^{\frac{1}{2}}$, where a_0 is the lattice parameter of SBA-15, a_{hk} is the amplitude of peak (hk), and b characterizes the width of the Gauss peaks which was kept constant in the data analysis of all samples. The form factor $P(q)$ in eq 1 was modeled for different surfactant aggregate morphologies. Simulated Bragg scattering profiles for two different modes of surfactant self-assembly in the pore and for the case of micelle formation outside the pore space are shown in Figure 1. Simulations are based on the lattice parameter and pore diameter of the present SBA-15 sample ($a_0 = 11.6$ nm, $D = 8.2$ nm), a layer thickness of 2.5 nm for the adsorbed film, and a cross-sectional radius of 2.5 nm for cylindrical and wormlike geometries of the surfactant aggregates.

(i) If the surfactant is forming surface micelles or adsorbed bilayer patches (Figure 1a), the volume averaged configuration represents a surfactant layer at the pore wall. In the chosen silica contrast-match scenario, this geometry

corresponds to a *cylindrical shell*. Hence the form factor of a hollow cylinder, $P_{HC}(q)$, is adopted in eq 1. It causes changes of the individual Bragg peak intensities from the original lattice structure factor $S(q)$ (dotted) to the peak intensities indicated by shaded regions. Since the first minimum in $P_{HC}(q)$ is situated at a q value near the (10) Bragg reflection, the intensity of this peak is strongly reduced.

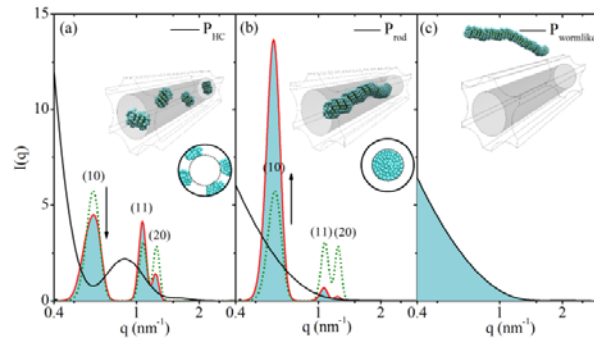


Figure 1. Simulated scattering profiles for three scenarios of surfactant aggregation as sketched in the cartoons (insets): (a) surface micelles adsorbed at the pore wall; (b) rod-like micelles in the core of the pore; (c) wormlike micelles in the solution outside the pores. The form factor of the aggregates is indicated by solid black lines, the Bragg peaks for empty pores by dotted lines; net scattering profiles for the three cases are indicated by shaded areas.

(ii) If the surfactant is forming cylindrical micelles or related structures in the center of the pores (Figure 1b), this can be simulated by the form factor of a cylindrical rod, $P_{rod}(q)$, in eq 1. As $P_{rod}(q)$ is a monotonic decreasing function in the relevant q range the intensity of (10) Bragg peak is enhanced relative to (11) and (20) in this scattering geometry.

(iii) If the surfactant is excluded from the pore space and forms wormlike micelles in the extrapore liquid volume, no Bragg scattering will occur in the chosen contrast scenario. Fig. 1c shows the scattering profile for wormlike micelles of the surfactant, based on the form factor of semi-flexible worms, $P_{worm}(q)$ [14].

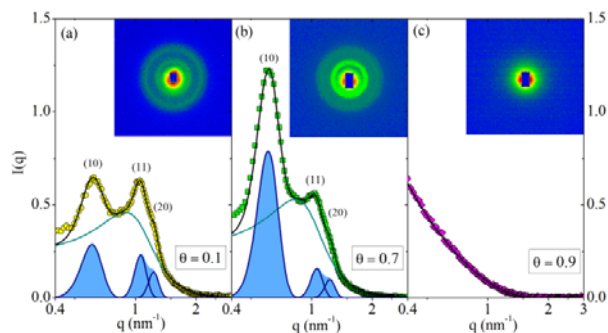


Figure 2. SANS 2D scattering patterns (insets) and 1D profiles $I(q)$ for SBA-15 slurry samples prepared with a fixed amount of $C_{12}E_5$ ($f = 0.95$) in contrast-matching H_2O/D_2O at different degrees of surface modification with lysine: (a) $\theta = 0.1$, (b) $\theta = 0.7$, (c) $\theta = 0.9$. Also shown are fits to the scattering profiles (black lines) based on a combination of a diffuse scattering term (green line) and Bragg scattering (contour of blue shaded area). In (c) the data are fitted by the form factor of wormlike micelles [14] without Bragg scattering term.

In the experiments, the influence of surface modification on the morphology of the surfactant aggregates in the pores was studied by co-adsorption of the amino acid lysine. The level of surface modification is expressed by the relative adsorption level of lysine, $\theta = n^L / n_m^L$, where n^L is the adsorbed amount and n_m^L is the maximum adsorbed amount (corresponding to a surface density of lysine molecules of 0.45 nm^{-2}). Scattering curves for a fixed surfactant loading (95% of maximum adsorption, corresponding to a volume fraction $\phi \approx 0.4$ of surfactant in the pore space [12]) at different lysine adsorption levels, $\theta=0.1$, 0.7 , and 0.9 , are shown in Figure 2. At the chosen lysine concentrations scattering originates almost entirely from the surfactant aggregates, while lysine makes no detectable contribution. The scattering curves for $\theta = 0.1$ and 0.7 represent a superposition of Bragg scattering and diffuse scattering. Separation was possible by modeling the diffuse scattering by the Teubner-Strey relation [15], which applies to microphase-separated systems with correlations among the domains. The resulting contributions $I_{Bragg}(q)$ and $I_{diff}(q)$ are also shown in the graphs. Results for the sample of lowest lysine adsorption ($\theta = 0.1$; Figure 2a) are in close agreement with earlier results for a sample without lysine [11]. As the lysine adsorption level increases, the (10) Bragg peak strongly increases, as shown for the sample of $\theta = 0.7$ (Figure 2b). However, as the lysine

adsorption level is further increased to $\theta = 0.9$, Bragg scattering vanishes and the profile can be modeled by the form factor of wormlike micelles [14] (Figure 2c). The pronounced changes in scattering behavior induced by surface modification can also be seen in the primary scattering patterns shown as insets in the graphs in Figure 2. Results as in Figure 2 were obtained independent of whether lysine was added before or after the surfactant, indicating that the morphology of the surfactant aggregates depends solely on the level of surface modification.

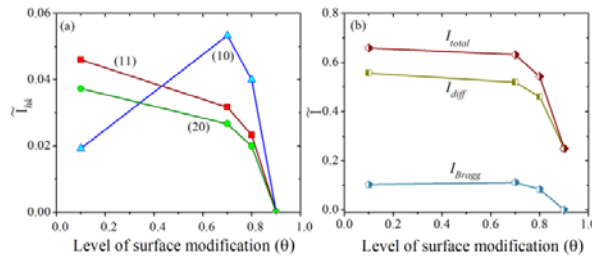


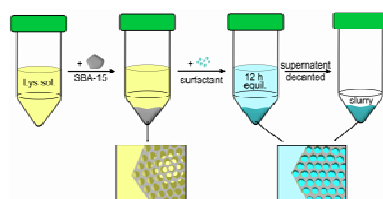
Figure 3. Integral scattering intensities for the surfactant $C_{12}E_5$ in SBA-15 slurry samples as a function of θ : **(a)** Integral intensity of the three leading Bragg peaks; **(b)** overall contribution from Bragg scattering, diffuse scattering, and total integral scattering intensity.

Further analysis of the data was performed on the basis of integrated intensities [12]. Individual integrated Bragg peak intensities \tilde{I}_{hk} are shown in Figure 3a, and the overall contributions from Bragg scattering (\tilde{I}_{Bragg}) and diffuse scattering (\tilde{I}_{diff}) are given in Figure 3b as a function of the level of surface modification θ . The total integrated intensity $\tilde{I}_{total} = \tilde{I}_{Bragg} + \tilde{I}_{diff}$, also shown in Figure 3b, is a measure of the overall amount of surfactant in the samples. From the evolution of individual peak intensities \tilde{I}_{hk} and the total intensity \tilde{I}_{total} shown in Figure 3, the following conclusions can be drawn:

- (1) As the lysine surface concentration increases from $\theta = 0.1$ to 0.7, the intensity \tilde{I}_{10} increases by a factor 3 while the intensities \tilde{I}_{11} and \tilde{I}_{20} decrease. This change in the peak intensities, combined with the fact that the amount of

surfactant in the sample (\tilde{I}_{total}) has remained constant, is conclusive evidence for a change of the aggregate morphology in the pores, from a surfactant layer at the pore walls (at $\theta = 0.1$) to aggregates of cylindrical geometry in the core of the pores (at $\theta = 0.7$). The mean diameter d of these aggregates can be estimated from the volume fraction of surfactant in the pores as $d = D\sqrt{\varphi}$. With the pore diameter $D = 8.2$ nm and volume fraction $\varphi = 0.4$, this gives $d = 5.2$ nm, which is similar to the diameter of wormlike micelles of $C_{12}E_5$ in solution [16]. This simple estimate implies that cylindrical micelles exist within the entire length of the cylindrical pores.

(2) As the lysine surface concentration is further increased from $\theta = 0.7$ to 0.9, all Bragg peaks vanish ($\tilde{I}_{Bragg} = 0$), indicating that no surfactant is left in the pore space, while \tilde{I}_{total} falls off to a low value, indicating that part of the surfactant is present in the extrapore liquid of the slurry sample (see Scheme 1), where the surfactant is now forming wormlike micelles, as to be concluded from the fit of the scattering curve in Figure 2c.



Scheme 1. Sample preparation for SANS measurements: SBA-15 was added to solutions of lysine in a H_2O/D_2O mixture that matches the scattering length density of the silica. After surfactant addition and equilibration (12 h) the supernatant was removed. The resulting slurry samples consist of SBA-15 powder containing most of the surfactant, and an approximately equal volume of solution.

For nonionic surfactants such as $C_{12}E_5$, the dominant binding mechanism to a silica surface is hydrogen bonding of the silanol groups to oxygen atoms of the ethoxylate head groups, either directly [17] or mediated with water molecules [18]. When lysine is competing with the surfactant for the silanol groups, the number of groups available for surfactant binding will decrease and thus its

adsorptive binding to the surface will become weaker as θ increases. However, since lysine is adsorbed to the silica surface via its terminal amino group [19], the zwitterionic α -amino acid moiety is exposed to the pore space and may contribute to the binding of surfactant via N-H...O hydrogen bonds from the α -amino group at high lysine adsorption levels. Further studies are underway to better understand the balance of attractive and repulsive interaction of the surfactant with the pore walls.

To our knowledge this work for the first time shows that the partitioning of wormlike micelles between a bulk solution and nanopores can be controlled by tuning the surface-wall interactions. According to the seminal theoretical study on chain partitioning between a pore and a reservoir by Freed et al. [8], attractive polymer-surface interactions become decisive in the regime of strong confinement, when $Q \equiv (\pi R_G/L)^2 > 1$, where R_G is the radius of gyration of the polymer and L is a measure of the pore size. The surfactant $C_{12}E_5$ studied in our case is forming semiflexible cylindrical micelles of a persistence length l_p of ca. 13 nm and contour length L_c of 300 nm at 20 °C [16]. Taking $R_G \approx 35$ nm and $L = D = 8.2$ nm, the present system corresponds to a confinement parameter $Q \approx 180$. For such high values of Q the theory [8] predicts a strong influence of the interaction parameter on the partition coefficient, decreasing from a high value for weakly attractive interactions to almost zero for weakly repulsive interactions (see Figure 9 of ref. 8). This agrees with the observed transition in the partitioning of the cylindrical micelles of $C_{12}E_5$ when the level of surface modification increases from $\theta = 0.7$ to $\theta = 0.9$. Further studies will show if the co-adsorption method to control the partitioning of wormlike micelles between pores and bulk phases can also be applied to classical polymers of higher flexibility than the semiflexible micelles considered here.

In conclusion, we have found that the self-assembly of a common nonionic surfactant in tubular 8 nm nanopores can be tuned by co-adsorption of the amino acid lysine, which reduces the adsorption affinity for the surfactant. An evolution of equilibrium morphologies of the surfactant aggregates was found as a function of the level of surface modification θ , using in-situ SANS which is

free from artifacts that can arise during the drying process for electron microscopy. At low lysine adsorption levels, the surfactant is forming patchy bilayer aggregates at the pore walls, as observed in the absence of lysine. At the highest degree of surface modification ($\theta = 0.9$), the surfactant is excluded from the pore space and forms wormlike micelles in the aqueous bulk phase, reminiscent of size exclusion of polymers from narrow pores with non-adsorbing walls. Remarkably, between these two regimes of weak and strong surface modification we find a domain in which the surfactant is entering the pores to form cylindrical aggregates. We conjecture that this state of cylindrical micelles in tubular nanopores is stabilized by weak adsorptive interactions with the wall, which remain just strong enough to balance the loss in configurational entropy relative to wormlike micelle in the unconfined solution.

This work may trigger further in-situ studies of morphological transitions of surfactant and polymer aggregates in nano-confinement by precisely tuning their interaction with the pore wall. The results will also contribute to a fundamental understanding of the role of attractive and repulsive interactions on the partitioning of polymeric entities between solution and nanopores.

Experimental

SBA-15 was synthesized as described previously [20] and characterized by nitrogen adsorption and small-angle X-ray scattering. The adsorption isotherm of lysine onto SBA-15 was determined at pH 7 as reported previously [13] and represented by the Langmuir equation (maximum specific adsorption $n_m^L = 0.57$ mmol g⁻¹, adsorption constant $K^L = 1.0$ mM⁻¹). The adsorption isotherm of the nonionic surfactant pentaethylene glycol monododecyl ether (C₁₂E₅) in SBA-15 exhibits a pronounced sigmoidal shape, reaching a limiting adsorption n_m^s shortly above the critical micelle concentration ($cmc = 6.5 \times 10^{-5}$ M) [11]. For the present SBA-15 material, $n_m^s = 1.15$ mmol g⁻¹. Samples for SANS measurements were prepared as sketched in Scheme 1, using a H₂O/D₂O solvent mixture which matches the scattering length density of SBA-15 ($\rho_{silica} = 3.7 \times 10^{-4}$ nm⁻²) [12]. Samples of fixed loading with surfactant (corresponding to a relative

filling $f = \frac{n^s}{n_m^s} = 0.95$) and a range of lysine surface concentrations θ were prepared.

References

- [1] Ramanathan, M.; Kilbey II, S. M.; Ji, Q.; Hill, J. P.; Ariga, K. J. *Mater. Chem.* 2012, 22, 10389-10405.
- [2] Shin, K.; Xiang, H.; Moon, S. I.; Kim, T.; McCarthy, T. J.; Russell, T. P. *Science* 2004, 306, 76.
- [3] Ma, M.; Titivesky, K.; Thomas, E. L.; Rutledge, G. C. *Nano Lett.* 2009, 9, 1678-1683.
- [4] Yu, B.; Jin, Q.; Ding, D.; Li, B.; Shi, A.-S. *Macromolecules* 2008, 41, 4042-4054.
- [5] Arai, N.; Yasuoka, K.; Zeng, X. C. *J. Am. Chem. Soc.* 2008, 130, 7916-7920.
- [6] May, S.; Bohbot, Y.; Ben-Shaul, A. *J. Phys. Chem. B* 1997, 101, 8648-8657.
- [7] de Gennes P.-G. *Scaling Concepts in Polymer Physics*, Cornell University Press, Ithaca, 1979.
- [8] Freed, K. F.; Dudowicz, J.; Stukalin, E. B.; Douglas, J. F. *J. Chem. Phys.* 2010, 133, 094901.
- [9] Zhao, D.; Feng, J.; Huo, Q.; Melosh, N.; Fredrickson, G. H. Chmelka, B. F.; Stucky, G. D. *Science* 1998, 279, 548-552.
- [10] Sundblom, A.; Oliveira, C. L. P.; Pedersen, J. S.; Palmqvist, A. E. C. *J. Phys. Chem. C* 2010, 114, 3483-3492.
- [11] Mütter, D.; Shin, T.; Demé, B.; Fratzl, P.; Paris, O.; Findenegg, G. H. *J. Phys. Chem. Lett.* 2010, 1, 1442-1446.
- [12] Shin, T. G.; Mütter, D.; Meissner, J.; Paris, O.; Findenegg, G. H. *Langmuir* 2011, 27, 5252-5263.
- [13] Bharti, B.; Meissner, J.; Gasser, U.; Findenegg, G. H. *Soft Matter* 2012, 8, 6573-6581.
- [14] Kholodenko, A. L. *Macromolecules* 1993, 26, 4179-4183.

- [15] (a) Teubner, M.; Strey, R. J. Chem. Phys. 1987, 87, 3195; (b) Sottmann, T.; Strey, R.; Chen, S.-H. J. Chem. Phys. 1997, 106, 6483.
- [16] Menge, U.; Lang, P.; Findenegg, G. H.; Strunz, P. J. Phys. Chem. B 2003, 107, 1316-1320.
- [17] Trens, P.; Denoyel, R. Langmuir 1993, 9, 519-522.
- [18] Matsson, M. K.; Kronberg, B.; Claesson, P. M. Langmuir, 2004, 20, 4051-4058.
- [19] Kitadai, N.; Yokoyama, T.; Nakashima, S. J. Colloid Interface Sci. 2009, 329, 31-37.
- [20] Akcakayiran, D.; Mauder, D.; Hess, C.; Sievers, T. K.; Kurth, D. G.; Shenderovich, I.; Limbach, H.-H.; Findenegg, G. H. J. Phys. Chem. B 2008, 112, 14637-14647.